Toward Rational Design of Graphene Nanomaterials: Manipulating Chemical Composition to Identify Governing Properties for Electrochemical and Biological Activities

by

Yan Wang

Bachelor of Engineering, Sun Yat-sen University, 2009

Master of Engineering, Zhejiang University, 2012

Submitted to the Graduate Faculty of the

Swanson School of Engineering in partial fulfillment

of the requirements for the degree of

Doctor of Philosophy

University of Pittsburgh

2020

UNIVERSITY OF PITTSBURGH

SWANSON SCHOOL OF ENGINEERING

This dissertation was presented

by

Yan Wang

It was defended on

March 17, 2020

and approved by

Leanne M. Gilbertson, Ph.D., Assistant Professor, Department of Civil and Environmental Engineering, Department of Chemical and Petroleum Engineering

Prashant N. Kumta, Ph.D., Professor, Department of Chemical and Petroleum Engineering, Department of Bioengineering, Department of Mechanical Engineering and Material Science, Department of Oral Biology

James R. Mckone, Ph.D., Assistant Professor, Department of Chemical and Petroleum Engineering

Carla A. Ng, Ph.D., Assistant Professor, Department of Civil and Environmental Engineering, Department of Chemical and Petroleum Engineering

Radisav R. Vidic, Ph.D., Professor, Department of Civil and Environmental Engineering, Department of Chemical and Petroleum Engineering

Dissertation Director: Leanne M. Gilbertson, Ph.D., Assistant Professor, Department of Civil and Environmental Engineering, Department of Chemical and Petroleum Engineering

Toward Rational Design of Graphene Nanomaterials: Manipulating Chemical Composition to Identify Governing Properties for Electrochemical and Biological Activities

Yan Wang, PhD

University of Pittsburgh, 2020

The unique properties of graphene-based nanomaterials (GMs) have enabled various applications in the fields of electronics, energy, environment, and biotechnology. Yet, their potential inherent hazard poses risks to human health and the environment, which could be a barrier to the success of these applications. A critical underpinning of sustainable material development is rational design. This approach involves the ability to control material outcomes, requiring the establishment of property-function and property-hazard relationships. This dissertation aims to demonstrate an ability to rationally design GMs by manipulating chemical composition and establishing the relationships that correlate material properties to their electrochemical activity (function) and bioactivity (hazard). The electrochemical activity is represented by the material reactivity for important electrochemical reactions (oxygen reduction reaction, ORR and oxygen evolution reaction, OER). The bioactivity is represented as the material propensity to oxidize a cellular biomolecule (glutathione) and inactivate the bacteria (*Escherichia coli*).

Material sets of graphene oxide (GO) and nitrogen-doped graphene (NG) are investigated using various complementary characterization techniques to determine the material properties that govern electrochemical and biological activities as chemical composition changes. The results suggest both activities are governed by synergistic effects from multiple properties, including specific oxygen and nitrogen sites and properties arising as a consequence of changing chemical composition. Enhanced aqueous dispersion and defect density are important for GO bioactivity. Additionally, coupled experimental and computational approaches elucidate the synergistic role of adjacent epoxide and hydroxyl groups on GO in directly oxidizing glutathione. As the surface of GO is reduced, the electrochemical and biological activities are governed by a balance of carbonyl groups and electrical conductivity. For NG, N-types control electrochemical reactions, ORR (graphitic-N) and OER (pyridinic-N). Further, the predominance of graphitic-N enhances oxidative stress-related bioactivity, which is an important contribution since very little is known surrounding NG bioactivity.

Collectively, this dissertation supports the use of chemical composition manipulation to control material properties and in turn, function and hazard outcomes. The established property-function and property-hazard relationships provide rational design guidance for GMs. The holistic approach herein is applicable to other nanomaterials and thus, will continue to contribute to the advancement of sustainable nanotechnology.

Table of Contents

List of Tables

List of Figures

Acknowledgements

While my doctoral study is coming to an end, it is yet the end of a chapter in my life, and I am turning a page to start a new journey. My path to a Ph.D. was not always smooth, but it was very fruitful through strong support, professional guidance, and enthusiastic encouragement from my mentors, family, friends, and colleagues. At this moment, I am excited beyond words to complete this dissertation.

I cannot begin to express my thanks to a great woman, my advisor Dr. Leanne Gilbertson, for her relentless and heartfelt mentorship toward my pursuits both in and out of the lab. Dr. Gilbertson has set an example of excellence as a researcher and a role model. After five years of working with her, I have been influenced by her meticulous attitude toward research and her profound insights, which have greatly enhanced my personal and intellectual growth. She helped me through various queries that I encountered throughout my doctoral study, ranging from the proposal of projects to the writing of papers; there were many times I thought of the Chinese Song Dynasty poem, which reads "After endless mountains and rivers that leave doubt whether there is a path out, suddenly one encounters the shade of a willow, bright flowers, and a lovely village." She guided me to my path!

I would like to extend my sincere thanks to my committee members Dr. Prashant Kumta, Dr. James Mckone, Dr. Carla Ng, Dr. Radisav Vidic and my collaborators Dr. Howard Fairbrother, Dr. John Keith, Dr. Vikas Khanna, and Dr. Francois Perreault for their decisive roles in defining the path of my research and guiding my professional development. I have had the great pleasure of working with such a brilliant group of academics. Their unparalleled knowledge, illuminating ideas, and constructive advice have been great contributors in completing this dissertation.

I would like to acknowledge the generous support from funding institutions, including the National Science Foundation CBET Award No. 1709031, the University of Pittsburgh Central Research Development Fund, and the Department of Civil and Environmental Engineering and Swanson School of Engineering at the University of Pittsburgh.

I cannot leave the University of Pittsburgh without mentioning my office and lab folks (Nathalia Aquino de Carvalho, Dr. Alen Gusa, Dr. Vaclav Hasik, Sishan Li, Dr. Omkar Lokare, Lisa Stabryla, Dr. Sakineh Tavakkoli, Dr. Nemi Vora, Dr. Shardul Wadekar, Tianyu Zhang, Zhewei Zhang), who have made my days abroad colorful and helped me succeed in my Ph.D. journey in their own ways. Many thanks should also go to my dear friends, past and present, for keeping good times flowing and bringing wonderful memories.

My success toward a Ph.D. would not have been possible without the unwavering support and unconditional love from my family. My parents have nurtured, supported, and blessed me generously. They have encouraged me through countless ups and downs, especially through long distance video calls across time zones. My brother, whose dreams for me have led to my achievements today, has been my confidant to assist me to make wiser decisions at every important crossroad of my life, inspiring me to pursue my ambitions. My fiancé has been a comrade for my adventures over the years; he has stood by my side through joys and sorrows and has constantly supported me to achieve every goal. Thank you, and I am deeply indebted to you!

I Dedicate This Dissertation
To My Parents (LJ. Wang & HF. Shi) and My Brother (L. Wang),
Who Made Me Who I Am

1.0 Dissertation Introduction

1.1 Motivation

1.1.1 The Need for Rational Design of Graphene-Based Nanomaterials

Sustainable and rational design of chemicals is considered vital to the vision of success in various industries, and its core lies in maximizing performance while ensuring minimum negative impacts on human health and the environment. The many unintended consequences of chemistry's past (e.g., asbestos, DDT, CFCs, PCBs) stimulated the emergence of the 12 Principles of Green Chemistry[1], which further motivated efforts to identify correlations between structure, physical and chemical properties, and toxicity for designing benign chemicals.[1, 2]

The 12 Principles of Green Chemistry are further applied for green nanoscience and nanotechnology to the design, manufacture, and use of nanomaterials,[3] emphasizing the establishment of the relationships between structure and/or properties, function, and hazard to inform rational design guidelines.[3-6] Rational design places emphasis on both the desired function and inherent hazard, aiming to advance the functional performance of the selected materials while eliminating the potential of risk.[7] This approach necessitates the ability to control both outcomes through manipulation of the material, which requires knowing the relationship with structure and/or property features. Engineered nanomaterials (ENMs) are defined as the materials of which the individual structure has at least one dimension between 1 and 100 nm and the agglomerate/aggregate owns a volume specific surface greater than 60 m^2/cm^3.[8] ENMs are characterized with unique physicochemical properties and improved reactivity compared to their bulk forms. The remarkable properties of ENMs have enabled their use in a wide range of fields to benefit society while accompanying with unknown (and early on, uncharacterized) hazard.[9, 10] Consequently, it is critical to proactively identify environmental and health risks before ENMs have widely diffused into the market.

The focus of my research is on graphene-based nanomaterials (GMs). There has been intense interest in GMs in the past decade for use in fields such as chemistry, physics, and materials science.[11-16] Yet, their potential risk to human health and the environment could be a barrier to the adoption and success of these applications.[17-20] This motivates the critical need for the establishment of relationships that correlate material properties with function and hazard profiles. Doing so informs a path towards intentionally manipulating the hazard profile of the GM while ideally, maintaining the functional performance (i.e., when different properties govern the function and hazard profiles). The development of these relationships requires evaluations of both functional performance and inherent hazard with a systematically prepared and comprehensively characterized GM material set.[5, 21, 22] Only through a comprehensive understanding of these relationships will GMs be rationally designed and their application potential be fully realized.

1.1.2 Graphene Properties and Synthesis

Graphene is an array of carbon atoms organized into a two-dimensional (2D) hexagonal lattice in a single atomic layer. There has been an explosion in research after the first isolation of graphene from bulk graphite using the Scotch tape method by Andre Geim and Konstantin Novoselov in 2004.[23] Graphene’s breakthrough electronic, thermal, optical, and mechanical properties result from the sp^2 hybridized structure (each carbon atom is bonded with three carbon atoms) and extremely thin atomic thickness (0.345 nm).[24]

Graphene is a zero-gap semiconductor (also called a zero-overlap semimetal) with electron-hole charge carriers driving superior electrical conductivity.[25] The sp^2 hybridized structure introduces highly mobile π electrons located above and below the graphene sheet, these bonding (π) and antibonding (π*) orbitals construct a valence and conduction band structure.[26] The connection of these two bands (i.e., no bandgap) enables the ease of electron excitation from the valence band into the conduction band, making graphene an excellent electrical conductor. Remarkable electron mobility (greater than 15,000 $cm^2V^{-1}S^{-1}$) can be obtained by graphene, which is 1,000,000 times higher than that of copper.[27] Likewise, a high thermal conductivity (~5000 $Wm^{-1}K^{-1}$) is achieved for graphene due to covalent sp^2 bonding between carbon atoms.[28] Given that out-of-plane atomic vibrations are more energetically favorable compared to in-plane vibrations, an unusual thermal property is observed for graphene; the sheet shrinks when it is heated and expands when it is cooled.[29] High carrier transport also enables the ability for a single layer of graphene to absorb 2.3% of while light (equal to 97.7% transparency), with the light absorption linearly related to the number of layers.[30] The unique band structure of graphene causes the production of optical transitions in electric fields, resulting in ultrafast and efficient optoelectronic response.[30] Further, the stability of the sp^2 bonds in graphene can protect against in-plane deformations contributing to exceptional mechanical properties.[31] Graphene is regarded as the strongest material ever measured in terms of stiffness, strength, and toughness.[24] For example, tests have shown that the ultimate tensile strength of graphene is three orders of magnitude higher than that of steel.[24] Versatile techniques can be used to characterize the multitude of GM physical and chemical properties, which are compiled in Table 1.1.

Table 1.1 Techniques used for different physical and chemical property characterization of graphene-based nanomaterials.

Material Properties Characterized	Techniques
Morphology	Scanning electron microscope (SEM), transmission electron microscopy (TEM)
Thickness, number of layers	High-resolution TEM (HRTEM), atomic force microscope (AFM), Raman
Elemental composition	Energy-dispersive X-ray spectroscopy, X-ray photoelectron spectroscopy (XPS)
Types of functional groups and dopants	XPS, attenuated total reflectance-Fourier transform infrared spectroscopy (ATR-FTIR)
Defects, n- or p-type doping	Raman
Crystallinity	X-ray diffraction (XRD), Raman
Thermal stability and purity	Thermogravimetric analysis (TGA)
Electrical conductivity	4-point probe
Surface area (dry powder)	Brunauer-Emmett-Teller (BET) analysis
Dispersed surface area (in suspension)	Methylene blue adsorption
Particle/aggregate size	Dynamic light scattering (DLS)
Surface charge (zeta potential)	Electrophoretic light scattering (ELS)
Electrochemical activity (E_{on}, J, $E_{1/2}$, n, ECSA)	Rotating disk electrode (RDE), rotating ring disk electrode (RRDE)

Due to these unparalleled properties, graphene has been heralded as a 'wonder material' and used in a broad spectrum of applications such as composites (e.g., scaffold or filler materials), energy generation and storage (e.g., active materials for electrodes in batteries, supercapacitors, fuel or solar cells), water treatment (e.g., molecule or ion filtration), electronics (e.g., transistors, current or heat spreaders, flexible and stretchable electronics), and biomedical devices (e.g., drug delivery, biosensing, and bioimaging).[11-16] In light of the developing and expanding applications, there has been steady progress toward the commercialization of graphene. The production volume of graphene has increased from 14 tons in 2009 to approximately 1,200 tons in 2019.[16] A meta-market analysis of twenty available market studies for graphene shows that the estimated market value of graphene material ranges from US$ 15-50 million in 2015 to US$200-2,000 million in

2025 (corresponding to an average growth rate of around 40%).[32] Also, a comparison of market forecasts by application areas reveals a much higher market potential for energy storage applications (greater than US$100 million by 2025) than others.[32]

Graphene can be fabricated by top-down and bottom-up routes. The top-down approach directly exfoliates graphene sheets from bulk graphite, primarily including micromechanical cleavage and chemical exfoliation. Epitaxial growth on silicon carbide substrate and chemical vapor deposition (CVD) primarily represent the bottom-up methods to synthesize graphene from carbon precursors.

The micromechanical cleavage is a method using adhesive tape to peel off the graphite surface, which is commonly employed to isolate single- or few-layered graphene.[23] While this elegantly simple method is popular for education and demonstration purposes, it is not very realistic for scalable production. Instead, liquid-phase mechanical exfoliation is used, where solvent- or surfactant-aided sonication is employed to isolate individual graphene sheets from graphite.[33] The nondestructive nature of mechanical exfoliation allows the isolation of single-crystalline graphene domains in a larger area.[33]

Chemical exfoliation typically involves the processes through the oxidation of graphite to graphite oxide, followed by sonication-centrifugation exfoliation to graphene oxide (GO), and further reduction of GO to obtain reduced GO (rGO) or chemically converted graphene. GO is a derivative of graphene with different oxygen functional groups on its basal planes (hydroxyl and epoxide groups) and at its edges (carbonyl and carboxylic acid groups).[34, 35] The oxygen functional groups endow GO to be hydrophilic, such that it can form a highly dispersed suspension that enhances the aqueous assembly of macroscopic structures.[36] Various oxidants are used to treat graphite to produce graphite oxide and GO, including the combined use of concentrated H_2SO_4

and 1) $NaNO_3$, $KMnO_4$ (Hummers); 2) $KClO_3$ and HNO_3 (Staudenmaier, Hoffmann); and 3) H_3PO_4 and $KMnO_4$ (Tour).[37] Hummers' method is the most popular bottom-up synthesis approach of graphene. Reduction of GO, the process of removing oxygen functional groups and restoring the conjugated structure of graphene, can be achieved by 1) thermal reduction including thermal annealing at high temperatures and microwave- or photo-irradiation; 2) chemical reduction with reducing agents such as hydrazine, sodium borohydride, lithium aluminum hydride, and ascorbic acid; 3) electrochemical reduction that relies on the electron exchange between GO and electrodes without using chemical agents.[36] The extent of reduction and the abundance of specific surface functional groups can greatly influence electronic properties and the reactivity of graphene.[21, 36, 38-40] The graphene product from chemical exfoliation of graphite differs from pure graphene. For example, various defects are introduced during the oxidation of graphite and the subsequent reduction of GO will not sufficiently 'heal' these defects, degrading the electronic structure of graphene.[36] Yet, the chemical exfoliation method is currently the most facile and cost-effective and suitable for mass production. The resulting graphene product can be used for many applications where high purity is not strictly required such as composites and energy storage applications but may not be satisfactory for sensitive electronic applications.

Epitaxial graphene can be grown on silicon carbide substrate through silicon sublimation at high temperature (>1300 °C).[30] Epitaxy refers to a process of depositing a crystalline layer on the surface of a crystalline substrate. For a typical CVD process, graphene is grown on metal substrates (e.g., copper, nickel) through the decomposition of hydrocarbon precursors (e.g., methane) at high temperature (800 to 1100°C).[33] The primary advantage of these two methods is the ability to produce high quality (e.g., large-area single crystal, defect-free) and well-controlled (e.g., controllable layers/thickness) graphene. This high quality, defect free graphene is necessary for electronic and optical applications. Yet, both methods require specialized instruments and expensive materials and the yield is rather low.

Additionally, doping graphene with various heteroatoms (e.g., B, N, P, S) is an effective approach to tune electronic properties of graphene and further its chemical reactivity.[41-44] Heteroatom-doped graphene reveals new and enhanced material properties and bring forward the development in electronics, electrocatalysts, and energy storage and conversion.[41-44] The synthesis of heteroatom-doped graphene can be classified into *in-situ* doping and post-treatment synthesis. Dopant precursors can be in the form of gas, liquid, or solid. The common dopants include N_2, NH_3, melamine, urea for N; H_3BO_3, B_2H_6, BBr_3, BCl_3 for B; $(NH_4)_2HPO_4$, $(NH_4)_3PO_4$ for P; elemental sulfur, H_2S, Na_2S, CS_2 for S.[42, 43] *In-situ* doping methods are coupled with bottom-up routes such as CVD. With the addition of dopant precursors, the heteroatoms are incorporated into the graphitic lattice along with the growth of graphene. The post-treatment doping commonly involves the reduction of GO via thermal annealing or chemical reduction in the presence of the heteroatom precursor. In this approach, the oxygen functional groups of GO serve as the active sites for heteroatom doping.[43] Plasma and arc discharge are also used to treat GO or graphene with the dopant source.[42, 43]

1.1.3 Electrochemical Activity

The electrochemical properties of graphene have advanced many applications ranging from sensing to energy storage due to its outstanding properties. Several reviews have covered the benefits of GMs for a variety of electrochemical applications.[45-48] In this dissertation, the functional performance is represented by the electrochemical activity of prepared GM materials given the prominent role of GMs in advanced energy technologies.[49] The oxygen reduction reaction (ORR), oxygen evolution reaction (OER), and hydrogen evolution reaction (HER) are core reactions to the development of clean energy technologies (e.g., water splitting system, fuel cells, solar cells, and metal-air batteries).[15, 42, 44] Metal-free catalysts, including GMs, have gained popularity in these reactions because conventional catalysts are commonly composed of noble metals that are often rare, finite, and cost-intensive.[15, 42, 44] Compared to HER, ORR and OER are more sluggish owing to a demand of four-electron transfer[50], thus, developing highly-efficient catalysts to speed up the kinetics of these two reactions becomes a focus of attention. The material reactivity toward ORR and OER is studied in this dissertation. While ORR is aimed to reduce O_2 to H_2O, OER works in a reverse way to oxidize H_2O to O_2. While ORR can be run in acidic or alkaline media, the latter favors the reaction due to a lower overpotential and a corrosion-resistant environment.[51] While acidic media limit the OER electrocatalysts to precious-metal-based ones, alkaline media expand the range of OER electrocatalysts to carbon-based materials.[52] Thus, ORR and OER in alkaline media are conducted in this dissertation.

An electrode reaction generally contains three elementary steps: 1) the mass transfer of the reactant from the bulk electrolyte to the electrode surface, 2) electron transfer on the electrode surface, 3) diffusion of the product from the electrode surface. The electrode activity (step 2) is often the focus of interest, and the rate of electron transfer reaction (i.e., current) determines how the electrode system should be designed to control mass transfer rates. To quantitatively analyze the activity for the step 2, rotating disk electrode (RDE) is commonly used to regulate the mass transfer rates of steps 1) and 3).[53] Combining a ring electrode with RDE, the rotating ring disk electrode (RRDE) enables the ability to detect the reaction intermediates, providing insights into the understanding of the reaction mechanisms.[53] Analyzing voltammetry curves (measurement of current as potential is varied) enables obtainment of the electrochemical parameters (as included in Table 1.1)for evaluation of electrochemical activity of electrode materials, including 1) onset potential (E_{on}, the potential where the current starts to rise); 2) limiting current density (J, the maximum current normalized to the electrode area); 3) half-wave potential ($E_{1/2}$, the potential where the current is half of the limiting current density); 4) electron transfer number (n); and 5) electrochemically active surface area (ECSA, the area of electrode materials responsible for electron transfer).

1.1.4 Biological Activity

Along with wide applications of GMs, studies have demonstrated their biological and toxicological effects on bacteria, mammalian cells, plants, and animals.[18-20, 54, 55] Understanding potential adverse effects of new materials on human health and the environment is critical to ensure realization of their promise. The hazard of GMs in this dissertation is represented as the propensity for materials to oxidize cellular biomolecules and to induce bacterial cytotoxicity. However, the results for these two bioactivities will also inform the advancement of applications where the hazard is an intended function, such as enhanced detection of target biomolecules or bacterial analytes and targeted antibacterial action.

Glutathione (GSH) is a crucial thiol-rich tripeptide in eukaryotic and mammalian cells, which serves as the predominant antioxidant enzyme to maintain the redox environment of cells and protect against the cellular oxidative stress by scavenging the free radicals that damage other important cellular components (e.g., DNA, protein).[38, 56-58] The oxidized form of GSH is glutathione disulfide (GSSG); the ratio of GSH to GSSG serves as the predictor of cell redox state and the ability of the cell to defend against oxidative stress.[57] The level of GSH in the tissues has been associated with many diseases, such as cancers, Parkinson's, Alzheimer’s, and HIV.[38, 56] Given the pertinence of GSH to oxidative stress, acellular oxidation of GSH is used to evaluate the effects of oxidative stress induced by GMs.[22, 58-60]

Evaluating the activity of GMs against bacteria is a key step to understanding their bioactivity. Bacteria are facile test subjects and important targets when evaluating environmental hazards and fates of ENMs due to the following reasons[61]: the bacterial community diversity in the natural environment can be impacted by ENMs; the physicochemical properties of ENMs can be modified through interacting with bacteria, leading to changes in environmental fate and transport of ENMs (e.g., bioavailability, environmental partitioning); ENMs can influence nutrient cycling reactions (important in wastewater treatment and agriculture) by altering bacterial physiology; the biodegradation of ENMs by bacteria may occur; and the trophic transfer of ENMs can happen from bacteria to their predators. *Escherichia coli K12* (*E.coli*) is used as the model bacterium in this dissertation due to its well-studied physiology and facile genetic manipulation.[62, 63] Although *in vitro* GSH oxidation is correlated to the chemical influence (i.e., oxidative stress) of GMs,[21, 22, 58, 59] it is important to study *in vivo E. coli* inactivation as well to explore the physical influence of materials given the sheet-like structure of materials and has already been shown in several studies.[55, 58, 64]

Oxygen is of great importance in biological systems, specifically, associated with oxidative stress in the GSH and *E. coli* assays employed in this dissertation. Studying oxygen related electrochemical reactions (aforementioned ORR and OER) can elucidate the interaction between GMs and oxygen and further our mechanistic understanding of oxidative stress related bioactivity.

1.1.5 Literature Review on Identified Property-Function Relationships and Property-Hazard Relationships

Graphene, graphene oxide, and nitrogen-doped graphene (NG) are studied in this dissertation. In this section, results regarding parametric relationships for these three classes of materials are summarized from previous studies. Specifically, property-function relationships for each graphene material with ORR and OER (functional performance metrics) are compiled in Table 1.2 and property-hazard relationships compiled in Table 1.3 using GSH oxidation and *E. coli* inactivation as hazard metrics.

Size, shape, and chemical composition are recognized as three primary parameters of a nanomaterial that can serve to manipulate material physicochemical properties, which we know influence the material reactivity towards functional and hazard outcomes. Capturing the changes of important material properties across a modified material set enables establishing meaningful relationships between governing properties and outcomes of interest. In this regard, studying and comparing outcomes of one modified sample is not useful to inform such relationships. In this way, we propose that a minimum set of three modified materials should be prepared through tailoring a single chosen parameter and compared to a non-modified control (e.g., graphene).

Table 1.2 Compiled results on property-function relationships from studies of GMs (graphene, G; graphene oxide, GO; and N-doped graphene, NG) for electrochemical activities (ORR and OER).

GMs	Approach to modify GM properties^a (#^{b})	Electrochemical outcomes (ORR or OER)	Identified governing physicochemical properties	Relative reactivity comparison between materials	Refs
NG	Shape (2)	ORR	High surface area and density of active sites	3D NG > 2D NG	65
NG	Shape (3)	ORR	High surface area, large pore volume, high defects, and N-type (graphitic-N)	3D NG > porous 2D NG > nonporous 2D NG	66
		OER	High surface area, large pore volume, high defect, and N-type (pyridinic-N)	3D NG > porous 2D NG ≈ nonporous 2D NG	
NG	Chemical composition (4)	ORR	High surface area, large pore volume, high defects, and N-types (both graphitic-N and pyridinic-N are important)	All 3D NG samples > rGO	67
NG	Chemical composition (4)	ORR	High defects and N-type (graphitic-N)	All NG samples > G	68
		OER	–	NG > G	
NG	Chemical composition (8)	ORR	High electrical conductivity and N-type (graphitic-N)	All NG samples > G	69
NG	Chemical composition (7)	ORR	N-type (pyridinic-N)	All NG samples > rGO	70
		OER	–	All NG samples > rGO	
NG	Chemical composition (4)	ORR	High surface area, high electrical conductivity, and N-types (both graphitic-N and pyridinic-N are important)	All NG samples > rGO	71
		OER	High surface area, high electrical conductivity, and N-types (both graphitic-N and pyridinic-N are important)	All NG samples > rGO	
NG	Chemical composition (7)	ORR	Large electrochemical active surface area and N-type (graphitic-N)	The NG samples with proper N-doping > rGO	72
NG	Chemical composition (5)	ORR	N-type (pyridinic-N)	The NG sample with the most pyridinic-N	73
NG	Chemical composition (4)	ORR	High electrical conductivity and N-type (graphitic-N)	The NG sample with the most graphitic-N	74
NG	Chemical composition (3)	ORR	N-type (pyridinic-N)	The NG sample with the most pyridinic-N	75
NG	Chemical composition (5)	ORR	High surface area and N-type (pyridinic-N)	The NG sample with the most pyridinic-N	76

[a] The use of shape to modify NG properties refers to the integration of 2D graphene sheet into 3D porous structure. The use of chemical composition to modify NG properties refers to the changes in the C/N ratio and the percent distribution of N-types. [b] The number of unique GM samples studied.

Note: "–" indicates that the information is not available. ">, ≈, <" refers to superior, equal, inferior, respectively.

GMs have been widely investigated for ORR whereas only a few studies are available for OER (Table 1.2). Since NG was demonstrated to have much better electrocatalytic activity than graphene, it has been extensively studied as the active GM electrode. GO, however, is generally studied as the electrode support for deposition of functional materials (e.g., organic compounds, nanoparticles, polymers, and biomaterials), which not only helps the dispersion of functional materials but also enhances mass transport and electron transfer.[48]

In electrochemical studies, shape and chemical composition have been used to manipulate properties of GMs (particularly NG) to constitute a material set (Table 1.2), while the latter has been used more commonly. Herein, the use of shape to control GM properties specifically refers to the integration of 2D graphene sheet into 3D porous structure. Synthesis of 3D porous carbon-based nanostructures can be achieved by using 1) template method, where hard templates (e.g., mesoporous silica) and soft templates (e.g., surfactant) are employed, and 2) self-assembly approach (e.g., hydrothermal treatment).[77] Taking advantage of large surface area, high porosity, and tunable compositional traits, these porous materials have demonstrated outstanding ORR and OER performance.[77] The use of chemical composition to manipulate NG properties refers to the doping of N resulting in the changes in the C/N ratio and the percent distribution of N-types. Compositional effects can be produced during the synthesis process by either changing the ratio of graphene and nitrogen precursors or annealing temperatures for thermal treatment approach considering different thermal stability between N-types.[41]

The identified governing properties for ORR and OER activities include electrical conductivity to transport electrons,[69, 71, 74, 78-80] defects to offer active sites,[66-68, 81, 82] surface area available for electron transfer on it and mass transport of reactants,[65, 67, 71, 72, 76, 77, 80] and surface groups (e.g., ketonic C=O, pyridinic-N, graphitic-N), which accelerate the adsorption of reactants (and the reaction intermediates) and facilitate electron transfer.[21, 39, 40, 66, 75] While significant effort has been made to explore the contributions of nitrogen configurations to ORR and OER, there is debate over the relative contribution of graphitic-N and pyridinic-N to improved ORR and OER activity.

In biological studies of graphene and GO (Table 1.3), size and chemical composition are the two predominant approaches used to manipulate GM properties. Size of 2D graphene sheets is most commonly manipulated by subjecting dispersion to varying sonication time.[58, 83] Tuning chemical composition of GO is often accomplished by varying the oxidation level, which can be realized by employing different synthetic methods of GO and reduction techniques (e.g., thermal and chemical).[36, 37, 84] While there is a wide variety of biological assays employed to evaluate the bioactivity of GO, only a few studies use GSH oxidation and *E. coli* inactivation, as is done in this research. Additionally, very little is investigated regarding NG mediated bioactivities; the role of N-types on GSH oxidation and *E. coli* inactivation remains to be elucidated.

Size, defects, aggregation, the orientation of graphene sheets (edge versus basal plane), and electrical conductivity are identified to influence the activity of graphene and GO toward GSH oxidation and *E. coli* inactivation (Table 1.3). The prevailing mechanisms that contribute to adverse biological consequences of GMs involve physical and chemical aspects. Physical mechanisms can be the membrane damage caused by sharp edges of GMs[55, 59, 85, 86] and the wrapping of microorganisms due to the sheet structure of GMs.[55, 58, 64] Chemical mechanisms are mainly represented by oxidative stress produced from GMs either with or without the participation of reactive oxygen species (ROS).[55, 58-60, 87-89]

Table 1.3 Compiled results on property-hazard relationships from studies of GMs (graphene, G and graphene oxide, GO) for biological activities (GSH oxidation and *E. coli* inactivation).

GMs	Approach to modify GM properties[a] (#[b])	Biological outcomes (GSH oxidation or *E. coli* inactivation[c])	Identified governing physicochemical properties	Relative reactivity for comparison between materials	Refs
GO	Chemical composition (2)	*E. coli* inactivation (surface)	–	rGO > GO (biocompatible)	90
GO	Chemical composition (2)	*E. coli* inactivation (surface)	Sharp sheet edges and high electrical conductivity	rGO > GO	63
GO	Chemical composition (2)	*E. coli* inactivation (suspension)	Small aggregate size or good aqueous dispersion, and high density of surface functional groups	GO > rGO	59
		GSH oxidation	High electrical conductivity	rGO > GO	
G and GO	Chemical composition (2)	*E. coli* inactivation (suspension and molecular dynamics simulation)	Unoxidized graphene sheet and large lateral size	G > GO	86
G	(1)	*E. coli* inactivation (suspension)	Sharp sheet edges	–	91
GO	Lateral size (6)	*E. coli* inactivation (suspension)	Large lateral size	Large GO > small GO	83
		GSH oxidation	–	Large GO ≈ small GO	
GO	Lateral size (4)	*E. coli* inactivation (suspension)	Large lateral size	Large GO > small GO	58
		E. coli inactivation (surface)	Small lateral size and high defect density	Large GO < small GO	
		GSH oxidation	High defect density	Large GO < small GO	
GO	(1)	*E. coli* inactivation (suspension)	Basal planes (not edges)	–	92
GO	(1)	*E. coli* inactivation (surface)	Basal planes (not edges)	–	93
GO	Chemical composition (5)	*E. coli* inactivation (suspension and surface)	Carbon radical	The GO sample with the highest carbon radical level	84
GO	(1)	*E. coli* inactivation (surface)	High density of exposed edges	Vertical GO > planar GO	94
		GSH oxidation	High defect density	–	
GO	(2)	GSH oxidation	–	GO (C=O and COOH rich) ≈ GO (C-O rich)	95

[a]The use of chemical composition refers to the changes in the C/O ratio and the percent distribution of O-types. [b]The number of unique GM samples studied. [c]*E. coli* inactivation (surface) refers to the antimicrobial activity of G/GO immobilized on a surface substrate/coating.

Note: "–" indicates that the information is not available. ">, ≈, <" refers to superior, equal, inferior, respectively.

While the gram-negative *E. coli* is the most widely studied bacterium to investigate the antibacterial effects of graphene and GO, the effects against other gram-positive bacteria (*Bacillus subtilis,*[91] *Enterococcus faecalis,*[91, 96] *Lactobacillus crispatus,*[84] *Staphylococcus aureus,*[63, 97-99]) and gram-negative bacteria (*Pseudomonas aeruginosa,*[96, 97, 99, 100] *Pseudomonas syringae,*[101] *Salmonella typhimurium,*[91] *Xanthomonas campestris pv. undulosa*[101]) have also been evaluated. In these studies, the antibacterial mechanisms and governing material properties are not unique from those mentioned in Table 1.3 for *E. coli*. Yet, the bactericidal efficiency of graphene/GO arising from the proposed physical mechanisms differs depending on the type of bacteria studied. This arises from differences in the cell wall structure in gram-positive and gram-negative bacterial cells with gram-positive cell possessing a much thicker peptidoglycan layer (20-80 nm) than gram-negative bacteria (7-8 nm), which have an additional lipopolysaccharide outer membrane.[102] The few studies showing graphene/GO is more toxic to gram-negative than gram-positive bacteria attribute the difference to the thicker, and thus more resistant, peptidoglycan layer of gram-positive bacteria.[91] Conversely, more evidence is presented supporting the stronger resistance of gram-negative bacteria against the direct contact with graphene/GO compared to gram-positive bacteria because: [63, 96, 98, 99] i) the outer membrane in the cell structure of gram-negative bacteria serves as a protective layer that can self-repair to retain the cell integrity and reproductivity and can induce repulsion force at the material-bacteria interface due to lipopolysaccharide stretching effects and ii) the thick peptidoglycan layer in the cell structure of gram-positive bacteria behaves as a chelating agent of which the surface proteins can facilitate adherence of materials onto bacteria increasing the cell death.[62, 95, 97, 98] The cell shape and size are additional factors that can influence the bactericidal efficacy of graphene/GO. In general, smaller size of bacteria (e.g., the size of coccus-shaped *Staphylococcus aureus* is smaller than rod-shaped *E. coli)* are less resistant to physical wrapping of graphene/GO and suffer more physical damage than larger bacterial cells.[98, 99]

Taken together, the messages extracted from the compiled study results in Tables 1.2 and 1.3 help identify the research gaps regarding applications of graphene, GO, and NG for electrochemical (ORR and OER) and biological (GSH oxidation and *E. coli* inactivation) activities, including:

i) There are inconsistent findings regarding the identification of governing material properties (e.g., graphene edge versus basal planes, graphitic-N versus pyridinic-N) and the relative magnitude of reactivity between different classes of materials (e.g., GO versus rGO) in respective electrochemical and biological studies. While using a specific parameter (size, shape, chemical composition) to manipulate properties, a systematically modified material set is prepared. Along with a comprehensive characterization of primary material properties (those identified in the literature and compiled in Tables 1.2 and 1.3), material and experimental variables confounding the establishment of property-function and property-hazard relationships will be avoided. It is important to capture the evolution of material properties across the material set to which the changes of outcomes can be correlated back to the governing property(ies) and ultimately, the manipulated parameter. However, tuning chemical composition to create a systematically modified material set with different distributions of oxygen functional groups (C-O-C, C-OH, C=O, COOH) is rarely carried out in the literature in relation to GSH oxidation and bacterial inactivation. More common is a comparison between two samples with different modified extents of the chosen parameter, e.g., GO versus rGO.

ii) Using the same set of materials to evaluate function and hazard in a single study allows for 1) a more robust identification of governing material properties underlying previously reported contradictions, and 2) rationalization of relationships that correlate properties with both function and hazard profiles to inform rational design. Gilbertson, et al. examined electrochemical and biological activities of a systematically modified set of oxygenated multiwalled carbon nanotubes, the results demonstrated the ability to control both activities by manipulating chemical composition.[21, 22] However, studying function in conjunction with hazard for GMs has not been conducted.

iii) While NG has been studied by many researchers for electrochemical applications (particularly for ORR), the role of N-types in mediating two bioactivities remains unknown.

1.2 Dissertation Objectives and Scope

The identified research gaps above motivate the work of this dissertation. The overall objective of this dissertation is to inform the controlled design of GMs by establishing the relationships that correlate material physicochemical properties to their function (electrochemical activity) and hazard (bioactivity). The central hypothesis is that chemical composition, manipulated by functionalizing graphene with heteroatoms (i.e., oxygen and nitrogen) at different levels, is an effective approach to regulate electrochemical and biological activities imparted by GMs.

The following specific aims are completed to realize the overall objective:

i) Develop property-function and property-hazard relationships for GO. This involves systematically manipulating the chemical composition (C/O ratio and O-types) to obtain a GO material set with varying physicochemical properties, comprehensive characterization of material property evolution across the material set to render identification of correlation between properties, evaluation of ORR and GSH oxidation by the GO material set using reliable methods to determine whether chemical composition is a viable approach to control ORR and GSH oxidation, and finally, identifying governing properties for these two activities by correlating trends and establishing the relationships between governing properties, ORR, and GSH oxidation supported by the underlying mechanisms.

ii) Uncover the mechanism of the GO-GSH interaction. This objective employs experimental and computational approaches to identify the oxygen active sites that govern oxidative potential of GO toward GSH oxidation considering all possible interactions between O-groups of GO and the GSH molecule.

iii) Develop property-function and property-hazard relationships for NG. This objective involves systematically manipulating chemical composition (C/N ratio and N-types) to obtain a NG material set with varying physicochemical properties, comprehensively characterizing material property evolution across the material set to render identification of correlation between properties, evaluating two electrochemical activities (ORR and OER) and two bioactivities (GSH oxidation and *E.coli* inactivation) mediated by the NG material set using reliable methods to determine whether N-types play roles in influencing bioactivities and whether chemical composition is a viable approach to control these activities, identifying governing properties for these activities by correlating trends, and establishing their relationships elucidated by the underlying mechanisms.

1.3 Dissertation Organization

Chemical composition is realized as a viable design handle to intentionally manipulate physicochemical properties of GMs. It is critical to identify relationships between specific properties of GMs (O and N active sites and consequential properties resulting from O functionalization and N doping) and activities of interests (electrochemical and biological activities), unveiling the mechanisms for each activity and enabling the potential to maximize functional performance and minimize adverse biological consequences. These outcomes will have a positive impact on the design of safe and highly effective GM-derived products and technologies.

In Chapter 2, the impact of chemical composition on GO is investigated. Thermal annealing and chemical reduction were employed to treat a highly oxidized GO to prepare a set of GO and rGO samples with different distribution of oxygen functional groups. After correlating the trends between characterized properties (percent of O-groups, dispersed aggregate size, defect density, conductivity) and materials' capacity for ORR and GSH oxidation, the results indicate that electrochemical and biological activities are not governed by a sole factor, but are driven by a balance between chemical composition (i.e., presence and type of oxygen functionalities) and consequential physicochemical properties as a function of chemical composition manipulation. While better dispersion (i.e., smaller aggregate size) and higher defect density are demonstrated to be important in influencing the oxidative potential of GO, the C=O moiety and the electrical conductivity collectively govern both electrochemical and biological activities of rGO. These two activities are linked together given the similar underlying mechanisms requiring the adsorption of oxygen and the heterogenous electron transfer, both of which are enhanced by the identified governing material properties.

Given the observed unique trend of GO in mediating GSH oxidation that is different from rGO (in Chapter 2), the interaction mechanism of GO with the GSH molecule is further explored in Chapter 3. In addition to the predominant O_2-mediated catalytic mechanism that was previously reported for carbon mediated GSH oxidation, the focus is on the investigation of direct reaction mechanism between specific O-groups of GO and thiol groups of GSH. The mechanistic resolution is gained by using 1) experimental approach to examine changes in the chemical composition of GO before and after reacting with GSH by XPS and ATR-FTIR, and 2) computational approach in terms of density functional theory to determine relative reaction barriers for all possible GO-GSH reactions. The results highlight the synergistic role of epoxide and hydroxyl groups in directly mediating GSH oxidation. The findings enhance understanding of oxidative stress mechanisms in biological activities for O-functionalized carbon nanomaterials and interactions of these materials with other thiol-containing biomolecules and drugs.

In Chapter 4, the impact of chemical composition on NG is investigated. The hydrothermal method was employed to prepare NG materials and N-types were tuned using different nitrogen precursors (urea and uric acid) and a post thermal annealing treatment at different temperatures. Analyzing the trends between characterized properties (percent of N-types, defect density, surface area) and materials' capacity for ORR, OER, GSH oxidation, and *E. coli* inactivation suggests that all activities are governed by synergistic contributions of multiple properties. The opposite trends are found for ORR and OER, confirming different electron transfer properties between N-types; electron-donating graphitic-N is the promoter for ORR while OER is driven by electron-withdrawing pyridinic-N. The similar trends are observed for GSH oxidation and *E. coli* inactivation, demonstrating predominant oxidative stress cytotoxicity. Further, the similar mechanism between ORR and GSH oxidation and the observed similar trends reveal the contribution of graphitic-N of NG to oxidative stress related bioactivity. The study highlights N-types work differently depending on the specific activity, presenting the opportunity to manage function-hazard tradeoffs toward benign applications of NG.

Finally, Chapter 5 summarizes the key findings in this dissertation, underscores the significance of the work, and proposes recommendations for future research. This dissertation conveys the ability to manipulate chemical composition to advance a growing rational design framework for GMs.

2.0 Informing Rational Design of Graphene Oxide through Surface Chemistry Manipulations: Properties Governing Electrochemical and Biological Activities

This Chapter has been published:

Wang, Y.; Gilbertson, L. M. *Green Chemistry* **2017**, 19 (12), 2826-2838

It is increasingly realized that rational design is critical to advance potential applications and proactively preclude adverse consequences of carbon nanomaterials (CNMs). Central to this approach is the establishment of parametric relationships that correlate material properties to both their functional performance and inherent hazard. This work aims to decouple the causative mechanisms of material structure and surface chemistry as it relates to the electrochemical and biological activities of graphene oxide (GO). The results are evaluated in the context of established relationships between surface chemistry and oxygen functionalized multi-walled carbon nanotubes (O-MWCNTs), a carbon allotrope. Systematic manipulation of GO surface chemistry is achieved through thermal annealing (under inert conditions, 200 – 900 °C). To further elucidate the contribution of several properties, chemical reduction was also used as an approach to differentially modify the surface chemistry. Physicochemical properties of GO and reduced GO (rGO) samples were comprehensively characterized using multiple techniques (AFM, TGA, XPS, ATR-FTIR, Raman, and DLS). The results indicate that surface chemistry is a viable design handle to control both activities. Rather than a single direct property (i.e., relative presence of carbonyl-containing moieties), it is a balance of multiple consequential properties, (extent of dispersion, defect density, and electrical conductivity) in combination with the relative presence of carbonyl moieties that synergistically contribute to electrochemical and biological activities. The identification of these governing physicochemical properties aims to inform the establishment of design parameters to guide the rational and safe design of CNMs.

2.1 Introduction

Rational chemical design motivated by green chemistry has stimulated an impressive body of work in which the function and hazard of chemicals are decoupled at the molecular level.[1, 2, 103, 104] At the core of this rational design approach is the identification of physicochemical properties – ideally those that can be manipulated – that govern the function and hazard. For chemicals, correlations between their structure, physicochemical properties and toxicity manifest as Quantitative Structure-Activity (and Toxicity) Relationships (QSAR and QSTR), which guide chemists in the molecular design process to reduce the inherent hazard through chemical structure and property manipulations.[103] This ‘design of safer chemicals’ approach and the unfortunate history that motivated its emergence, underlines the critical need for proactive development of design guidelines for new and emerging chemicals. Engineered nanomaterials (ENMs) are one such class of chemicals that present tangible benefits and market penetration[49] with potential concomitant adverse environmental and human health consequences.

One- and two-dimensional configurations of carbon nanomaterials (CNMs), including carbon nanotubes (CNTs) and graphene, have captured the attention of researchers due to their unique physicochemical properties. In particular, CNM exceptional electronic properties have advanced a wide range of applications in electronic and electrochemical devices, energy conversion and storage, and sensors.[11, 12, 105-108] The estimated global market of graphene-based products alone are estimated to grow from $1.5 million in 2015 to $310.4 million in 2020.[49] Given their versatile applications and demonstrated significant magnitudes of (cyto)toxicity,[22, 37, 58, 59, 63, 87, 109, 110] concerns have been raised regarding the potential for these materials to impart adverse consequences in the event of the unintended release to the environment and human exposure.[17, 18, 111] The balance of promoting the use of CNMs in promising applications while preventing unintended consequences presents a critical challenge that motivates a rational design approach for sustainable development of promising CNM-enabled products. Similar to chemicals, this balance can be met through the establishment of relationships that relate specific structure and/or material properties to the functional performance and inherent hazard.[5] Interestingly, the electron transport and specific surface functional moieties of CNMs have been shown to be important for both electrochemical and biological activities.[21, 37, 38, 59, 112-114] These properties can be manipulated through their dependence on material structure and surface chemistry. Decoupling the causative mechanism of material structure and surface chemistry in relation to electrochemical and biological activities is thus a critical step toward rational and sustainable CNM design.

Gilbertson, et al. previously demonstrated the ability to control the electrochemical (a desired function) and biological activities of oxygen functionalized multi-walled carbon nanotubes (O-MWCNTs) by manipulating their surface chemistry.[21, 22] In that work, the relative presence of carbonyl moieties was identified as the governing parameter, influencing both biological and electrochemical activities. The research presented herein, aims to determine whether, i) surface chemistry alone governs electrochemical and biological activities of all CNMs, or ii) the activities of CNMs are driven by unique material properties (e.g., structure, electronic). Given the chemical similarity and distinct structure of CNTs and graphene, the surface chemistry of graphene is manipulated in the same way as the previously studied O-MWCNTs (i.e., oxygen functionalization) to produce a systematically modified graphene oxide (GO) material suite. The comparison of governing physicochemical properties on the corresponding electrochemical and biological activities within these two CNM allotropes will thus inform the potential establishment of guidelines for the controlled and tailored design of CNMs.

Like graphene, GO consists of a single atomic plane of carbon arranged in a network of sp^2- carbons decorated with different oxygen moieties, including epoxide and hydroxyl groups on the basal planes and carboxylic and carbonyl groups at the edges.[34, 35] Surface functionalization introduces a hybrid structure consisting of variable sp^2 and sp^3 carbon bonding schemes.[34, 35] The balance of sp^2-sp^3 carbons directly influences the electronic properties (e.g., conductivity) thus, presenting an opportunity to tailor these properties of graphene by manipulating specific oxygen groups of GO.[48, 115, 116]

A critical underpinning of the proposed rational design approach is the establishment of a systematically modified and comprehensively characterized material suite, which further enables movement beyond the reported inconsistencies of graphene and GO biological activity (Table 1.3). Two approaches, thermal annealing and chemical reagent reduction, were used in this work to prepare a series of reduced GO (rGO) samples from the same starting GO. Thermally reduced GO samples with varying surface chemistries were obtained through selective reduction of oxygen functional groups – based on their thermal stability on carbon surfaces[117] – by varying the maximum temperature from 200 to 900 °C. One chemically reduced GO sample was prepared through deoxygenation with sodium borohydride ($NaBH_4$). Comprehensive characterization is necessary to establish governing relationships between specific material properties and the desired function and hazard outcomes. In addition to standard approaches to characterize the structure, physical and chemical properties, significant attention is given in this study to the biological and electrochemical activities, which are characterized using independent approaches. The trends in electrochemical and biological activities are correlated with the specific GO/rGO physicochemical properties, including extent of dispersion (measured as aggregate size and distribution), defect density, electrical conductivity, and the relative presence of different oxygen functional groups. The balance of these contributing properties is discussed as it relates to the identified trends in the measured electrochemical and biological activity endpoints.

2.2 Materials and Methods

2.2.1 Preparation of Graphene Oxide and Reduced Graphene Oxide Material Suite

Graphene Oxide (GO). Powdered single layer GO (~99% purity), synthesized using the modified Hummer's method, was purchased from ACS Materials LLC (Medford, MA, USA, Product No. GNO1P005), and used as-received (ARGO).

Reduced GO (rGO) Samples via Thermal Annealing. Systematic surface modified GO was prepared by a thermal treatment under helium gas flow in a tube furnace (Thermo Scientific Lindberg/Blue M TF55035A-1) with custom-built quartz tube at increasing maximum temperatures 200, 400, 600 and 900 °C. The ARGO was added to the quartz tube and heated at a rate of 5 °C min^{-1} to the maximum temperature, held for 30 min, and then left to cool at room temperature (under He flow). These thermally reduced GO samples are henceforth referred to as TGO200, TGO400, TGO600, and TGO900, respectively.

Chemically Reduced GO. The chemically reduced GO (CGO) sample was prepared using the method of Gao, et al.[118] Briefly, 100 mg of ARGO was dispersed in 100 mL deionized water by 30-min bath sonication (VWR Aquasonic 150T). After sonication, the pH of the ARGO dispersion was adjusted to 9.5 using 5 wt% sodium carbonate (Na_2CO_3). 20 mL of 40 g L^{-1} $NaBH_4$ was added and the mixture was heated to 80 °C under constant stirring for 1 hour. The final CGO sample was isolated by filtration, rinsed ten times with 250 mL deionized water, and dried in a vacuum desiccator with phosphorous pentoxide for 48 hours. This chemical reduction method was chosen because it avoids using a hazardous reducing reagent (e.g., hydrazine) and further, precludes the incorporation of functional groups, such as C-N groups with hydrazine reduction, limiting the potential for impurities in the final product.[118, 119] Since the CGO sample was prepared using $NaBH_4$ and boron-doped CNMs are known efficient electrocatalysts,[120, 121] the potential for boron to confound the electrochemical activity of CGO was investigated by XPS (Figure 2.1). The results confirm the absence of boron in the CGO sample.

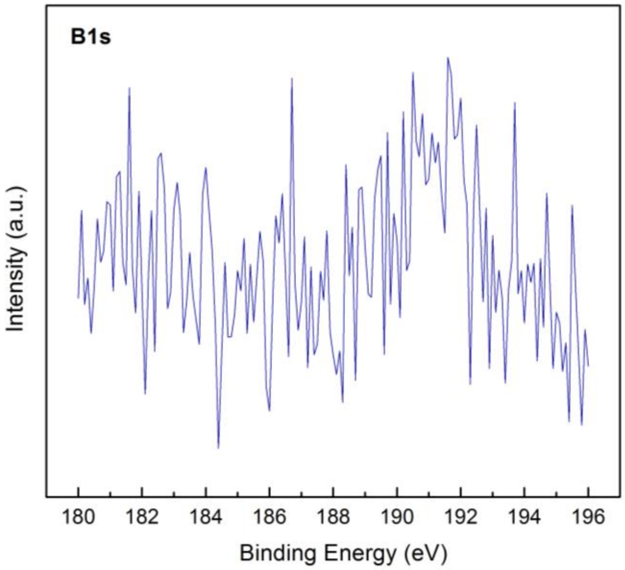

Figure 2.1 High resolution XPS spectrum of the boron region (B1s) for CGO. No peak signal was detected, indicating the absence of boron in the CGO sample.

2.2.2 Characterization of the Prepared Samples

ARGO, TGOs, and CGO were characterized using atomic force microscopy (AFM, to evaluate potential changes in the lateral dimension and sheet height before and after reductive treatments), thermogravimetric analysis (TGA, to determine the thermal stability and purity of ARGO), X-ray photoelectron spectroscopy (XPS, to quantify the surface chemistry and distribution of functional groups via C-O bonding schemes), attenuated total reflectance-Fourier transform infrared spectroscopy (ATR-FTIR, to confirm the changes in surface chemistry as a complementary technique to XPS), and Raman spectroscopy (to determine the degree of disorder or defect density and the crystallite size). The electrical conductivity of GO/rGO samples was determined using the four-point technique. The methodological details of these techniques are shown below.

AFM. AFM images were taken in tapping mode with an Asylum MFP-3D AFM equipped with a MikroMasch NSC14 silicon cantilever (5.7 N/m force constant and a resonance frequency of 160 kHz). The sample for AFM was prepared by drop-casting 3 μL of a GO/rGO suspension (25 μg mL^{-1}) on a 1.5 cm × 1.5 cm silicon wafer previously cleaned by acetone, methanol, isopropanol, and plasma oxygen. The Asylum research MFP-3D software was used to determine the sheet height and lateral size distribution by counting approximately 100-150 sheets captured in multiple similar images.

TGA. Thermal stability and purity of ARGO was evaluated by a SDT-Q600 thermal analyzer (TA Instruments, New Castle, DE, USA) under nitrogen and air atmospheres, respectively. Samples were held at 100 °C for 30 min to remove the adsorbed water molecules. The temperature was then increased to 1000 °C at a heating rate of 5 °C min^{-1}.

XPS. Surface chemistry and elemental composition of all samples were evaluated by XPS. Approximately 3 mg of GO/rGO sample was dusted onto the sample holder covered with double-sided copper tape and then loaded into a Thermo Scientific ESCALAB 250Xi instrument with monochromatic Al Kα X-ray source (1486.7 eV, spot size 650 μm). A flood gun was used to compensate the surface charge in the case of measuring the insulating or weakly conductive samples, whereby the charges accumulating at the surface from the emission of electrons are neutralized by replenishing electrons from this external flood gun. Survey spectra were collected using a pass energy of 150 eV with a step size of 1.0 eV, and high-resolution spectra for C1s and O1s were collected using a pass energy of 50 eV with a step size of 0.1 eV. At least three measurements in different locations of each sample were carried out. Thermo Scientific Avantage software was used for peak fitting and to calculate the atomic percentage. Spectra were subtracted with a Smart background, which is a Shirley-derived background with the constraint that any point of the actual data should be of a higher intensity than the background. After background subtraction, a mixed Gaussian-Lorentzian product function was used to deconvolute the peaks. In the process of performing the deconvolution to high-resolution C1s spectra, each spectrum was calibrated with respect to the sp^2 component at 284.8 eV. Peak positions were constrained to shift within ±0.2 eV from the assigned binding energy and values of full width at half maximum (FWHM) for all major components were fixed at the same level with ±0.2 eV deviation.

ATR-FTIR. Changes in surface chemistry as a function of treatment was further evaluated/confirmed by ATR-FTIR. The spectra were recorded by a FTIR spectrometer (Bruker VERTEX-70LS) and the attached ATR accessory was equipped with ZnSe crystal, the spectral region was scanned from 600 - 4000 cm^{-1} 150 times with 4 cm^{-1} resolution.

Raman. Raman spectra were acquired on a Horiba Scientific XplorA Raman-AFM/TERS system using a 638-nm laser for excitation. At least three measurements were performed at different locations of each sample. The intensities, FWHMs, and positions of D and G peaks were determined by performing a polynomial baseline subtraction, and then fitting D peak with a Lorentzian character and G peak with a Breit-Wigner-Fano (BWF) function owing to its asymmetry shape.[122, 123]

Electrical Conductivity Measurement. Thin films of GO/rGO samples were prepared for electrical conductivity measurements. 50 mL GO/rGO suspension (0.3 mg mL^{-1}) was vacuum filtered using a mixed cellulose eater membrane (Millipore) and then dried in a vacuum desiccator with phosphorous pentoxide for 24 hours. The sheet resistance of fabricated films was measured using a four-point probe system (Jandel, Model RM2) connected to a Keithley multimeter for a more accurate display. The film thickness was measured using scanning electron microscopy (SEM, Zeiss Sigma 500 VP). The prepared films were treated with liquid nitrogen to prevent disruption during cutting of the sample (at the measurement sites) to obtain a cross section for thickness determination. The electrical conductivity of samples was obtained from the inverse of the resistivity as determined by both the sheet resistance and the film thickness.

2.2.3 Biological Activity Using the Oxidation of Glutathione (GSH) Assay

GSH was used in this study to evaluate the relative biological activity of the differentially treated GO/rGO samples following a previously described method.[22, 58, 124] GO/rGO dispersions, 0.025 or 0.050 mg mL^{-1} (two concentrations were studied to evaluate mass-dependence), were prepared by bath sonication (VWR Aquasonic 150T) for 30 min in 33 mM bicarbonate buffer (pH=8.6), after which GSH stock solution was added to the prepared triplicate samples to yield a final concentration of 0.4 mM. Next, the sample vials were covered with aluminum foil to avoid potential photo-induced oxidation, and placed on a rotator for continuous rotation for the duration of the experiment. An aliquot was removed at specific time points and filtered (0.22 µm syringe filter) to prevent potential confounding interaction with Ellman's reagent and potential interference with absorbance measurements. Ellman's reagent (5,5'-dithio-bis-(2-nitrobenzoic acid)) was added, which reacts with thiol group of GSH, to produce a yellow product. The absorbance (412 nm) was measured and then used to determine the concentration of GSH remaining in solution. The percent loss of GSH was calculated by comparing with the negative control (no GO/rGO). Statistical analysis of the results included two-sample *t* test with a 95% confidence interval (CI) and a 0.05 level of significance (*P* value).

The dispersed aggregate size and size distribution was determined by dynamic light scattering (DLS) using a Litesizer 500 (Anton Paar, Austria). Zeta potential was determined using the same instrument and determined by electrophoretic light scattering (ELS). The GO/rGO materials were prepared in the experimental media used for the GSH experiment (no addition of GSH) and transferred to disposable cuvettes for particle size measurements, and to omega cuvettes for zeta potential measurements. The size distribution was determined using a multiexponential fit of the correlation function with a Tikhonov regularized non-negativity constraint, which generates a size distribution without any assumption of the shape (e.g., normal distribution is not assumed). Furthermore, this advanced cumulant method can generate multimodal size distributions and thus, is particularly useful for heterogenous samples where more than one main particle (or aggregate) size is present. Smoluchowsiki approximation was adopted to calculate the zeta potential from electrophoretic mobility based on Henry equation, which is commonly used for lamellar-type materials like GO.[125, 126]

2.2.4 Electrochemical Measurements

Rotating ring-disk electrode (RRDE) technique was employed for electrochemical characterization of the prepared GO/rGO samples using a WaveDriver 20 Bipotentiostat (PINE Research Instrument, NC, USA) and a PINE modulated speed rotator. A three-electrode cell was used in all measurements with a platinum counter electrode, an Ag/AgCl reference electrode, and a sample modified RRDE glassy carbon working electrode. The working electrodes were prepared as follows: i) GO/rGO inks were prepared by mixing 2 mg of GO/rGO, 792 µL isopropanol, 8 µL of Nafion (5 wt%) and 1.2 mL deionized water followed by one hour tip/probe sonication (Branson S-450 digital ultrasonic homogenizer) to form a well-dispersed suspension, ii) 10 µL of the dispersed mixture was carefully drop cast onto the glassy carbon disk electrode surface (0.1963 cm^2) and left to dry (approximately 2 hours).

1 M KOH electrolyte solution was used for all oxygen reduction reaction (ORR) experiments. Prior to each measurement, the electrolyte was bubbled with nitrogen for at least 30 min and the working electrode was cleaned by cyclic voltammetry (CV) for 25 cycles sweeping from 0.2 to -1 V. Next, the electrolyte was saturated with oxygen for 30 min before performing RRDE voltammetry.

RRDE voltammetry was conducted from 0.2 to -1 V at a scan rate of 5 mV s^{-1} with varying rotating speeds of 400, 625, 900, 1600, and 2500 rpm. The ring potential was held at 0.5 V. By collecting the polarization curves at each rotating speed, the kinetic limiting current density (J_K, mA cm^{-2}) during ORR was determined based on the Koutecky-Levich (K-L) equation:[79, 127-129]

$$\frac{1}{J} = \frac{1}{J_L} + \frac{1}{J_K} = \frac{1}{B\omega^{1/2}} + \frac{1}{J_K} \tag{2-1}$$

where,

$$B = 0.62nFC_0(D_0)^{2/3}\nu^{-1/6} \tag{2-2}$$

$$J_K = nFkC_0 \tag{2-3}$$

J is the measured current density (mA cm^{-2}), J_L is the diffusion limited current density (mA cm^{-2}), B is the Levich constant, ω is the rotating speed (rad s^{-1}), n is the electron transfer number during ORR, F is the Faraday constant (96,485 Coulomb mol^{-1}), C_0 is the bulk concentration of dissolved oxygen in 1 M KOH solution (0.84×10^{-6} mol cm^{-3}),[22, 130] D_0 is the diffusion coefficient of dissolved oxygen in 1 M KOH solution (1.65×10^{-5} cm^2 s^{-1}),[22, 130] ν is the kinetic viscosity of the electrolyte (0.01 cm^2 s^{-1}). By plotting J^{-1} versus $\omega^{-1/2}$ at different electrode potentials, the J_K can be obtained by extrapolating K-L lines to yield intercepts.

The electron transfer number (n), determined using RRDE technique is more accurate than that using the K-L plots. While the K-L method requires the reaction to be one-step and n to be constant at certain potentials from theoretical viewpoint, RRDE is able to directly measure the amount of H_2O_2 during ORR process and not required to fulfill the assumptions of the K-L method.[128, 131] Therefore, n and the percentage of H_2O_2 released during ORR were determined using the following equations:[79, 127-129]

$$n = \frac{4I_D}{I_D+\frac{I_R}{N}} \tag{2-4}$$

$$\%H_2O_2 = 200 \times \frac{\frac{I_R}{N}}{I_D+\frac{I_R}{N}} \tag{2-5}$$

where I_D is the measured disk current (mA), I_R is the measured ring current (mA), and N is the H_2O_2 collection coefficient at the ring (25.6%, provided by PINE Research Instrument).

Electroactive surface area of the prepared GO/rGO working electrodes was determined by CV using 10 mM $Fe(CN)_6^{3-/4-}$ in 1 M KCl under N_2 flow, and then estimated using the following Randles-Sevcik equation modified for quasi-reversible redox process,[80, 132, 133]

$$I_P = 2.99 \times 10^5 n(\alpha n_a)^{1/2} A C D^{1/2} \upsilon^{1/2} \tag{2-6}$$

where A is the electroactive surface area (cm^2), I_P is the peak current (A), n is the electron transfer number during the redox reaction (n=1 for the $Fe(CN)_6^{3-/4-}$ redox process), α is the transfer coefficient and assumed to be 0.5,[133] n_a is the number of electrons involved in the charge transfer step (n_a=1), C is the bulk concentration of the reactant (mol cm^{-3}), D is the diffusion coefficient of the reactant (cm^2 s^{-1}), and υ is the scan rate (V s^{-1}). CV measurements were carried out from 0.6 to -0.1 V with various scan rates from 50 to 270 mV s^{-1}. By plotting I_P versus $\upsilon^{1/2}$, A can be calculated from the slope of the line.

2.3 Results and Discussion

2.3.1 Probing the Lateral Size and the Height of GO/rGO Samples by AFM Imaging

AFM imaging was carried out to, i) confirm the single layer conformation of ARGO, and ii) reveal any changes in lateral size and height of the samples upon reductive treatments (Figure

2.2). The isolated ARGO flakes are found to have an average sheet height of 1.34 ± 0.57 nm, indicating that ARGO sheets are single-layered.[134, 135] The average sheet heights of TGO600 and CGO are around 2.55 ± 1.74 and 4.46 ± 3.62 nm, respectively. The individual single-layer sheets still exist in these two rGO samples, however, disordered clusters can be observed and form by random aggregation of these single-layer sheets in accordance with other studies.[136, 137] Thus, the rGO samples include a mix of single- and multi-layer sheets as well as aggregated rGO sheets. In addition, the average lateral size of ARGO, TGO600, and CGO were determined to be 186 ± 103, 191 ± 128, and 239 ± 155 nm, respectively, and is based on analysis of approximately 100-150 sheets captured from multiple acquired images (Figure 2.2). Although there is a range in lateral size distributions, the GO/rGO sheets being investigated are smaller than 1 μm.

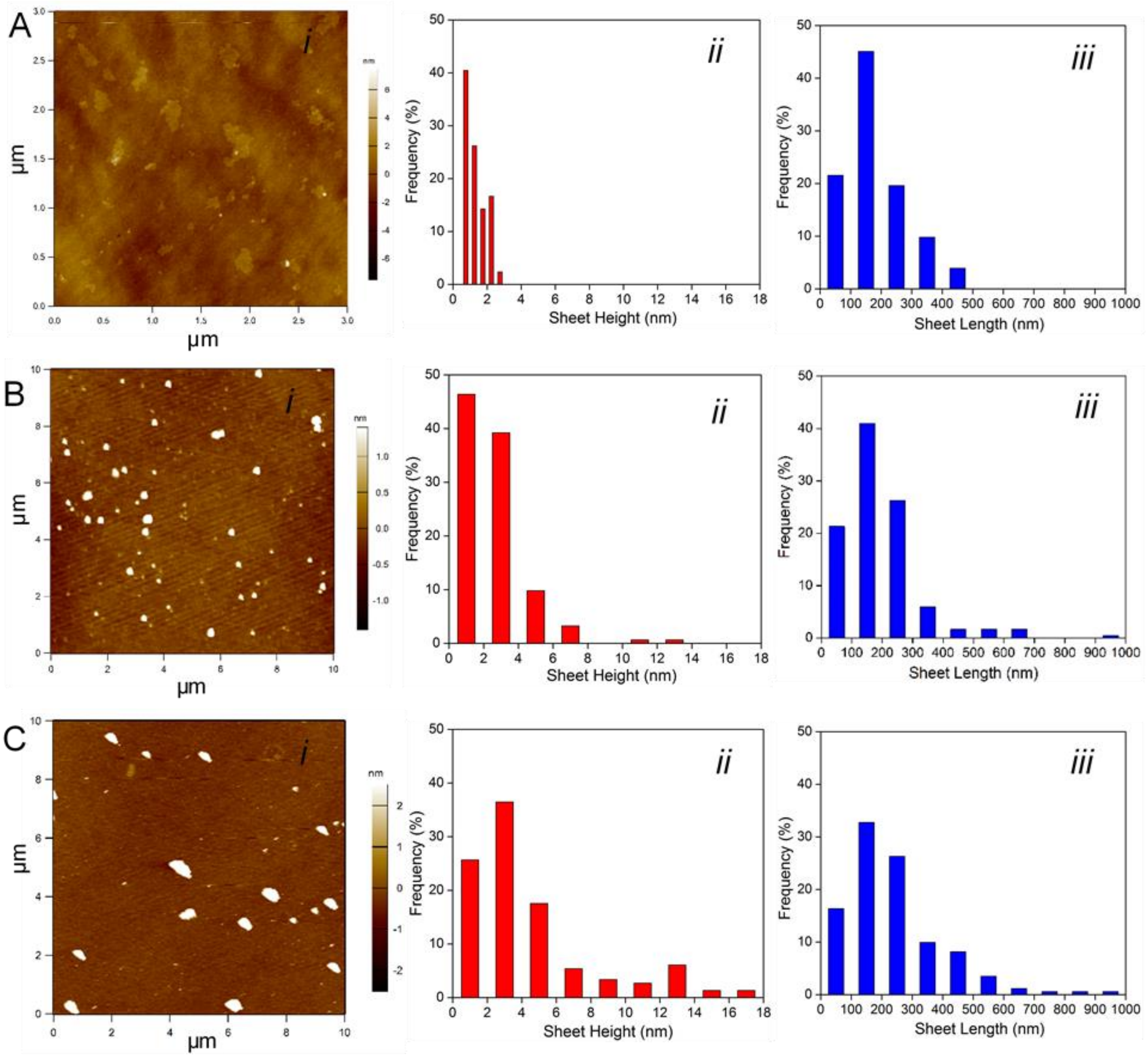

Figure 2.2 AFM characterization of (A) ARGO, (B) TGO600, and (C) CGO, including representative AFM images (i), sheet height distribution (ii), and lateral size distribution (iii). The histograms were obtained by counting approximately 100-150 sheets captured in multiple images of each sample.

2.3.2 Characterizing Surface Chemistry as a Function of Thermal and Chemical Reduction to Inform the Potential to Tailor GO/rGO Physicochemical Properties

Thermal and chemical reduction processes were explored as mechanisms to control graphene surface chemistry and the potential to serve as a path towards tailoring resultant physicochemical properties. As such, comprehensive characterization of surface chemistry is critical and was characterized using multiple complementary techniques, including TGA, XPS, and ATR-FTIR. The results from each will be discussed in turn as it relates to elucidating distinct GO/rGO surface chemistries.

TGA monitors the sample mass during temperature cycling, and can be evaluated under different gas environments. Here, the sample mass loss was determined under nitrogen (N_2) and air to evaluate the thermal stability and the purity of ARGO. The significant mass loss (~ 40%) observed between 100 and 200 °C under N_2 atmosphere (Figure 2.3) is attributed to the release of CO and CO_2 from the decomposition of labile oxygen surface groups (e.g., water molecules, epoxides).[138] The systematic mass loss above 200 °C indicates the subsequent loss of more stable oxygen functional groups.[139] Complete oxidation of ARGO occurs around 500 °C under air; over 95% mass loss indicates minimal residue and high purity of ARGO.

XPS was employed to further resolve the reduction in total surface oxygen (C/O atomic ratio in Table 2.1) and the type of surface oxygen (remaining columns in Table 2.1) as a function of thermal and chemical reduction. These data are compiled in Table 2.1 and determined from peak deconvolution of the high-resolution C1s spectra shown in Figure 2.4. The C1s spectrum of the ARGO exhibits well defined double peaks with sp^2 and sp^3 carbon components (~ 284.8 eV and 287.0 eV, respectively)[140], indicating the presence of a large amount of sp^3 carbon (i.e., presence of functional groups). After thermal or chemical reduction, the C1s spectrum shifts to a single sharp peak at *sp*^{2} carbon position owing to the restoration of *sp*^{2} bonding.[35] The C/O atomic ratio – the metric commonly used to indicate the relative presence of oxygen functionalization of different oxidized carbon samples – increases, as expected, with maximum annealing temperature (ARGO to TGO900), reaching 5.80 for the sample annealed at 900 °C. The CGO C/O ratio increases from 1.58 (ARGO) to 3.52, which is equivalent to that of TGO400. The observed increase of the C/O ratio confirms the effective reduction of surface oxygen and the relative extent of reduction for the methods employed.

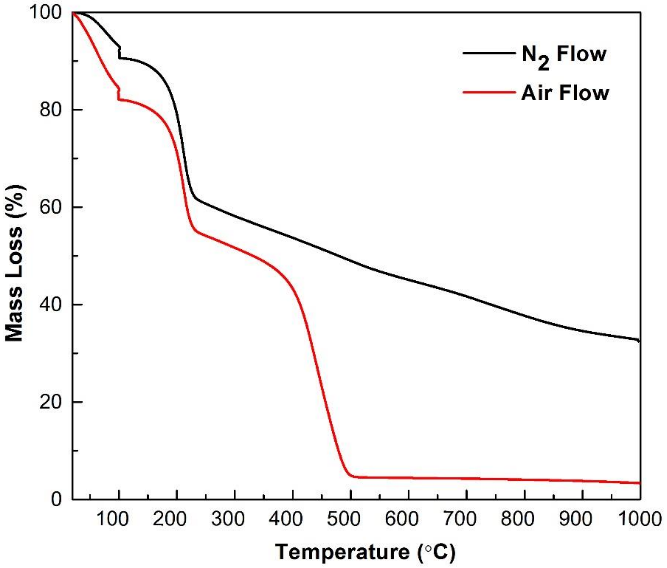

Figure 2.3 TGA curves of ARGO under nitrogen and air atmosphere.

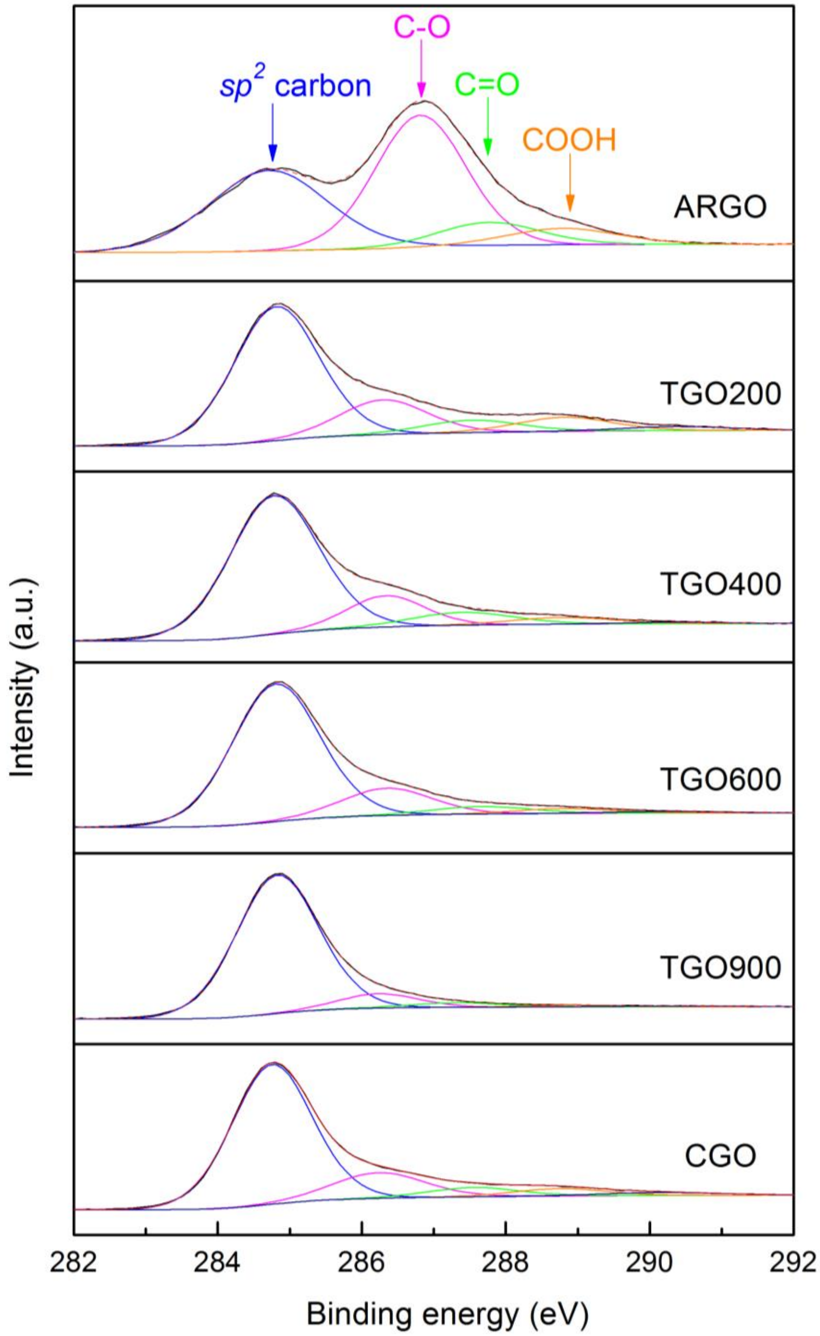

Figure 2.4 XPS high-resolution C1s spectra for ARGO, TGOs, and CGO. Peak deconvolution was completed using four representative peaks for the sp^2 carbon and the respective C-O bonding schemes as indicated by the different color curves. Three C1s spectra were collected at different locations of each sample, peak deconvolution was performed for each C1s spectrum and the average values for four components were compiled in Table 2.1.

Table 2.1 Compiled XPS data representing the C/O atomic ratio, the atomic percent of the graphitic carbon content (sp^2 carbon) and the different C-O bonding schemes representative of different functional groups (C-O, C=O, and COOH) determined from the component fitting of the C1s envelope for ARGO, TGO, and CGO samples.

Samples	C : O	% sp^2 carbon	% C-O	% C=O	% COOH
ARGO	1.58±0.04	36.98±0.70	47.48±0.92	8.74±0.63	6.79±0.48
TGO200	3.04±0.07	68.74±1.18	14.68±2.21	8.48±0.97	8.11±0.31
TGO400	3.52±0.04	73.28±0.73	16.03±1.51	6.91±0.92	3.79±0.25
TGO600	3.68±0.06	76.50±0.09	15.62±0.32	4.74±0.18	3.14±0.10
TGO900	5.80±0.13	86.72±1.74	9.08±1.71	3.21±0.16	1.00±0.21
CGO	3.52±0.05	74.49±0.39	15.67±0.08	5.50±0.12	4.35±0.32

Peak fitting of the C1s spectra can further resolve the various carbon-oxygen bonding schemes, including unoxidized sp^2 carbon (~284.8 eV), hydroxyl and epoxide (C-O, ~286.4 eV), carbonyl (C=O, ~287.5 eV), and carboxylic acid (COOH, ~288.8 eV) groups, to provide additional insight into the type of oxygen on the prepared graphene surfaces. The assignment of these four features is in agreement with the previous studies.[35, 48, 141-143] The sp^2 carbon fraction confirms the degree of reduction, the trend of which should (and does here) coincide with that of the C/O ratio, indicating the restoration of the aromatic (sp^2) carbon structure. As the electrical properties of CNMs are primarily determined by the π electrons of sp^2 carbon[144], changes in the sp^2 carbon fraction can significantly influence the GO/rGO reactivity. The percent contribution of C-O (Table 2.1) indicates it is the major bonding scheme present on ARGO and that upon reduction, the C-O fraction significantly decreases (47.48% for ARGO to 14.68% for TGO200 and 15.67% for CGO). This is attributed to reduction of epoxide groups, which are most abundant on GO[35, 48, 145] and are neither thermally nor chemically stable. For TGO900, the relative contribution of the C-O bonding scheme is highest, which may be attributed to the stability of C-OH groups at high temperature, particularly those that are intercalated into interlayers of graphene domains.[35, 142] Above 200 °C, the C=O and COOH moieties exhibit a steady decrease upon thermal reduction.

The O1s spectra (Figure 2.5) complement the C1s spectral observations and trends. There are two primary core-level components of the O1s spectra, the single-bonded C-O species (~533 eV) and double-bonded C=O species (~531 eV).[48, 146] These two components are clearly visible during reduction processes, and remain in the spectra of the TGO900 and CGO samples. This indicates that both the thermal and chemical reduction methods employed do not completely regenerate pure graphene. Rather, residual oxygen remains on the surface, consistent with the findings from peak deconvolution of C1s spectra. Combined, the XPS data indicate that thermal and chemical reduction processes, i) are successful at systematically reducing the total amount of surface oxygen, and ii) provide an approach to tailor the functional group composition (i.e., relative amount of different groups).

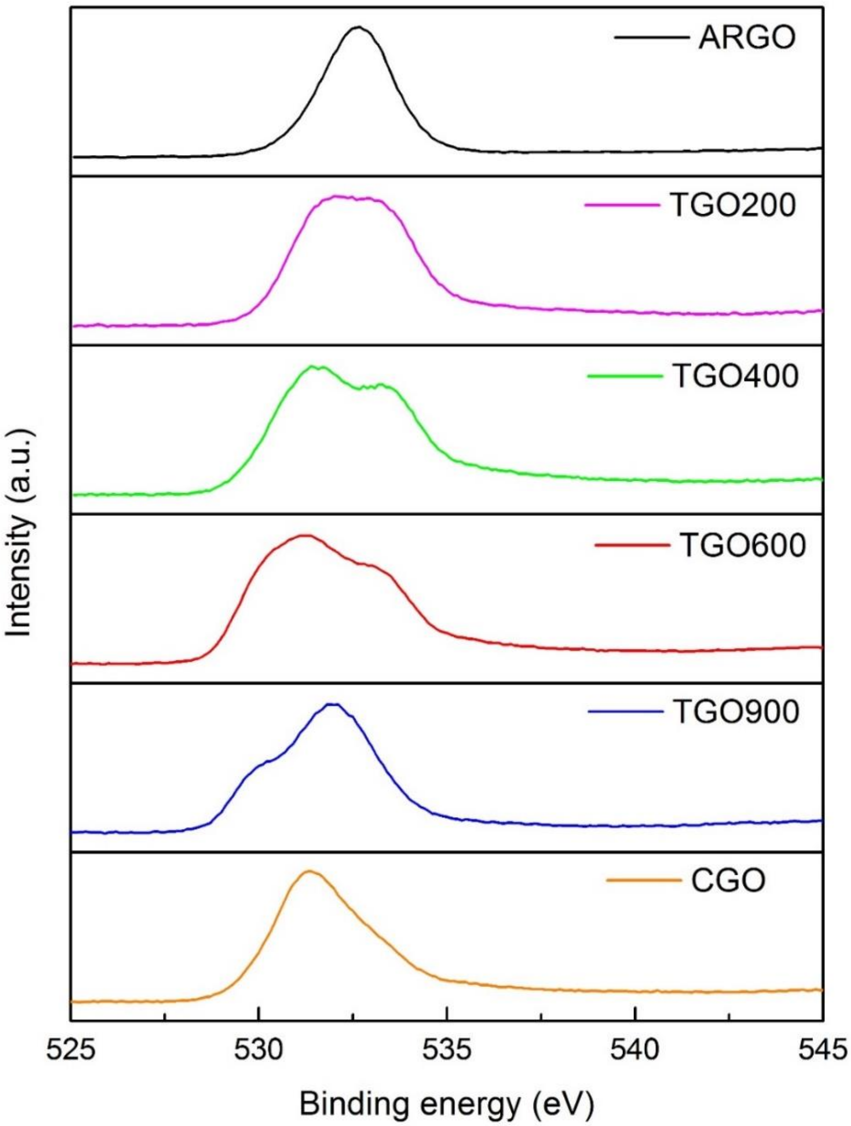

Figure 2.5 High-resolution O1s spectra of ARGO, TGOs, and CGO.

ATR-FTIR provides complementary insight into surface chemistry and confirms the trends observed by XPS.[147] Compiled spectra are shown in Figure 2.6. The observed peaks are assigned to characteristic functionalities, as will be described, and consistent with previous reports.[143, 147-150] A broad peak in the 3000 to 3700 cm^{-1} region denotes the -OH stretching mode, which is attributed to bound water molecules, hydroxyl and carboxylic acid groups. Upon reduction, this band is significantly reduced as seen for rGO samples in this region. The two peaks in the region from 1550 to 1730 cm^{-1} correspond to the carbonyl (C=O) stretching mode that arises from the ketone and carboxylic acid groups. While it is challenging to differentiate the contributions of each, the relative intensity of this peak upon reduction confirms the corresponding XPS trends. Significant reduction in the C=O intensity is observed for the TGO600 and TGO900 samples. Peaks within the 980-1150 cm^{-1} region generally represent epoxy (C-O-C) and alkoxy (C-O) bands. C-O moieties decrease remarkably under higher temperature reduction, and evolve as the prominent peak for TGO900, suggesting there are still some carbon-oxygen groups remained even after 900 °C thermal reduction. Indeed, characteristic features localizing in this low-wavenumber region may originate from a number of species including epoxides, ethers, hydroxyls, carboxyls and ketones due to overlapped frequencies.[147] Collectively, it is evident to note the sequent removal of functional groups from the ATR spectra, confirming the XPS results.

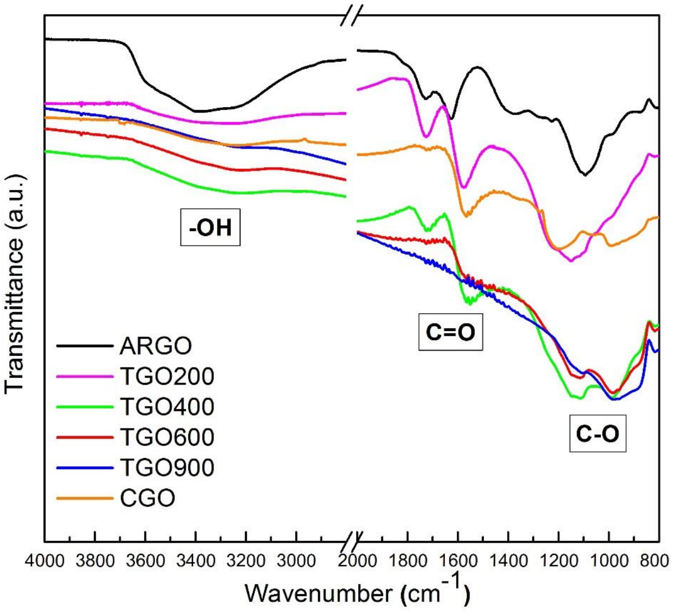

Figure 2.6 ATR-FTIR spectra of ARGO, TGOs, and CGO.

2.3.3 Quantifying Defects and Restoration of the Aromatic Carbon Domain by Raman Spectroscopy

Raman is a widely used tool to study the crystal structure and examine the degree of disorder or defects in carbonaceous materials. Raman spectra were collected for all samples and are compiled in Figure 2.7. There are two prominent peaks at ~1350 cm^{-1} and ~1585 cm^{-1}, representative of the D- and G-band, respectively. The D-band arises from the breathing modes of six-membered rings and the intensity indicates the presence of defects. These defects include *sp*^{3} carbons, bond-angle or bond-length disorders, edge defects, grain boundaries, vacancies, or even physical defects like holes and wrinkles.[126, 151, 152] The G-band originates from the in-plane *sp*^{2} carbon stretching mode of the graphene lattice.[151] In addition, there is a lower magnitude broad bump-like peak observed at high wavenumbers (2400-3250 cm^{-1}) that is representative of the 2D region, including several characteristic bands denoted as 2D (~2700 cm^{-1}), D+G (~2930cm^{-1}), and 2G (~3170 cm^{-1}) bands.[126, 152, 153] It has been reported that the emergence of the modulated bump in the 2D region indicates the existence of a large amount of defects; this high disorder results in the suppression of the 2D band, reducing its intensity.[153, 154] The Raman spectra for all samples present this broad peak at high wavenumbers.

The relative intensity ratio of the D and G band (I_D/I_G) is a commonly used metric to characterize the level of defects. Further, it can be used to evaluate the crystallite size of the basal planes (L_a) and the distance between the defects (L_d).[155-157] An increase in the I_D/I_G is commonly observed upon reduction of GO[36, 126, 152, 158, 159], and is in agreement with results presented here as shown in Figure 2.8 (left axis). Both reduction approaches result in an increase in the I_D/I_G ratio, with that of TGOs systematically increasing with increasing annealing temperature (1.28 – 1.92 from ARGO to TGO900). Previous studies attributed this increase in I_D/I_G of rGO to an increase in structural defects (e.g., holes) and a decrease in the average size of the sp^2 domain according to the Tuinstra–Koenig equation ($I_D/I_G \propto 1/L_a$).[36, 126, 152, 158, 159] However, there is a competing explanation of the defect-induced D band[154, 157, 160] in which the resulting I_D/I_G ratio is a function of L_a and L_d, and the I_D/I_G dependence on each is differentiated by two stages. Stage 2 is characterized by the increase in I_D/I_G with increasing L_d, up to L_d ~3 nm and L_a ~2 nm where I_D/I_G reaches the maximum and signifies the boundary between stage 2 and stage 1. Stage 1 is characterized by a decreasing trend in I_D/I_G as L_d increases, defined by $L_d > 3$ nm and $L_a > 2$ nm. As a result, the increase of I_D/I_G can be explained by either a decrease or increase in defect density depending on mechanistic explanation and the regime to which the materials belong.

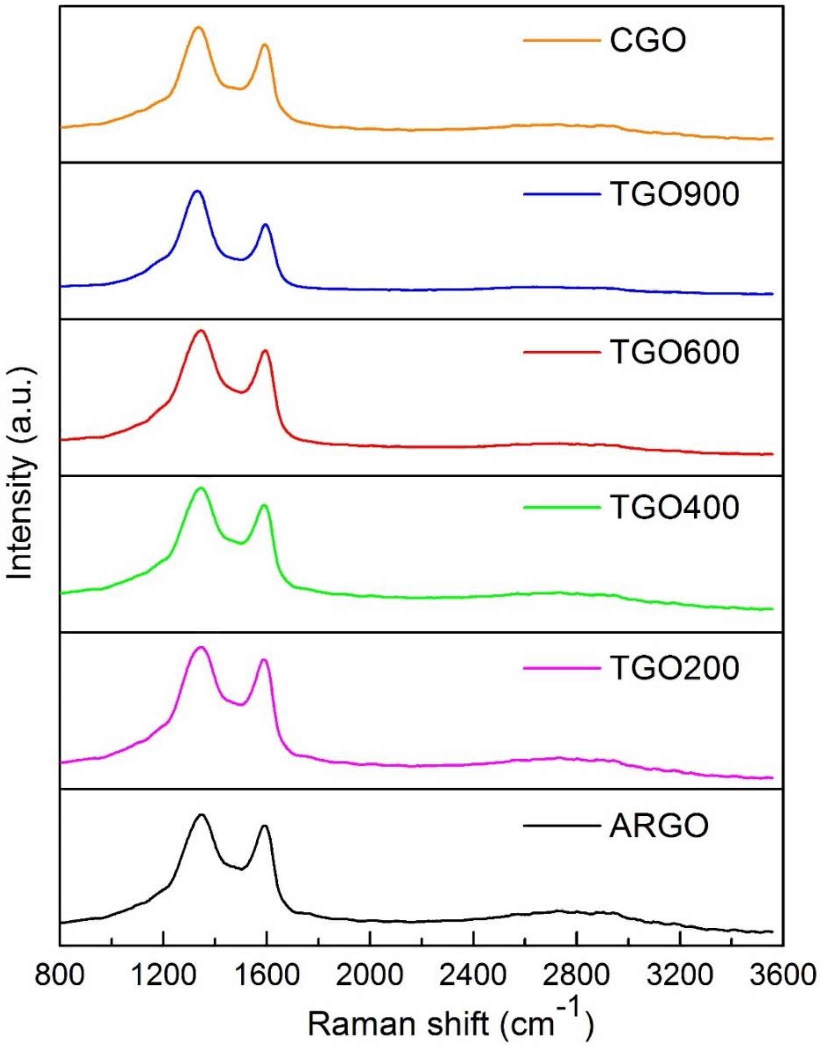

Figure 2.7 Raman spectra of ARGO, TGOs, and CGO.

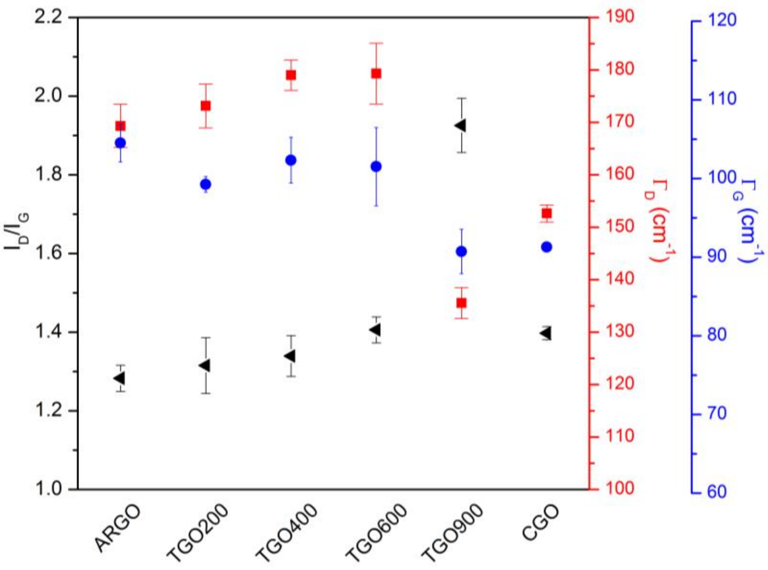

Figure 2.8 Variation of the I_D/I_G values, the FWHM of D band (Γ_D) and the FWHM of G band (Γ_G) for ARGO, TGOs, and CGO. I_D/I_G, Γ_D, Γ_G are displayed by black triangles, red squares and blue circles, respectively. Triplicate measurements in different locations of each sample were carried out and the error bars represent the standard deviation of repeated measurements.

In stage 1, which is indicative of the nanocrystalline phase and referred to as the low defect density regime, the Tuinstra–Koenig relationship is valid and the increase of I_D/I_G corresponds with a decrease in L_a and L_d. Conversely, in stage 2, which represents the high defect density regime, the Tuinstra–Koenig relationship fails and the increase of I_D/I_G infers an increase in L_a and L_d. Before conducting an evaluation of the prepared GO/rGO material suite in the present study, it is important to first identify the appropriate regime (i.e., stage 2 or stage 1) by analyzing Raman spectra. The broad bump-like peak in the 2D region and the full width at half maximum (FWHM, Γ) of G band (Γ_G) (~90-100 cm^{-1}) displayed in our samples are characteristics of stage 2.[156, 157, 161] Thus, the I_D/I_G increase with the increase in the level of reduction, from ARGO to TGOs or CGO, indicates the improvement in ordering and the formation of more defect-free sp^2 domains of larger size. In other words, the ARGO experiences a transformation from small sp^2 clusters interspersed by an amorphous and highly disordered sp^3 matrix to a larger sp^2 carbon network upon systematic reduction of oxygen function groups. In addition, while the Γ_D and Γ_G do not change significantly from ARGO and TGOs annealed below 900 °C, there is a significant decrease in both Γ_D and Γ_G for the TGO900 and CGO samples. This indicates that these reduction conditions are effective at 'healing' the GO defects. Finally, the TGO sample of comparable sp^2 carbon fraction to that of the CGO sample (TGO600, Table 2.1) has distinct Γ_D and Γ_G, which suggests that chemical reduction produces samples with relatively lower structural disorder than the thermal reduction.

2.3.4 Investigating the Electron Transfer Capability of GO/rGO Samples Through Conductivity Measurements

Given that the electronic properties of CNMs are important for both electrochemical and biological activities[22-26], the electron transfer capability of the prepared GO and rGO is evaluated here, quantified by the sample conductivity. Further, the electrical conductivity indicates how the π electron network of sp^2 carbons is restored upon reduction. The functional groups and defects on the GO disrupt the conjugated graphitic structure of graphene, thus, high electrical conductivity can theoretically be achieved through the reduction of GO and restoration of the conjugated structure.[36] Due to the high defect density introduced by oxygen functionalization (38.70 at% O), the resistivity of ARGO approaches infinity and exceeds the full-scale value of the four-point probe unit. While ARGO is deemed an insulator[36, 162], resistivity values obtained for the rGO samples indicate a range in electron transfer capability. The corresponding conductivity of the TGO400, TGO600, TGO900, and CGO samples are 0.47, 2.59, 13.77 and 8.54 S m^{-1}, respectively.

This trend in conductivity agrees with the XPS and Raman results; an increase in rGO conductivity is represented by XPS data as a greater % sp^2 carbon and by Raman as lower defect density and larger sp^2 crystallite size. This agreement in measured conductivity by four-point probe, XPS and Raman is similarly reported by others[36, 48, 141], and is rationalized by the increase in sp^2 carbon (XPS) and decrease in the defect density (Raman) representing the recovery of π conjugated structure. Further, the growth in the crystallite size (increasing I_D/I_G ratio in region 2) indicates a reduction of grain boundaries (the interface between two single crystallites, or grains, in a polycrystalline material), which have been shown to degrade the electrical property of graphene.[163, 164]

The relative conductivity values of TGO600, TGO900 and CGO merit further discussion. CGO has a higher conductivity than TGO600 despite having a comparable % sp^2 carbon (Table 2.1) and I_D/I_G ratio (Figure 2.8). This is attributed to the lower disorder of the CGO structure (reflected by lower Γ_D and Γ_G values, Figure 2.8), a benefit realized through the chemical reduction method. Specifically, thermal annealing induces expansion of the graphene lattice through generation and release of CO or CO_2 gases, which introduces structural damage (e.g., holes) in the graphene plane.[35, 36, 81] These lattice defects inevitably influence the electronic properties by interrupting electron transport and disturbing conductive pathways. In contrast, chemical reduction preserves the graphene structure; the reduction process is based on chemical reactions between functional groups and a reducing agent, which causes minor impacts to the structure of the carbon plane. Given that subtle enhancements in long-range conjugated structures of the sp^2 lattice can impart a significant conductivity enhancement[135], the preservation of the conjugated graphene structure through chemical reduction (compared to thermal) results in significantly higher conductivity of the CGO compared to TGOs annealed below 900 °C.

2.3.5 Biological Activity Changes as a Function of GO/rGO Physicochemical Properties

Proposed mechanisms of adverse biological outcomes of graphene-based materials include membrane stress caused by physical disruption[59, 85, 86], physical interference of essential nutrient fluxes due to diffusion limitation[165], and induced oxidative stress via reactive oxygen species (ROS)-mediated or ROS-independent pathways.[58-60, 87-89] Among these mechanisms, oxidative stress is cited as the dominant mechanism for graphitic nanomaterial toxicity to cells.[59, 87, 88] Graphene, GO and rGO can mediate cellular oxidative stress through, i) the formation of ROS from oxygen adsorption, or ii) by the direct binding with or oxidation of cellular biomolecules.[54, 58, 60, 100] GSH is one such biomolecule that serves to maintain a healthy cellular redox environment and plays an important role in protecting against cellular oxidative stress.[58, 59] The propensity for the prepared GO/rGO samples to oxidize GSH (referred to as oxidative potential) thus, serves as a metric to compare the relative biological activity in the present study.

Figure 2.9 includes the compiled results presenting several important points. First, the magnitude of oxidative potential scales with GO/rGO concentration (Figure 2.9a versus 2.9b). Second, and most importantly, the magnitude of GO/rGO-mediated GSH oxidation shifts for differentially treated samples. (The importance and relative contribution of surface chemistry as well as the consequential physicochemical property modifications that result from thermal and chemical reduction will be discussed in detail below with the respective characterization data.) Third, time-dependent GSH oxidation indicates, i) the loss of GSH scales with exposure time, and ii) suggests that the GO/rGO-GSH interaction is chemical in nature rather than proceeding through physical adsorption because the latter is typically a fast process.[60] As such, the oxidation of GSH by the GO/rGO is the dominant mechanism of GSH loss.

To further evaluate the kinetics of GSH oxidation, a kinetic model was applied to the collected data to estimate a kinetic rate constant, providing insight into the respective sample oxidative potential. In these calculations, it is assumed that the adsorption of reactant (GSH) and desorption of product (e.g., GSSG) from the GO/rGO surface is fast. The GO/rGO-GSH interaction is expressed with the following first-order rate law[60, 166]:

$$-\left(\frac{d[GSH]}{dt}\right) = k[GSH][GO] \rightarrow \ln[GSH] = -k[GO]t + C \qquad (2\text{-}7)$$

where k is the rate constant (mL mg^{-1} h^{-1}), [GSH] is the concentration of GSH remaining in solution, [GO] is the concentration of the GO/rGO sample (0.050 mg mL^{-1}), C is a constant of this integration equation and represents the natural log of the initial concentration of GSH. By plotting ln[GSH] versus time (Figure 2.10), the rate constants (k) are determined from the slope of the resulting linear curve fits to be 3.39, 0.35, 0.56, 1.84, 2.57 and 4.72 mL mg^{-1} h^{-1} for ARGO, TGO200, TGO400, TGO600, TGO900, and CGO, respectively. Finally, there is a good fit of the data with the assumed first-order kinetic model ($R^2 > 0.98$).

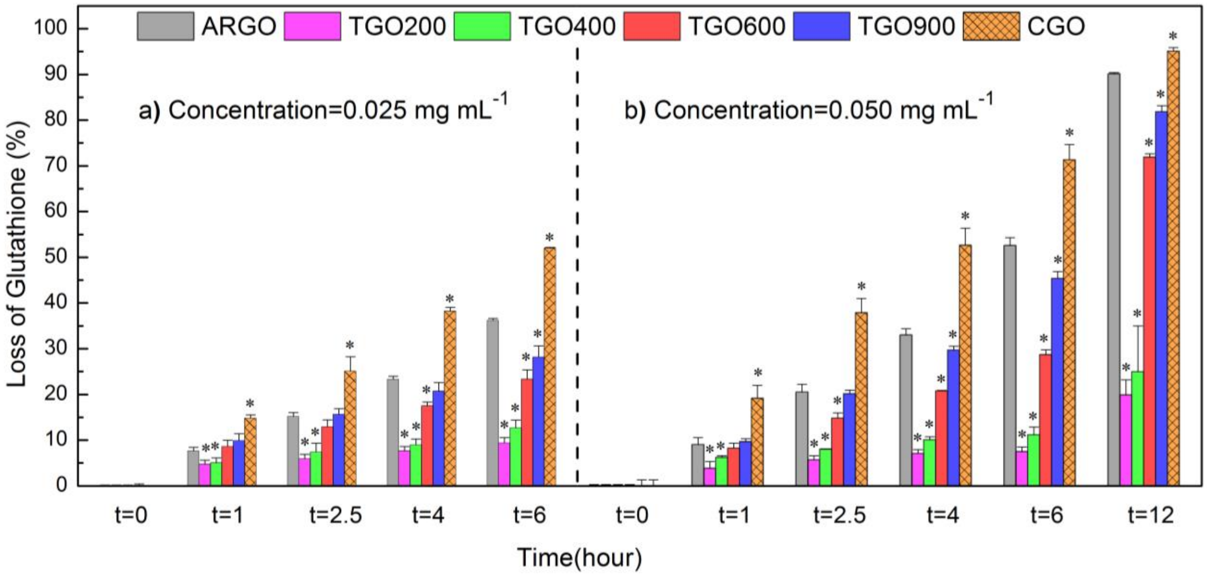

Figure 2.9 Time-dependent GSH oxidation mediated by the prepared GO/rGO samples. Two mass loadings of GO were evaluated, a) 0.025 mg mL^{-1} and b) 0.050 mg mL^{-1}, to demonstrate mass-dependent GSH oxidation. In addition, extended time points in b) were included to i) confirm eventual 100% GSH oxidation and ii) inform subsequent kinetic analysis. Samples were run in triplicate and the error bars represent the sample standard deviation of repeated experiments. Asterisk (∗) denotes the statistically significant differences in means compared to the ARGO by two-sample t test (95% CI, $P < 0.05$).

Combined, the results suggest that GO/rGO-mediated loss of GSH is both time and concentration dependent, and that within a given concentration, the differentially treated GO samples have different propensities for GSH oxidation, represented by their estimated rate constants, CGO > ARGO > TGO900 > TGO600 > TGO400 > TGO200. Finally, the extended time point (12 h, Figure 2.9) demonstrates that 100% loss of GSH can be achieved given sufficient interaction time. In the 0.050 mg mL^{-1} system, 90% and 95% loss of GSH are achieved after 12 h exposure for ARGO and CGO, respectively.

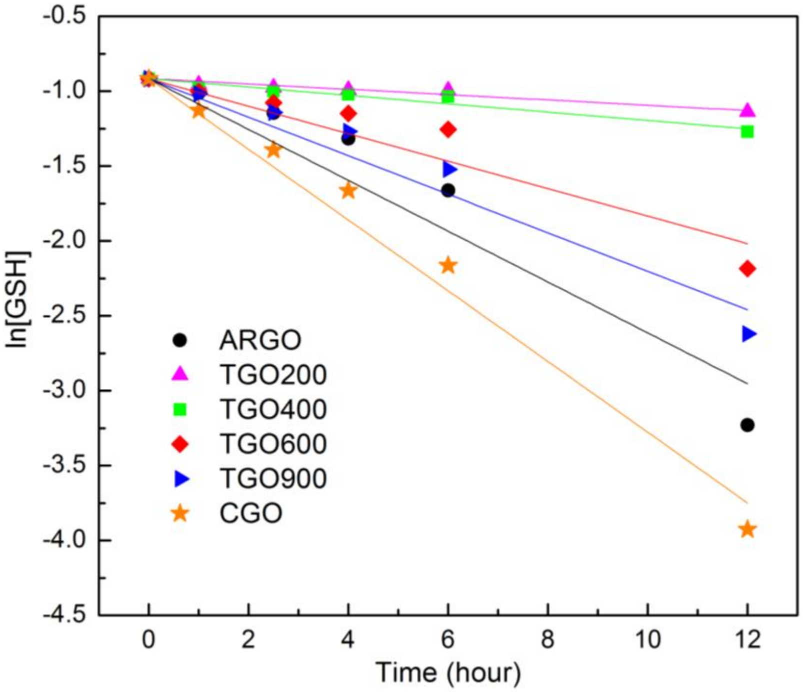

ARGO: $y = -0.1697x - 0.9163,\ R^2 = 0.9820$

TGO200: $y = -0.0177x - 0.9163,\ R^2 = 0.9997$

TGO400: $y = -0.0279x - 0.9163,\ R^2 = 0.9994$

TGO600: $y = -0.0918x - 0.9163,\ R^2 = 0.9892$

TGO900: $y = -0.1286x - 0.9163,\ R^2 = 0.9923$

CGO: $y = -0.2361x - 0.9163,\ R^2 = 0.9950$

Figure 2.10 Plots of ln[GSH] versus time by applying the first-order kinetic model to the GSH oxidation results for ARGO, TGOs, and CGO. The slope of each fitted line was used to determine the rate constant (*k*).

Among the six samples, noteworthy differences in biological activity are observed. The following trends are described in turn. Primary physicochemical properties, including aggregate size, presence of defects, electrical conductivity, and surface chemistry, have been proposed as contributing factors that influence the oxidative capacity of CNMs.[21, 22, 58-60, 100] No single property can explain the observed trends attained in this research, rather the relative contribution of each is discussed in the context of each noteworthy trend.

Oxidative potential of ARGO. ARGO exhibits a higher capacity to oxidize GSH than the thermally reduced samples. A primary difference between ARGO and TGO samples is the amount of surface oxygen and thus, greater defect density of ARGO. The high defect density on the highly-oxidized carbon surface can facilitate adsorption of oxygen, providing the opportunity to generate ROS (e.g., peroxide, superoxide) and promote GSH oxidation.[60, 100] In addition, surface oxygen is known to influence the dispersive properties of GO/rGO[162], and aggregation has been shown to affect the extent of GO/rGO-induced oxidative stress.[58, 59] The dispersed aggregate size was estimated from the peak location of dynamic light scattering (DLS) data in which samples were prepared in the same manner as for the GSH assay. The compiled data (Figure 2.11) indicates that all samples are composed of heterogeneously dispersed aggregates (i.e., multiple peaks and/or broad peaks). Relative peak locations indicate that ARGO has the smallest overall dispersed aggregates (two peaks, both below 1 µm). The highly oxidized surface (C/O ratio = 1.58 ± 0.04) introduces hydrophilic properties unique to ARGO, enabling good dispersion and stability in aqueous media. Peak shifts towards larger aggregates are observed for the TGO samples corresponding with the reduction of surface oxygen. This trend is also reflected in the AFM image analysis (Figure 2.2). The enhanced dispersion of ARGO facilitates interaction with target molecules (e.g., greater available active surface area), giving rise to the enhanced oxidative potential towards GSH. In addition, surface charge is likely to change as a function of surface chemistry and thus, is considered as a possible variable in the associated activity. A negative zeta potential is standard for GO and is attributed to the dissociation of electronegative functional groups.[126, 145] In our current study, the pH is adjusted to 8.6 using bicarbonate buffer. As such, the deprotonation of the carboxylic acid group ($pK_a < 4.2$) is primarily responsible for the negative surface charge compared to the more basic groups, such as phenolic groups (pK_a ~10).[145] No obvious differences in the surface charge were observed among all GO/rGO samples (Figure 2.12). Finally, the high concentration of epoxide groups is a characteristic of GO (as noted in the XPS discussion) and the high steric strain of epoxides introduces reactive surface sites, further enhancing the oxidative potential of ARGO. The thiol group of GSH may serve as the nucleophile attacking the electrophilic carbon atom of the epoxide group facilitating a ring-opening reaction.[167] This process also contributes to the loss (or oxidation) of GSH. Given the thermal lability of epoxides, the relative concentration on the surface of GO is significantly reduced upon thermal annealing. Therefore, this additional mechanism of GSH oxidation is only present for the ARGO sample.

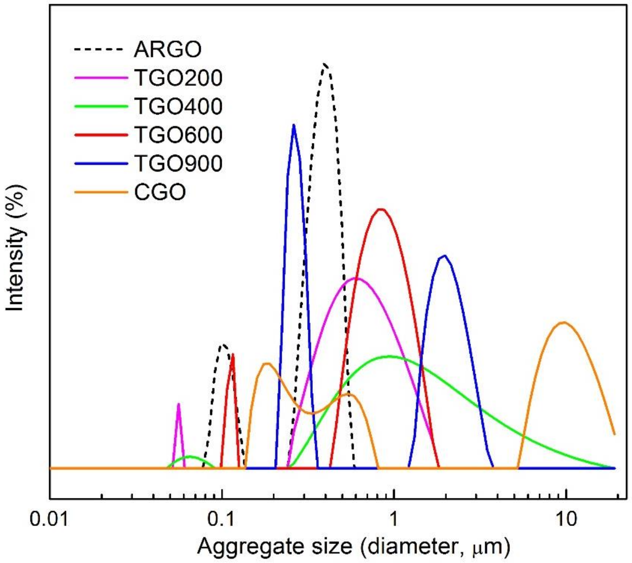

Figure 2.11 Aggregate size distribution of ARGO, TGOs and CGO as determined by DLS in the GSH-assay scenario. Note that TGOs and CGO might precipitate and settle down to the bottom of cuvettes during the measurement period (~5 min), the contribution to the intensity of the scattered light might not come from all the particles being measured. Consequently, the DLS results for these materials may be underestimated.

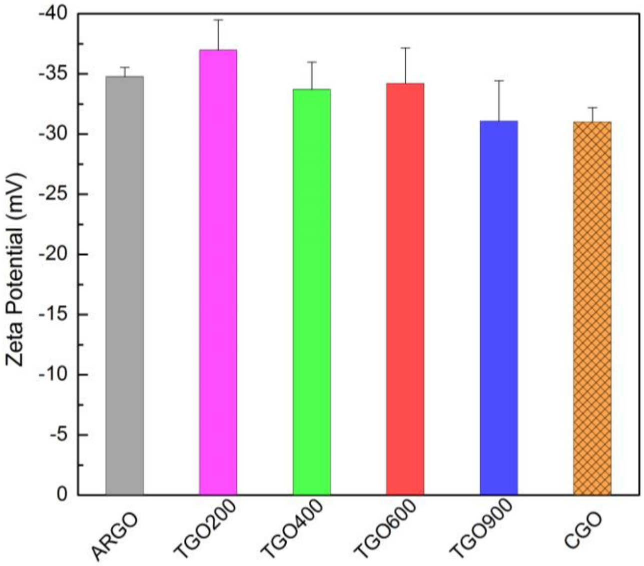

Figure 2.12 Zeta potentials of ARGO, TGOs and CGO measured by ELS in the GSH-assay scenario.

Oxidative potential of rGO samples correlates with conductivity and the presence of carbonyl moieties. The loss of GSH systematically increases with maximum annealing temperature from 200 – 900 °C and is significantly greater for the CGO sample. The factors identified to contribute to the enhancement of ARGO oxidative potential are weakly correlated, at best, with the observed trend of rGO samples (i.e., the defect density decreases, the aggregate size becomes larger and the quantity of epoxide groups decreases upon thermal and chemical reduction). Therefore, for the observed trend is GSH oxidation must result from other rGO properties. As previously discussed, the conductivity of the rGO samples increases with systematic reduction in surface oxygen groups. High conductivity of rGO will accelerate the electron transfer necessary to mediate the oxidation reaction of GSH. However, the TGO900 has the highest measured conductivity, yet CGO has the highest oxidative potential. This suggests that another factor is involved in the observed biological activity. The relative presence of carbonyl moieties on the surface of CNMs has been shown to play an important role in facilitating the oxidation of GSH.[21, 22] The presence of C=O groups differs for these samples with a greater relative presence in the CGO sample (3.21% in TGO900 and 5.50% in CGO, Table 2.1), suggesting that both conductivity and carbonyl moieties play an important role in the biological activity of rGO samples.

Combined, the results suggest that GSH oxidation mediated by GO/rGO samples is not controlled by a sole factor, but instead, is governed by the synergistic effects of consequential properties, including dispersed aggregate size, defect density, electrical conductivity, and the relative presence of carbonyl moiety.

2.3.6 Electrochemical Activity of the Prepared GO/rGO Samples

The realization that CNMs can promote the oxygen reduction reaction (ORR) has inspired their use in energy conversion and storage such as fuel cells and metal-air batteries.[107, 168] Electrochemical performance (i.e., facilitating the rate of electron transfer) of a material is commonly measured via the ORR and represents the propensity of a material to promote or catalyze the reduction of oxygen. Thus, ORR was used here to examine and compare the electrochemical activity of the prepared GO/rGO material suite.

Previous research on O-MWCNTs demonstrates a significant correlation between biological and electrochemical activities.[21, 22] In that work, the enhanced activity was attributed to the ability of differentially treated O-MWCNTs to facilitate the exchange of electrons necessary for both GSH oxidation and ORR. Due to this established connection between GSH oxidation and ORR, both activities were studied here to identify if the same conclusions are transferable across CNM classes. The electrochemical activities of ARGO, TGOs, and CGO were investigated by ORR experiments (in the alkaline media) using the RRDE technique. The evaluation of electrochemical performance using RRDE provides insight into the electrocatalytic activity and electron transfer kinetics of the prepared GO/rGO samples.

The polarization curves for all samples are compiled in Figure 2.13 (1600 rpm, oxygen saturated 1 M KOH solution). A summary of the electrochemical activity indicators determined from this data, including the half-wave potential ($E_{1/2}$), the onset potential, the limiting current (J_L) and the electroactive surface area (A), is presented in Table 2.2. $E_{1/2}$, onset potential, and J_L were acquired from polarization curves in Figure 2.13, and A was obtained from CV curves (Figure 2.14). The kinetic limiting current density (J_K), which indicates the intrinsic ORR activity by excluding the mass transport limited component of oxygen adsorption kinetics, was calculated from the corresponding Koutecky-Levich (K-L) plots (Figure 2.15) and is included in Figure 2.16. Enhancement in electrochemical activity is represented by a greater absolute value of the current density and limiting current, a more positive $E_{1/2}$, and a more positive onset potential.

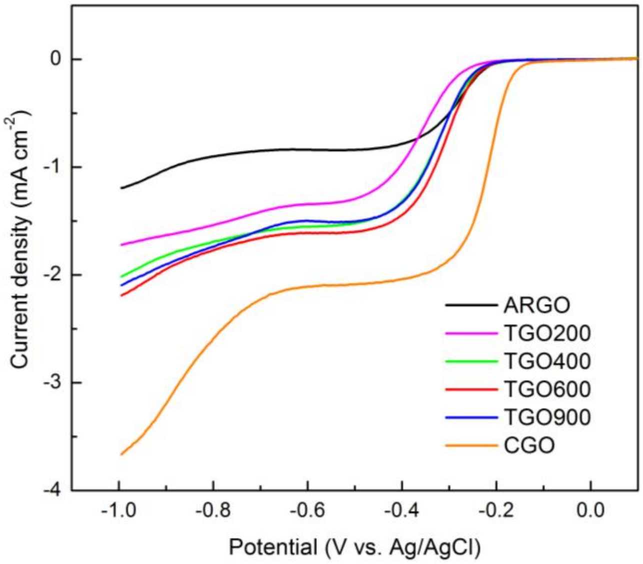

Figure 2.13 ORR polarization curves of ARGO, TGOs, and CGO in O_2-saturated 1 M KOH solution with 1600 rpm rotating speed. All curves display a feature of two regions separated at the potential around -0.5 V, the lower overpotential region is indicative of the reduction of O_2 to HO_2^-, and the higher overpotential region for the reduction of HO_2^- to H_2O. The half-wave potential ($E_{1/2}$), the onset potential, and the limiting current density (J_L) were determined by analyzing the polarization curve in the first region, wherein the onset potential was determined from the intersection of the tangents between the baseline and the current signal.

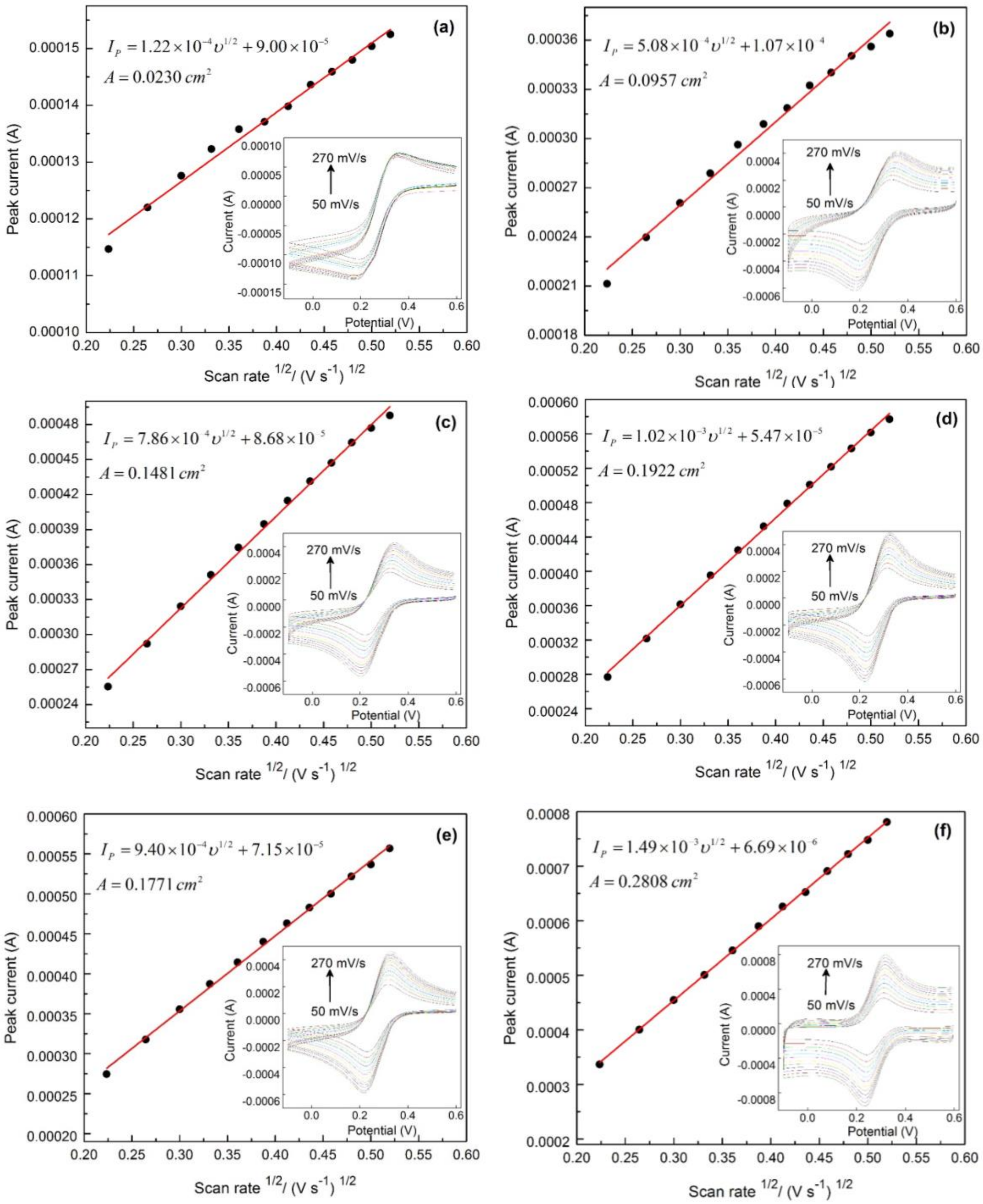

Figure 2.14 Plots of peak current (I_P) versus (scan rate, υ)$^{1/2}$ to estimate electroactive surface area (*A*) of (a) ARGO, (b-e) TGOs, and (f) CGO in 10 mM Fe(CN)$_6^{3-/4-}$/1 M KCl. Insets: CVs at various scan rates from 50 to 270 mV s^{-1}.

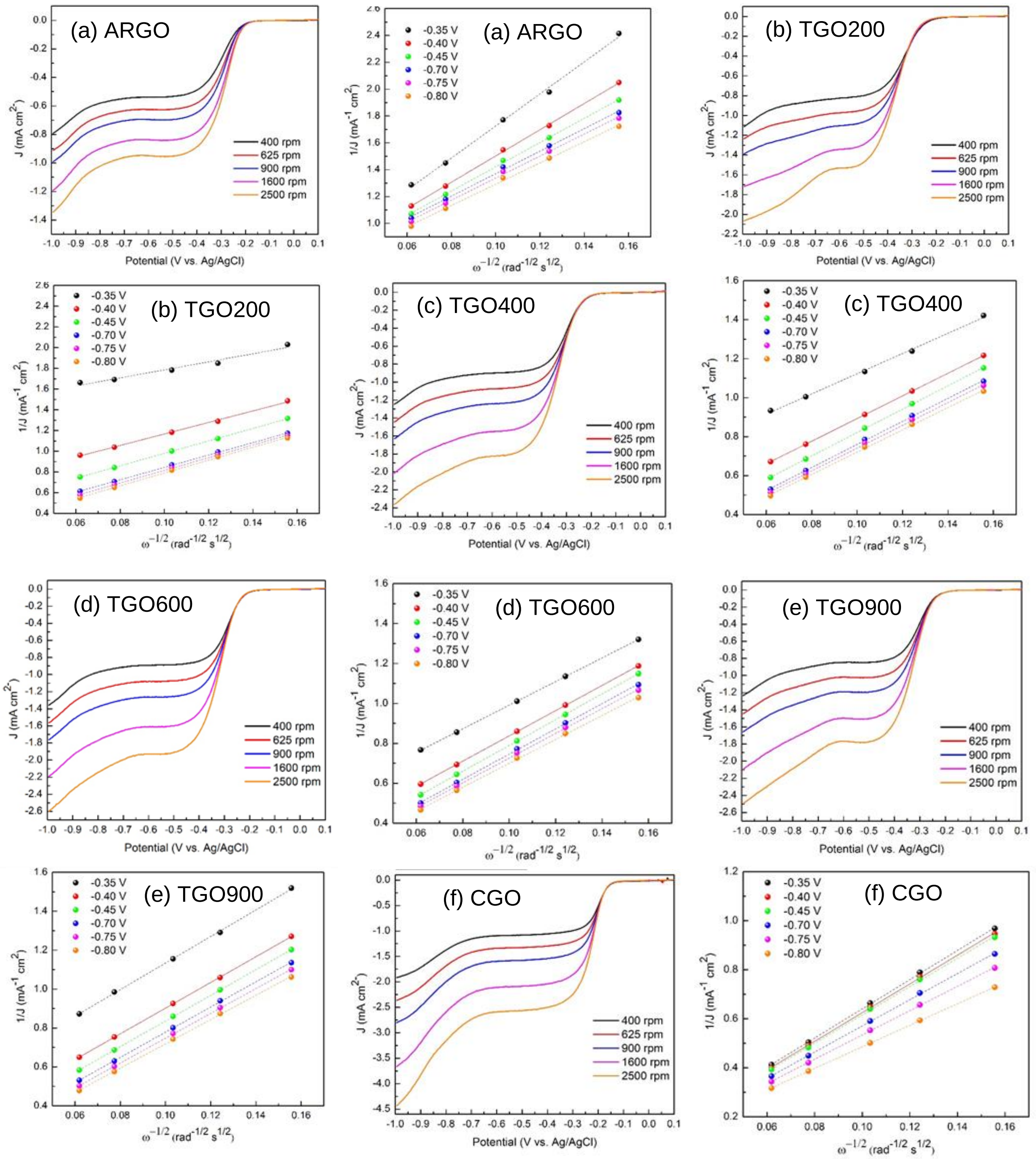

Figure 2.15 Polarization curves and K-L plots of (a) ARGO, (b-d) TGOs and (f) CGO in O$_2$-saturated 1 M KOH electrolyte. Polarization curves were recorded at different rotation speeds of 400, 625, 900, 1600, and 2500 rpm. K-L plots were compiled at electrode potentials of -0.35, -0.40, -0.45, -0.70, -0.75 and -0.8 V, the slopes of the K-L plots were used to calculate the kinetic current density (J_K).

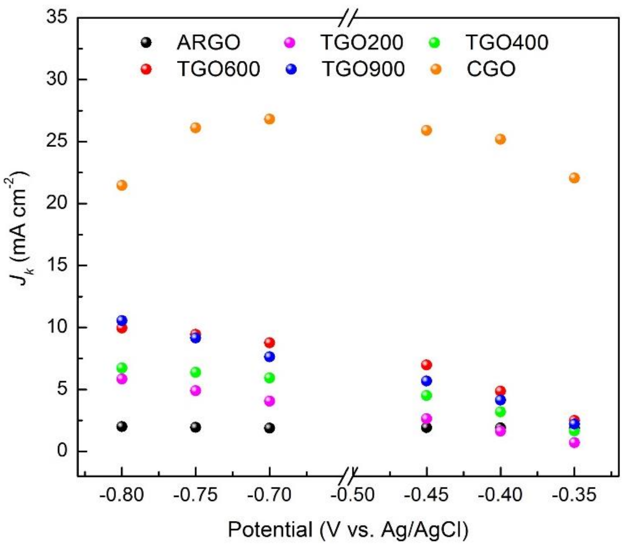

Figure 2.16 Kinetic limiting current density (J_K) of ARGO, TGOs, and CGO calculated from the corresponding K-L plots at different potentials (Figure 2.15). J_K reflects the intrinsic electrocatalytic ability of GO/rGO materials taking no account of the mass transport effect with regard to the oxygen absorption.

Table 2.2 Electrochemical indicators used to evaluate the ORR performance, including the half-wave potential ($E_{1/2}$), the onset potential, the limiting current density (J_L), the kinetic limiting current density (J_K), and the electroactive surface area (A). In general, an enhancement in ORR performance is represented by the higher J_L and J_K, the higher A, more positive $E_{1/2}$ and a more positive onset potential.

Samples	$E_{1/2}$[a] (V)	Onset potential[a] (V)	J_L[a] (mA cm^{-2})	J_K[b] (mA cm^{-2}, -0.45V)	J_K[b] (mA cm^{-2}, -0.75V)	A[c] (cm^2)
ARGO	-0.2862	-0.2143	-0.8408	1.9283	1.9331	0.0230
TGO200	-0.3590	-0.2744	-1.3395	2.6364	4.8996	0.0957
TGO400	-0.3258	-0.2445	-1.5471	4.5188	6.3816	0.1481
TGO600	-0.3127	-0.2344	-1.6101	6.9735	9.4429	0.1922
TGO900	-0.3226	-0.2445	-1.5075	5.6818	9.1491	0.1771
CGO	-0.2201	-0.1695	-2.0885	25.9067	26.1097	0.2808

[a] Data extracted from Figure 2.13. [b] Data extracted from Figure 2.16 (the values of J_K were tabulated at two representative potentials from the low and high potential regions, respectively). [c] Data extracted from Figure 2.14.

Identifying trends in ORR activity of GO and rGO. Similar to the relative biological activity discussed above, ARGO presents unique electrochemical properties. While a more positive $E_{1/2}$ and onset potential indicate more favorable ORR activity for ARGO compared to the TGO samples, the electrocatalytic activity of ARGO is significantly lower, as indicated by the J_L and J_k values, representing a lower density of active sites toward ORR at higher overpotentials. Among the TGO samples, an increase in the electrocatalytic activity is observed with the increase of the annealing temperature until 600 °C, followed by a notable decrease for the TGO900. This trend is reflected in all the indicators ($E_{1/2}$, onset potential, J_L, and J_k). It is interesting to note the improved electrocatalytic activity in the CGO, particularly in terms of the $E_{1/2}$, onset potential and current density. The J_k values of CGO at two representative potentials, -0.45 V and -0.75 V, is significantly greater than those of ARGO and TGOs. Finally, the trend in electroactive surface area, estimated by the Randles–Sevcik equation, agrees well with that of the other discussed electrochemical metrics (see Table 2.2). Specifically, CGO has the greatest electrocatalytic surface area (0.2808 cm^2) and that of TGO600 (0.1922 cm^2) is the greatest among the TGO samples. This indicates that the manipulation of the ARGO under these conditions leads to the increase in the active sites and further enhances the current density.

To gain insight into the ORR pathway, as the 2-electron or direct 4-electron reduction[169], the electron transfer number (n) and concentration of produced H_2O_2 were obtained from RRDE experiments (Figure 2.17). The number of electrons transferred remains greater than 3.2 over the range of potentials for all GO/rGO samples, indicating the contribution of the more efficient 4-electron pathway. The production of H_2O_2 during ORR is commonly monitored in fuel cell research as the presence of H_2O_2 can degrade the catalyst layer and lower the utilization of oxygen.[127] As such, the observed low H_2O_2 yield (< 15%) and high electron transfer number (>

3.6) for the CGO sample suggests it is a more effective catalyst toward ORR. Note that the goal of this study is not to develop the optimal catalysts, rather to utilize the standard metrics and interpretation of the trends in data to probe the role of surface chemistry manipulations on GO/rGO electrochemical activity.

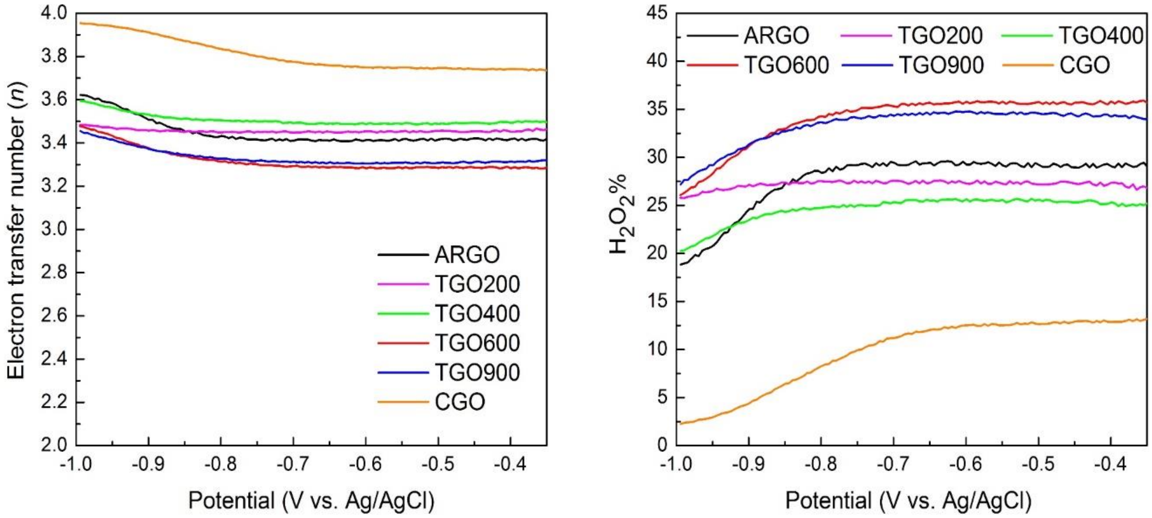

Figure 2.17 Electron transfer number (*n*) and H_2O_2 yield (% H_2O_2) of ARGO, TGOs, and CGO at various potentials from -0.35 to -0.1 V, which were determined based on the disk and ring currents measured from RRDE experiments.

Considering the data from both the GSH oxidation and ORR experiments, different trends were observed for the GO/rGO samples. In the ORR experiments, the electrochemical activity decreases as: CGO > TGO600 > TGO 900 > TGO400 > TGO200 > ARGO. Most notably, ARGO has relatively high capacity to oxidize GSH but has the lowest ORR activity, and a modest decrease of electrochemical activity is observed in TGO900 compared to TGO600. As such, the trends in the biological and electrochemical activities of GO/rGO samples are not synchronous as previously observed for O-MWCNTs[21, 22], indicating that surface chemistry alone cannot elucidate the observed trends in the current study of GO/rGO materials. Several factors have been associated with superior ORR performance of graphene-based materials, including i) good electrical conductivity of materials to transfer electrons between the active catalytic sites[78-80], ii) edge defects (e.g., hole-induced edges, edge-plane-like sites, and dangling bonds) and topological defects (e.g., pentagons and heptagons – five- and seven-carbon rings, respectively) introduced during the reduction processes that serve as electroactive sites for ORR[81, 82], iii) high electroactive surface area indicative of more active sites accessible to ORR[80], and iv) the presence of active functional groups (e.g., quinone groups, C=O) on the carbon surface that are known to enhance the electrocatalysis of oxygen reduction through the production of the semiquinone radicals that accelerate the rate of electron transfer[21, 39, 40]. The relative role of each factor in the observed ORR activity will be discussed further.

The relative importance of conductivity and defects in the electrochemical activity. As postulated by the widely accepted Lerf-Klinowski model, large amounts of hydroxyl and epoxide groups are located mainly within basal planes, with a lower amount of C=O and COOH species on the outer edges of GO.[34, 35] During the reduction process, edge-planes are progressively exposed as C=O and COOH groups are reduced. In addition, defects within the basal plane are introduced in the form of hole-induced edges as well as topological defects like pentagon and heptagons.[81, 82] These defect sites on both the edge and basal planes have demonstrated strong electrocatalytic activity and can be effective active sites for the ORR by means of redistributing the local electron density and enhancing the affinity to the intermediates.[39, 170-173] Likewise, the dangling bonds at the edges are reactive edge defects and can be effective O_2 adsorption sites.[174]

While both conductivity and defects (at the edge and in basal plane) influence the electrochemical activity, it is proposed that conductivity is the dominant factor as evidenced here by the CGO sample. First, the CGO sample has fewer defects within the basal plane due to the inherent difference in the reduction methods, namely the chemical reduction method preserves the graphene basal plane (*vide supra*). Second, CGO has a higher fraction of edge-plane groups (i.e., C=O and COOH) than TGO600 (Table 2.1) − the sample with the next highest electrochemical activity − indicating there are fewer exposed edge-plane defects. Therefore, the prominent contribution of the material conductivity to the ORR activity of CGO is rationalized by the fact that the sample has fewer ORR-active defect sites and significantly enhanced electrocatalytic performance.

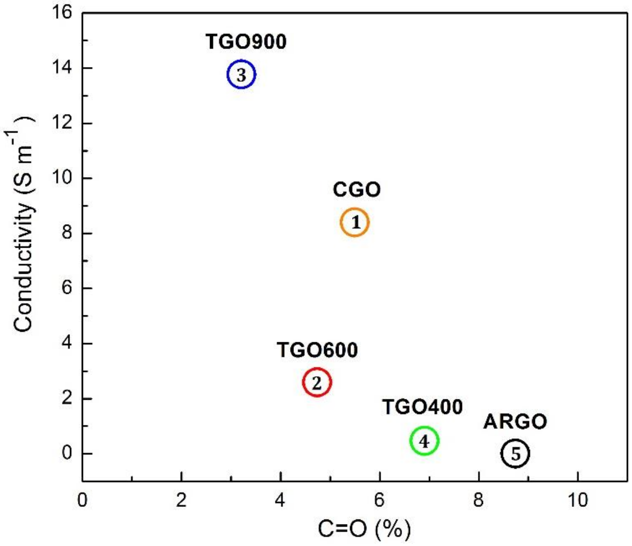

Figure 2.18 The enhancement of electrochemical activity as a function of two critical contributing factors: electrical conductivity and the percentage of carbonyl moiety (% C=O). The conductivity of ARGO is assumed to be zero based on observed insulating behavior during four-point probe measurements. The numeric numbers from 1 through 5 refer to the order of electrochemical activity with 1 as the maximum and 5 as the minimum.

Synergistic contributions of conductivity and the carbonyl moiety to enhanced electrochemical activity. The important role of carbonyl groups in the electrochemical activity of GO/rGO materials is demonstrated through the comparison of TGO600, TGO900 and CGO. The conductivity of TGO900 is significantly higher than TGO600 and CGO, yet the electrochemical performance of TGO900 is inferior to these other two samples. Interestingly, TGO900 has a lower relative proportion of C=O moieties compared with the TGO600 and CGO samples (Table 2.1). Taken together, the data highlights the important contributions of electrical conductivity and carbonyl moieties to enhancement of electrochemical activity. To delineate the influence of electrical conductivity and carbonyl moieties, the conductivity is plotted against the percentage of carbonyl moiety (% C=O). In Figure 2.18, the bottom-left (low conductivity and low % C=O) is the most unfavorable region while the top left (high conductivity and low % C=O) and bottom right (low conductivity and high % C=O) present deficiencies in one of the two contributing factors - carbonyl moieties and conductivity, respectively. The top-right (high conductivity and high % C=O) is theoretically limited, given that the inclusion of surface functionalities inherently disrupts the long-range ballistic transport of graphene materials. The optimal electrochemical activity is achieved with a balance of the conductivity and % C=O, and confirmed empirically by the CGO and TGO600 samples.

2.4 Conclusions

The results presented from the systematically treated and comprehensively characterized GO/rGO material suite reveal that the previously established correlation for O-MWCNTs between, i) electrochemical and biological activities, and ii) the relative presence of carbonyl-containing moieties, is not wholly maintained. Rather, changes in properties as a consequence of modulating surface chemistry play an important role in governing biological and electrochemical activity of GO/rGO materials. Taken together, the results suggest that both activities are driven by synergistic effects from multiple factors informing the following conclusions:

Dispersed aggregate size and defect density (particularly the presence of reactive groups like epoxides) are the primary properties that influence the biological activity of highly oxidized graphene, as demonstrated by the ARGO sample. Yet, when dispersion is eliminated as a factor, such is the case with electrochemical measurements where the material is deposited on an electrode, the highly oxidized surface does not contribute favorably to this functional performance.

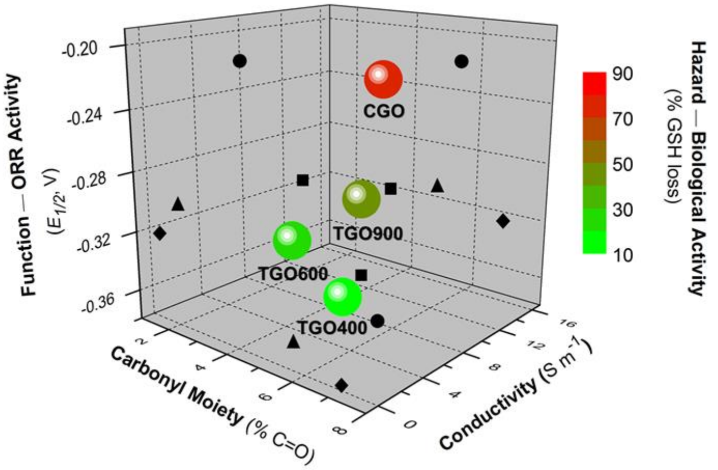

Figure 2.19 Structure-property-function (SPF) and structure-property-hazard (SPH) parametric plot for the rGO sample set, including two synergistic materials properties – conductivity (S m^{-1}) and the presence of carbonyl moieties (% C=O). The function − ORR activity − is represented by the half-wave potential, $E_{1/2}$ (V); and the hazard − biological activity − is represented by the percent loss of GSH (after 6 h exposure to 0.050 mg mL^{-1} rGO samples). Each sphere is an independent rGO sample. The symbols indicate data projections for each sample onto the three planes: rhombuses (◆, TGO400), triangles (▲, TGO600), squares (■, TGO900), and circles (●, CGO).

Restoration of the long-range conjugated graphitic structure, achieved through both thermal and chemical reduction approaches, enhances rGO electrical conductivity contributing to increased oxidation of GSH. A noticeable effect of the carbonyl moiety on the GSH oxidation also emerges as a contributing property as demonstrated by the comparison of TGO900 and CGO samples.

Electrical conductivity and the presence of carbonyl moieties both contribute to enhanced electrochemical activity, which can be optimized through a balance of these two properties, as demonstrated through the TGO600 and CGO samples.

Combined, these findings indicate that surface chemistry is a viable design handle to effectively control biological and electrochemical activity of rGO materials. Yet, rather than a single property modulating function and hazard, it is the balance of two synergistic properties that can be manipulated to control function and hazard. In this way, the addition of a dimension to previously established structure-property-function (SPF) and structure-property-hazard (SPH) plots[5] is proposed in Figure 2.19 for a subset of rGO samples (TGO400, TGO600, TGO900, and CGO). Still, enhancement of the desired function (here, electrochemical activity) is concomitant with enhancement of inherent materials hazard (here, biological activity measured as the oxidation of GSH).

The ultimate goal sought through this and ongoing research endeavors is the ability to tailor function and hazard properties in a controllable and independent manner. Yet, it is possible that electrochemical activity and the propensity to induce biological oxidative stress are inextricably linked given the underlying mechanisms of GSH and ORR require an exchange of electrons (facilitated here by the CNMs). Still, there remains the opportunity to further evaluate the rational design of CNMs and the potential to decouple these activities through surface chemistry manipulations by investigating additional (non-oxygen) functional groups (e.g., other heteroatom doping). In doing so, the contribution of carbonyl-containing groups is eliminated. Heteroatoms, such as nitrogen, sulfur, and boron, have demonstrated favorable influence on the electrochemical activity and conductivity[41, 120, 121, 129, 175-177], providing an avenue to control these two factors. While the biological activity of nitrogen-doped or functionalized CNTs has not been comprehensively studied, there is an indication of lower toxicity.[178] Through the holistic and systematic approach described herein, the underlying mechanisms of CNM activity will be elucidated to inform a guiding framework for rational and sustainable design of CNMs.

3.0 Unveiling the Synergistic Role of Oxygen Functional Groups in the Graphene-Mediated Oxidation of Glutathione

This Chapter has been submitted for publication:

Wang, Y.; Basdogan, Y.; Zhang, T.; Lankone, R. S.; Wallace, A. N.; Fairbrother, H. D.;
Keith, J. A.; Gilbertson, L. M.

This is the first report of an atomic-scale direct oxidation mechanism of the thiol group in glutathione (GSH) by epoxides on graphene oxide (GO) at room temperature. The findings build on the previously established catalytic mechanism of GSH oxidation by graphenic nanocarbon surfaces. Experimental results suggest epoxides are the active sites for the reaction with GO, which we confirm using density functional theory calculations of reaction barriers for possible GO-GSH reaction schemes. We further identify a synergism between adjacent epoxide and hydroxyl groups on the GO surface. This insight is critical for furthering our understanding of GO oxidative stress pathways in cytotoxicity as well as informing rational material design for GO applications that can leverage this reaction (e.g., biosensing) and those in which low cytotoxicity is desired (e.g., applications with high exposure potential). Finally, the findings are translatable to reactions between GO and other important biological and therapeutic thiol-containing compounds.

3.1 Introduction

Graphene-based nanomaterials have attracted great interest in areas of drug delivery, biosensing, tissue engineering,[14, 179-181] and more recently, to enhance agricultural crop production and to enable novel sensing capabilities to reduce stress-related loss.[182-184] Critical atomic scale interactions between the material surface and the surrounding environment drive larger scale bio-interface interactions that enable all of these applications and potentially introduce adverse unintended consequences. Decades of research efforts have been devoted to uncovering mechanistic-level insights into cytotoxic effects[17, 55, 185] and critically, to inform a rational, safe material design paradigm.[3, 5, 6] Yet, uncovering refined mechanisms for fundamental nano-biointerface interactions is fraught with challenges.

The inherent structure of graphene - composed of 2D and hexagonally arranged sp^2-bonded carbon atoms - induces attractive thermal and electrical conductivity, mechanical strength, and high surface area.[186] Graphene oxide (GO) is a graphene derivative containing various oxygen functional groups, including epoxide (C-O-C) and hydroxyl (OH) groups on the basal planes and carbonyl (C=O) and carboxylic acid (COOH) groups at the edges.[34, 89, 187] These hydrophilic oxygen groups enhance GO's aqueous phase dispersion and stability compared to hydrophobic graphene, which facilitates biophysicochemical interactions with the surrounding environment and at the nano-bio interface. The nature of these critical interactions and the resulting impact depend on the particular system of interest, which can range from whole cells[54, 63, 188, 189] to single biomolecules.[185, 190, 191] Further, they reveal insights necessary to advance promising applications that rely on these interactions as well as inform safe material design to preclude unintended consequences.[181]

Studying the impact of GO on whole cells informs potential adverse consequences that will result from exposure, but the biological complexity of the system makes mechanistic understanding challenging. To overcome this challenge, we propose the refined study of specific biomolecule interactions using model systems that allow the explicit examination of atomic scale features and their impact on reaction mechanisms.

Computational approaches, such as Kohn-Sham density functional theory (DFT) or Molecular Dynamics (MD) simulations, can be used to provide insight into molecular interactions and validate mechanistic hypotheses.[192] Interfacial systems can be modeled as periodic systems[193] or with molecular clusters.[194] Several DFT studies have explored the importance of oxygen functional groups on the GO surface using periodic calculations. Notably, Boukhvalov et al. used the oxidation of benzyl alcohol to benzaldehyde as a model reaction and identified diol formation from epoxide ring opening.[195] Chen et al. showed that in a sodium hydroxide solution, the Na^+ cation and water molecule assist the epoxide ring opening reaction,[196] and Cen et al. studied oxidation of SO_2 and NO by epoxide groups on GO via the ring opening reaction.[193] These studies demonstrated the importance and unique reactivity of epoxide groups, particularly to the ring opening reaction. There is also evidence that hydroxyl groups, in conjunction with epoxides, decrease the activation barriers[193, 195] by creating hydrogen bonds that stabilize the transition state structures.[197] Even though GO reactions with many different chemical compounds have been studied, GO reactions with biomolecules (i.e., relatively bigger molecules) have been largely unexplored.

This study tests glutathione (GSH), a thiol-rich tripeptide that is critical to healthy function of eukaryotic and mammalian cells.[198-201] GSH serves as the predominant antioxidant enzyme to maintain the redox environment of cells and protect against the cellular oxidative stress by scavenging the free radicals that damage other important cellular components (e.g., DNA, protein).[38, 56-58] GSH will oxidize to form glutathione disulfide (GSSG) and the balance of GSH and GSSG acts as the predictor of cell redox state and the cell capability to defend against oxidative stress.[57, 202] The measured levels of GSH have been connected with several cancers, Parkinson's disease, Alzheimer's, and HIV.[38, 56] Due to the close relevance of GSH to oxidative stress, acellular GSH oxidation is commonly used to probe the level of oxidative stress imparted by graphene-family nanomaterials and further, to evaluate their relative adverse biological impacts.[22, 58-60, 187]

The mechanism(s) underlying the interaction between GO and GSH remain unresolved. Liu et al. proposed an O_2-mediated, two-step catalytic mechanism for GSH oxidation on graphenic nanocarbon surfaces in which (i) O_2 selectively adsorbs at carbon active sites (edge or defect sites) to form the surface oxides, followed by (ii) direct oxidation of GSH by the surface oxides or liberation of reactive oxygen species (ROS) that subsequently oxidize GSH.[60] Yet, the role of surface oxygen groups already on carbon surfaces – as is the case for GO – in GSH oxidation remains unknown. Our previous research demonstrates varying oxidative potential toward GSH depending on the abundance and the specific types of oxygen groups on both carbon nanotubes[21, 22] and GO.[187] GSH has been used as a "green" reducing agent to produce reduced GO or graphene, though the reduction mechanism has not been proposed.[203] The interaction between GO and GSH is known to result in the reduction of surface oxygen groups, which suggests that GO could promote GSH oxidation via both a (i) catalytic mechanism, whereby the carbon surface is restored after the reaction as proposed by Liu, et al.[60], and (ii) direct oxidation in which GO oxidizes GSH resulting in a change in the surface chemistry.

We now interrogate these mechanisms with experiment and computational theory to resolve the influence of highly reactive and abundant epoxide groups on GSH oxidation.

Specifically, we unravel the relative energetics of elementary reactions involving the different oxygen surface groups (i.e., C-O-C, C-OH, C=O, and COOH). Since the amount and type of surface oxygen groups can be manipulated in a semi-controlled manner, knowing the role of each functional group in this mechanism informs a rational design paradigm. The active oxygen groups involved in the direct oxidation of GSH were determined by examining GO surface chemistry before and after the reaction with GSH using X-ray photoelectron spectroscopy (XPS). GO samples with different percent oxygen and oxygen compositions (the presence and absence of epoxide groups, specifically) were studied at increasing GSH concentrations to maximize the interactions with GO reactive sites. Refined modeling of chemical reactions requires full explorations of accessible regions of phase space using molecular dynamics simulations,[204] but these can be prohibitively costly to run, especially when used for investigating larger scale systems such as GSH oxidation. As a first step toward identifying essential elementary mechanisms, we used a static DFT calculation scheme with explicit solvent molecules to quantify reaction barriers for different possible GO-GSH reaction schemes in order to identify the preferred reactions between specific oxygen groups and GSH. To our knowledge, this is the first molecular scale study of GO-GSH reaction mechanisms. This work also opens the door for other detailed mechanism analyses of a plethora of other biologically important thiol-containing biomolecules (e.g., cysteine) and drugs (e.g., captopril), as well as other important nano-bio interface mechanisms (e.g., membrane lipid peroxidation, the initial point of nanomaterial-cell contact).

3.2 Materials and Methods

3.2.1 Material Preparation

Single-layered graphene oxide, synthesized by the modified Hummer's method, was purchased from ACS Materials LLC (Medford, MA, USA) and used as-received (labeled as ARGO). One thermally annealed sample was prepared by heating ARGO under helium gas flow at 600°C for 30 min and referred to as TGO600. Centrifugation was adopted to isolate and collect ARGO after exposure to GSH while filtration was used for TGO600. These post-reaction samples were cleaned with sufficient rinsing with deionized water and dried in a vacuum desiccator and labeled as P-ARGO and P-TGO600, respectively. The post-reaction sample without GSH exposure was used as the control.

3.2.2 Measurement of GSH and Its Oxidation Product, GSSG

Measurement of GSH by Ellman's assay. The depletion of GSH after exposure to GSH was measured in acellular conditions using the Ellman's assay (DTNB, (5,5'-dithiobis (2-nitrobenzoic acid)) as described in our previous studies.[21, 22, 166, 187] The GO suspension was prepared by 1 h bath sonication (VWR Aquasonic 150T) and added to the GSH solution in a 33 mM bicarbonate buffer (pH=8.6) to initiate the reaction, during which the sample vials were covered with aluminum foil to avoid potential photo-induced oxidation and rotated continuously during the experiment at the room temperature. The final concentration of GO was 0.05 mg mL^{-1} and different initial concentrations of GSH (0.33, 3.3, 16.5, and 33.3 mM) were applied. GO was filtered out of the solution using 0.22 μm syringe filter before the measurement. The concentration of free GSH in the filtered sample solution was quantified using the Ellman's reagent that reacts with the thiol group of GSH to produce a yellow product 3-thio-6-nitrobenzoate (TNB) which can be detected with UV-Vis spectroscopy at 412 nm. The percent loss and absolute loss of GSH was calculated in reference to the control (no GO added).

Measurement of GSSG by GSSG/GSH Quantification Kit assay. GSSG/GSH Quantification Kit assay (Dojindo Molecular Technologies, Inc.) was used to determine the amount of formed GSSG, while the total glutathione (GSH+GSSG) and free GSH were measured at the same time. Specifically, the filtered sample solution was incubated with DTNB and glutathione reductase for 10 min at 37 ℃, wherein GSSG was converted back to GSH by glutathione reductase. Total glutathione concentration was determined by measuring the absorption at 412 nm using a 96-well microplate reader. GSSG was quantified by masking the GSH thiols with 2-vinylpyridine. Free GSH was then calculated by subtracting GSSG from the total glutathione. The GSH solution without GO is used as the control.

The GSH oxidation was conducted at ambient and low dissolved oxygen (DO) conditions, respectively. The ambient O_2 condition refers to the situation that DO is at a normal level (i.e., 8.4 mg L^{-1}) while the low O_2 condition was achieved by purging the solution with nitrogen gas for 20 min before initiating the reaction, resulting in a DO level of 0.25 mg L^{-1}. All the experiments were performed in triplicate.

3.2.3 Characterization of Materials Before and After Reaction With GSH

XPS were used to determine the elemental composition of samples and evaluate the changes in the surface oxygen groups. The spectra were collected using a PHI 5600 instrument with a Mg Kα (1253.6 eV) flood source. Powdered samples were dried in a desiccator prior to analysis and then secured to double sided copper adhesive tape on an XPS sample stub. After preparation, samples were introduced into an ultra-high vacuum environment. Surveys were collected to identify the elements and ensure there were no impurities in the samples. Quantitative analysis was performed on high resolution multiplex spectra for the existing elements including carbon (C1s), nitrogen (N1s), sodium (Na1s), oxygen (O1s) and sulfur (S2p) regions at a pass energy of 29.35 eV, step size of 0.125 eV, with 20 sweeps per region. XPS spectra were quantitatively analyzed using CasaXPS.

Attenuated total reflectance-infrared spectroscopy (ATR-FTIR) was employed as a complementary technique to XPS to confirm the changes in the surface oxygen groups. The data were collected using a Nicolet iS5 with a diamond window. Prior to analysis, samples were dried in a desiccator for at least 24 hours. Samples were analyzed from 4000 cm^{-1} to 400 cm^{-1} at a resolution of 0.482 cm^{-1}, with 16 scans per sample. The background of the instrument was ambient atmosphere for all samples analyzed.

3.2.4 Computational Methodology

All Kohn-Sham density functional theory (KS-DFT) calculations were performed using the ORCA program.[205] To study the graphene oxide morphologies, model clusters of graphene with different sizes and different oxygen functional groups were generated. Edges of the cluster model were terminated by hydrogen atoms so to have a stable GO morphology with a singlet spin state. The reaction mechanisms were modeled by involving one and two GSH molecules. Figure 6 shows illustrations of reactant and product states using our cluster model. Full geometry optimizations were performed using BP86[206, 207]-D3BJ[208]/def2-SVP[209] level of theory. Free energy contributions were calculated using the ideal gas, rigid rotor, and harmonic oscillator approximations at the same level of theory as the geometry optimizations. ωB97x-D3[210]/def2-TZVP single point energy calculations were then performed on the fully optimized geometries to study the significance of high level of theory calculations. Solvation effects were also modeled by performing single point energy calculations using the Conductor-like Polarizable Continuum Model (CPCM)[211] solvation model as implemented in ORCA. Finally, single-ended Growing String Method (GSM) calculations were used to model reaction pathways.[212-214] GSM calculations were found to not converge for some pathways, but even in these cases, GSM calculations found a reasonable starting guess that could be optimized to a valid transition state structure having only one imaginary frequency. All transition state structures reported in this paper were confirmed to have one imaginary frequency, all the remaining structures (reactants, intermediate states, and products) have zero imaginary frequencies.

3.3 Results and Discussion

3.3.1 GSH Oxidation Mediated by GO Proceeds via Parallel Catalytic and Direct Oxidation Routes

GSH oxidation to GSSG (Figure 3.1) is a critical biochemical reaction involved in reducing an oxidative species that would otherwise induce cellular oxidative stress.[57] This reaction was previously proposed to occur via a catalytic mechanism involving dissolved oxygen (DO),[60] which we confirm (Figure 3.2) for our system (as-received GO, (ARGO), synthesized by the modified Hummer's method) under ambient DO conditions (~ 8.4 mg L^{-1}). The oxidative potential of ARGO toward GSH after five successive cycles is fairly repeatable, exhibiting a typical catalytic behavior. These experiments also identified near complete GSH removal at an incubation time to 12 h under ambient DO conditions.

To investigate the potential direct reaction between GSH and surface oxygen groups of GO, a low DO condition (~ 0.25 mg L^{-1}) was used (see details in the methods section). GSH (0.33 mM) exposed to 0.05 mg mL^{-1} of ARGO under ambient DO conditions for 6 h produced 0.09 mM of GSSG (Figure 3.3a) corresponding to a 54% loss of GSH (Figure 3.3b). When this experiment was repeated under low DO conditions, the percent loss of GSH decreased to 20 % (Figure 3.3b), which suggests that the oxidation of GSH by GO is predominantly driven by the DO-mediated catalytic mechanism. While we anticipate that the catalytic mechanism likely persists under low DO conditions to a significantly reduced degree, the 20 % loss of GSH suggests another potential direct oxidation mechanism may be at play.

The lack of significant difference (two-sample *t* test, $P > 0.05$) in total glutathione (GSH + GSSG) between the ARGO and the control sample (no ARGO added) indicates that GSSG is the dominant oxidation product (Figure 3.3a). GSH can be oxidized to minor higher oxidation byproducts, such as sulfinic (R-SO(OH)), and sulfonic ($R-S(=O)_2-OH$) acids.[60, 215] However, unlike GSSG, these higher oxidation byproducts cannot be reduced to GSH through the addition of glutathione reductase.[216, 217] If these higher oxidation byproducts formed, the amount of total glutathione (GSH+GSSG) in the reaction mediated by ARGO would be lower than that of the control, which we do not observe in our data (Figure 3.3a).

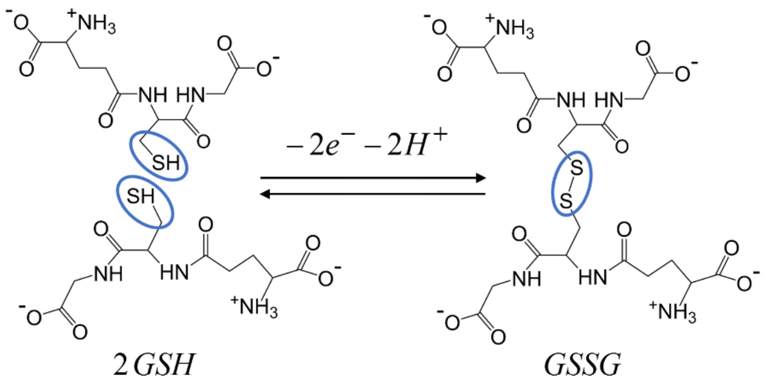

Figure 3.1 Chemical reaction schematic for the oxidation of GSH (glutathione) to GSSG (glutathione disulfide).

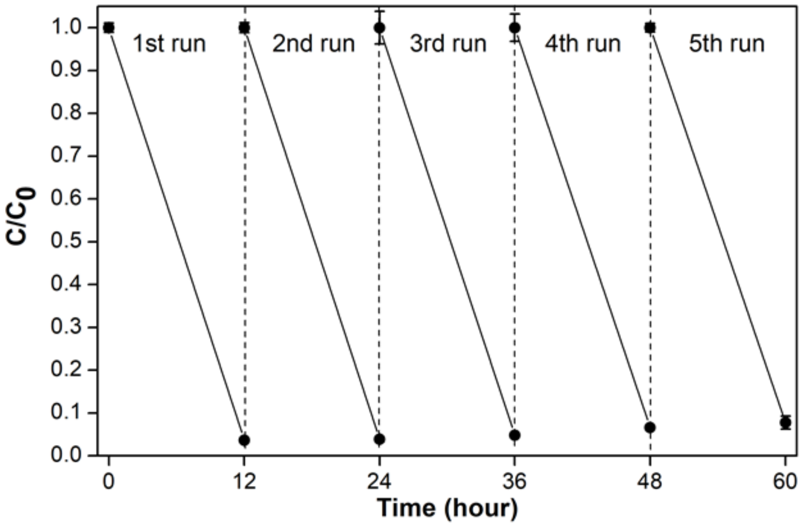

Figure 3.2 GSH oxidation repeated for five cycles under ambient DO conditions. Fresh GSH stock was added to the same reaction vial after each 12-hr cycle. C_0 is the initial concentration of GSH and C is the concentration after "t" h incubation. The depletion of GSH was measured using Ellman's assay. The concentrations of ARGO and initial GSH were 0.05 mg mL^{-1} and 0.33 mM, respectively.

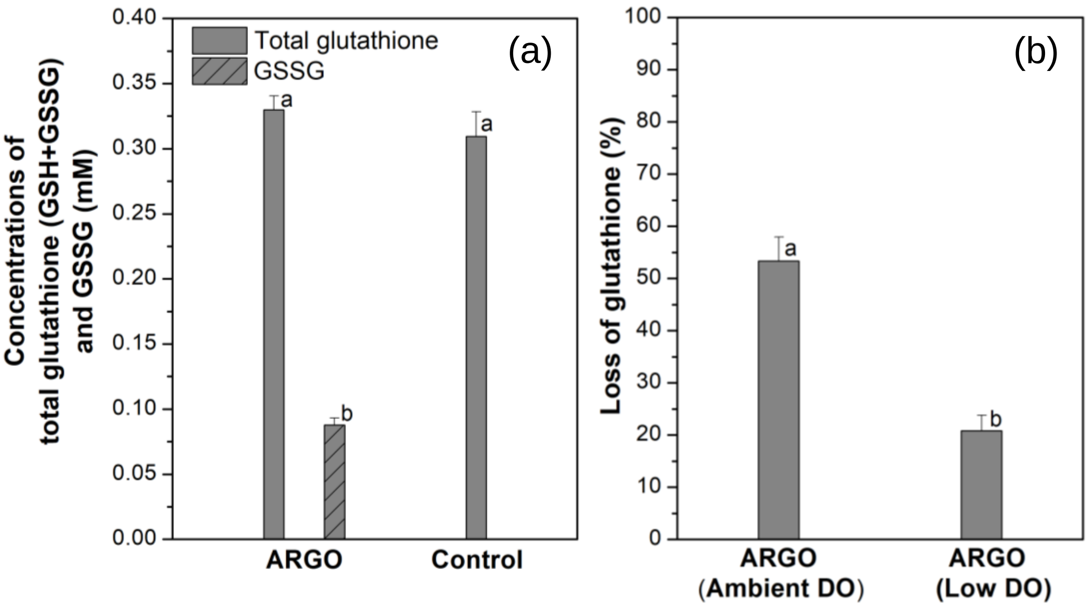

Figure 3.3 (a) Total glutathione (GSH+GSSG) and GSSG measurement using GSSG/GSH Quantification Kit assay after incubation with ARGO for 6 h under ambient DO conditions and (b) the percent loss of GSH under ambient and low DO conditions for a 6 h incubation with ARGO. The ambient and low DO concentrations are ~8.4 and ~0.25 mg mL^{-1}, respectively. The depletion of GSH for (b) was measured using Ellman's assay. The amount of GSSG was quantified by adding glutathione reductase to reduce GSSG to GSH (the unreacted, free GSH was masked prior to the addition of glutathione reductase). The concentrations of ARGO and initial GSH for (a)-(b) were 0.05 mg mL^{-1} and 0.33 mM, respectively. Samples were run in triplicate (n = 3) and the error bars represent the standard deviation of measurements. Means suffixed with different letters (a, b) are significantly different from each other by two-sample *t* test (95% CI, $P < 0.05$).

3.3.2 Quantifying the Changes in the Surface Chemistry of GO Materials Before and After Exposure to GSH Indicates Direct Reaction with Epoxide Groups.

The potential for a direct reaction (non-catalytic) between GSH and oxygen functional groups on the surface of GO was pursued by quantifying changes in GO surface chemistry before and after exposure under low DO conditions. A range of GSH concentrations (3.3 mM to 33.3 mM) and incubation times (0 h to 36 h) were investigated to account for potential concentration and time influences on the direct interaction between oxygen groups on the GO surface and GSH. The higher concentrations and longer exposure times ensured measurable changes of GO in surface chemistry (as discussed below, the material surface changes are much more pronounced when the initial GSH concentration is increased to 33.3 mM).

As expected, increased GSH concentrations and exposure time both result in higher absolute loss of GSH via ARGO-mediated oxidation (Figure 3.4, circles). At the end of each experiment, samples were isolated and extensively washed (referred to as post-ARGO or P-ARGO) and characterized by XPS (results summarized in Figure 3.5). The XPS data of the C1s region indicates that exposure to GSH results in a change in C1s spectral profile that is consistent with the decrease in oxygen of P-ARGO. As well, the oxygen-to-carbon (O:C) ratio before and after exposure is in agreement with the change of spectral profile (i.e., the loss of oxygen) as the O:C ratio decreases from 0.488 for the control P-ARGO sample (without GSH added) to 0.424 for the P-ARGO sample with a 33.3 mM initial concentration of GSH. The diminishment of the C-O component at ~287 eV likely indicates the opening of the epoxide ring and further removal of epoxides due to the reactive nature of epoxides.[218] Importantly, no significant increase of N and S is observed in the P-ARGO sample, suggesting that GSH is not adsorbed on the surface and that GO-GSH conjugates are not appreciably formed in the direct reaction mechanism.

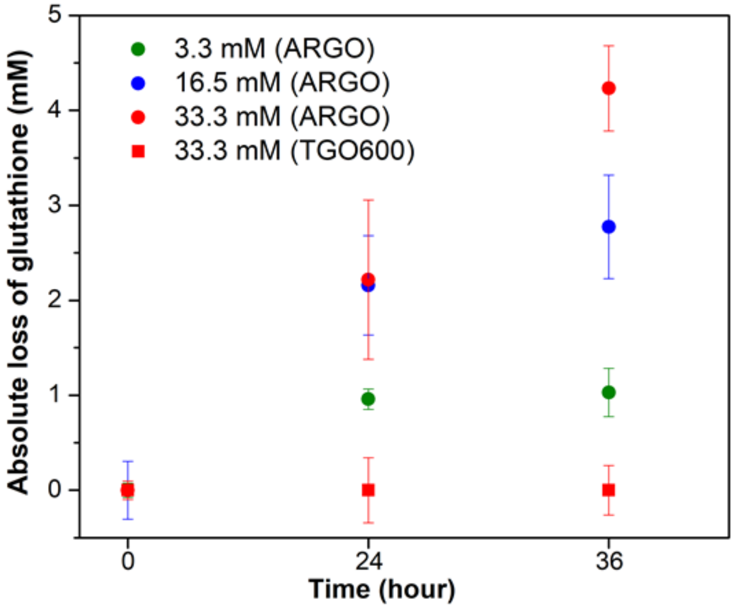

Figure 3.4 The absolute loss of GSH with different initial concentrations of GSH by ARGO and TGO600 under low DO conditions for a total incubation time of 36 h. The GSH concentrations of 3.3, 16.5, and 33.3 mM were investigated. The loss of GSH was measured using Ellman's assay, and the concentration of GO was 0.05 mg mL^{-1}. Samples were run in triplicate (*n*=3) and the error bars denote the standard deviation of measurements.

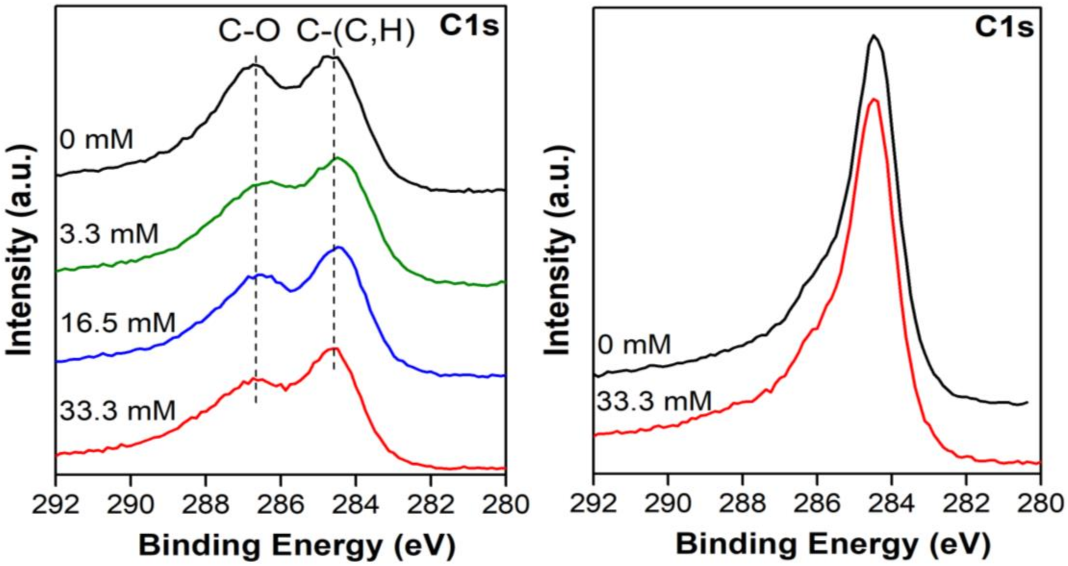

[GSH], mM	C	O	N	S	Na	O: C
P-ARGO						
0	65.6	32	0.3	0	2.1	0.488
3.3	66.5	30.5	1	0.2	1.7	0.459
16.5	66.9	30.2	0.8	0	2.1	0.451
33.3	67.7	28.7	1.3	0.2	2.1	0.424
P-TGO600						
0	85.2	14.1	0	0.1	0.6	0.165
33.3	84.9	13.9	0.6	0.4	0.2	0.164

Figure 3.5 XPS C1s spectra of (a) P-ARGO and (b) P-TGO600 samples exposed to different initial concentrations of GSH under low DO conditions for a total incubation time of 36 h. The samples are exposed to the GSH concentrations of 3.3, 16.5, 33.3 mM while that exposed to 0 mM GSH serves as the control. The table shows changes in atomic percent of the elemental composition and oxygen-to-carbon atom ratio (O:C) on GO samples determined from the XPS data of samples post exposure.

To investigate the potential for epoxide groups to play a role in the oxidation of GSH under low DO conditions, we prepared a reduced GO sample by thermally annealing ARGO up to 600°C (TGO600). Annealing exploits the thermal stabilities of oxygen groups and was used to selectively reduce surface oxygens. Epoxides are the least thermally stable[35] and are expected to be fully reduced at 600°C; carboxylic acid groups will also be removed due to thermal decarboxylation at this temperature.[35, 219, 220] ATR-FTIR confirms that after annealing at 600°C, epoxide groups were absent from the GO surface: the peak at ~1000 cm^{-1} represents epoxide groups (C-O-C) and is absent for the TGO600 sample (Figure 3.6).[143, 187] The XPS C1s spectra also indicates the diminishment of the strong C-O feature at ~287 eV observed in ARGO prior to annealing (Figure 3.5a) for TGO600 (Figure 3.5b). The faint shoulder at ~287 eV for TGO600 suggests the existence of a trace amount of residual oxygen-containing groups, which should be attributed to the high thermal stability of hydroxyl and carbonyl groups.[35, 219, 220]

The GSH oxidation assay was repeated under low DO conditions at the highest initial GSH concentration (33.3 mM) with TGO600 and no significant loss of GSH is observed with increasing exposure time (Figure 3.4, squares). Further, there are no significant changes in the surface chemistry (i.e., the C1s spectrum) for the post-reaction TGO600 sample (referred to as P-TGO600) (Figures 3.5 and 3.6). Thus, we propose that the removal of reactive epoxide groups on the GO surface limits the direct oxidation reaction with GSH and suggest that the contribution of residual oxygen-containing groups on TGO600 (e.g., C=O) to this reaction is insignificant.

The loss of oxygen for ARGO determined from XPS (Figure 3.5) can be used to estimate the contribution of the direct reaction mechanism in the loss of GSH under low DO conditions. For the 3.3 mM GSH concentration condition (Figure 3.4), the percent contribution of the catalytic mechanism is approximately 10 times that of the direct mechanism. While our system is not ideal (i.e., some DO remains) and the relative contribution of the direct mechanism will depend on the system conditions (e.g., initial GSH concentration), this estimate provides a rough baseline comparison.

The combined results corroborate our previous findings[187] that surface oxygen influences the propensity for GO to oxidize GSH under ambient DO conditions (combined catalytic and direct oxidation mechanisms). In the ambient DO system with 0.33 mM GSH, 53% and 20% loss of GSH are observed after 6 h exposure for ARGO (Figure 3.3b) and TGO600 (Figure 3.7), respectively. The primary differences between ARGO and TGO600 include the amount of surface oxygen and the changes of consequential physiochemical properties resulting from thermal reduction of oxygen groups.[187] The capacity to oxidize GSH decreases upon the thermal reduction of ARGO to TGO600 due to the decrease in defect density[187], which is known to drive the catalytic mechanism.[60]

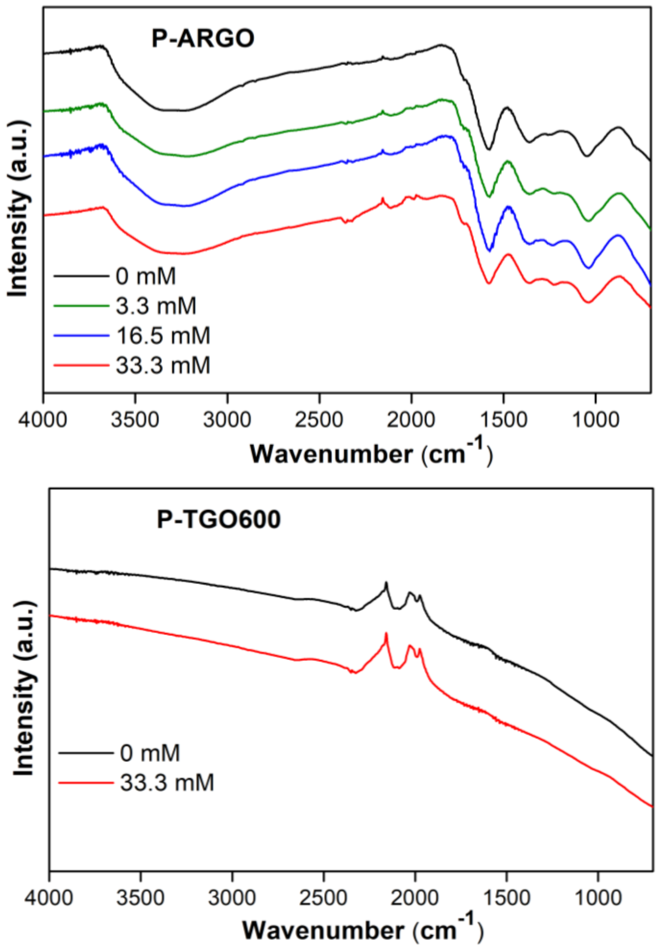

Figure 3.6 ATR-FTIR spectra of P-ARGO and P-TGO600 samples exposed to different initial concentrations of GSH under low DO conditions for a total incubation time of 36 h. The samples are exposed to the GSH concentrations of 3.3, 16.5, 33.3 mM while that exposed to 0 mM GSH serves as the control.

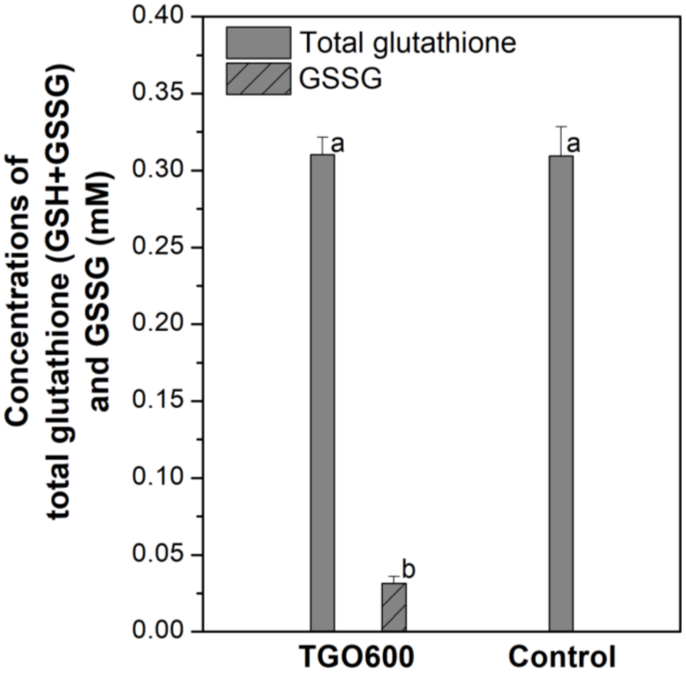

Figure 3.7 Total glutathione (GSH+GSSG) and GSSG measurement using GSSG/GSH Quantification Kit assay after incubation with TGO600 for 6 h under ambient DO conditions. The concentration of DO is ~8.4 mg mL^{-1}. The percent loss of GSH oxidized to GSSG is 20%. The amount of GSSG was quantified by adding glutathione reductase to reduce GSSG to GSH (the unreacted, free GSH was masked prior to the addition of glutathione reductase). The concentrations of TGO600 and initial GSH were 0.05 mg mL^{-1} and 0.33 mM, respectively. Samples were run in triplicate (*n* = 3) and the error bars represent the standard deviation of measurements. Means suffixed with different letters (a, b) are significantly different from each other by two-sample *t* test (95% CI, *P* < 0.05).

3.3.3 DFT Calculations of Reaction Barriers for Different GO-GSH Reaction Schemes Unveil Elementary Reaction Steps.

There are three primary components to the model evaluated in this work: graphene, surface oxygen groups, and GSH. We used a graphene nanoflake model consisting of 52 carbon atoms (forming 18 aromatic rings) with 18 capping hydrogen atoms to ensure the model had a physically relevant spin state of S=0. Preliminary calculations using a smaller cluster (31 carbon atoms forming 10 aromatic rings) were found to be unstable due to inadequate stabilization provided by the smaller cluster. Four primary oxygen groups were considered: epoxide (C-O-C) and hydroxyl (OH) groups on the basal plane, and carbonyl (C=O) and carboxylic acid (COOH) edge groups.[34, 89, 187] The GSH molecule ($C_{10}H_{17}N_3O_6S$) is an eleven C-N chain decorated with two carbonyl, one thiol group (-SH), one amino group (-NH_2), and two carboxylic acid groups at either end. In most calculated pathways we used two full GSH molecules to form the GSSG molecule. All calculations were performed by modeling all reactants and products each as a single cluster to maximize error cancellation within our model. As an example, Figure 3.8 shows the reactant and product states for one of the reaction pathways using a graphene nanoflake. Figure 3.8a shows a hypothetical GO site having two oxygen functional groups (C-O-C and C-OH) along with two unreacted GSH molecules, each forming hydrogen bonds to oxygen species on the surface. Figure 3.8b shows the corresponding product state where oxidation products GSSG and H_2O have formed while one oxygen functional group (C-OH) remains on the surface.

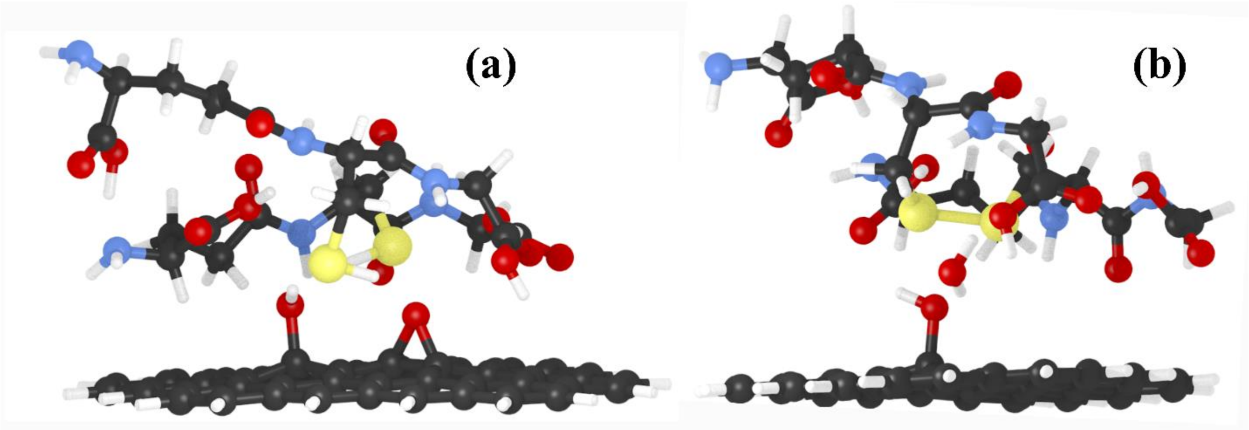

Figure 3.8 A representative molecular cluster model used in computational reaction pathway analyses. a) A reactant state considers the role of two oxygen functional groups (C-O-C and C-OH) and two interacting GSH molecules. b) A resulting product state has one oxygen functional group remaining (C-OH) as well as oxidation products: water and GSSG. Atom coloring: black = carbon; white = hydrogen; red = oxygen; blue = nitrogen; yellow = sulfur.

We used DFT calculations to quantify reaction barriers for several hypothetical reactions involving different oxygen groups on GO with thiol and amino groups of GSH (Table 3.1). The thiol and amino groups were first identified to be the most likely reaction sites (as compared to the C=O groups in the chain or COOH terminal groups) since they have weaker bonds with the carbon chain and thus are more reactive.[221, 222] Subsequently, the thiol group was identified as the preferred site to react with the GO surface since it has a weaker relative bond strength: the S-H bond (~86.8 kcal/mol) compared to the N-H bond (~92.3 kcal/mol).[221, 222] The relative difference in bond strengths also correlates with calculated reaction barriers (Table 3.1). Reactions involving one epoxide, one carbonyl, or one carboxylic acid group with the thiol on GSH were modeled. Reactions with the carbonyl and carboxylic groups resulted in very high barriers (greater than 50 kcal/mol) and thus are considered unfeasible.

Barriers involving a single epoxide group were found to be substantially lower, but results were not consistent with experimental data. On the surface with one epoxide group (Figure 3.9, Reaction 1), the first step found involves the epoxide ring opening with the dehydrogenation of one GSH molecule to form a surface oxygen atom with a reaction energy of 15.5 kcal/mol and a barrier height of 17.2 kcal/mol. Subsequent dehydrogenation of the second GSH molecule forms a water molecule with a reaction energy of -74.1 kcal/mol and a barrier height of 17.7 kcal/mol. Even though the overall reaction energy is calculated to be highly exothermic (-58.6 kcal/mol) due to the formation of water, the calculated barriers are fairly high and would not explain experimental observations of GSH oxidation under ambient temperatures. The primary reason for the high barriers is because water formation in this reaction results in a loss of intermolecular interactions between the surface oxygen species and the GSH molecules relative to the reactant structure. We also observe unphysical buckling of the graphene nanoflake surface in the second transition state indicating a relatively high degree of instability within the computational model.

Table 3.1 The proposed reaction schemes for the interaction between glutathione (GSH) and oxygen groups on the graphene oxide (GO) surface, and the corresponding reaction barrier values calculated using Kohn-Sham Density Functional Theory (DFT) calculations.[a]

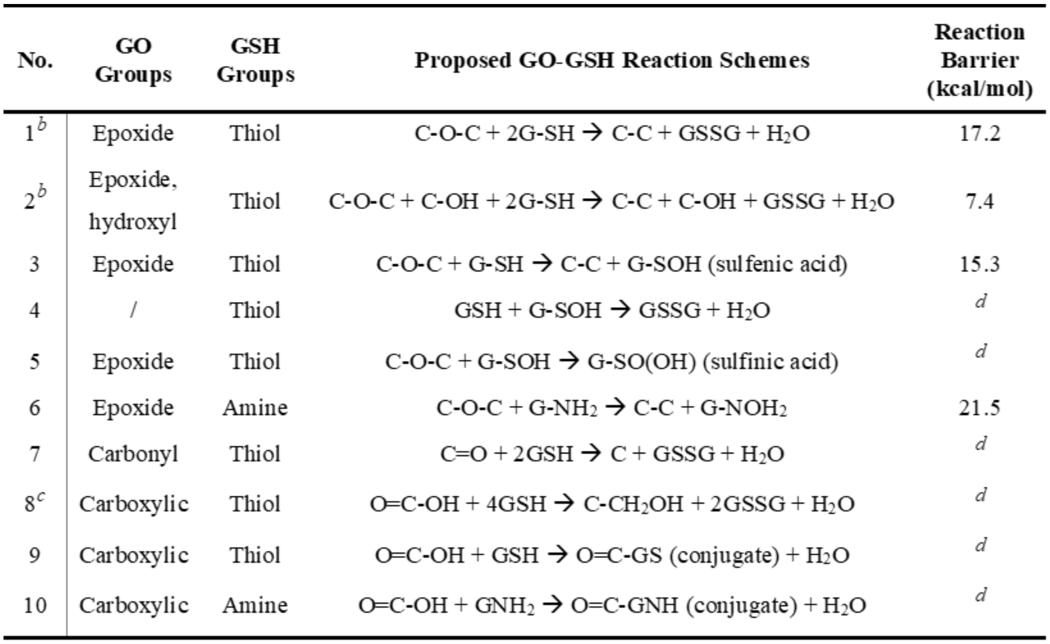

No.	GO Groups	GSH Groups	Proposed GO-GSH Reaction Schemes	Reaction Barrier (kcal/mol)
1[b]	Epoxide	Thiol	C-O-C + 2G-SH → C-C + GSSG + H_2O	17.2
2[b]	Epoxide, hydroxyl	Thiol	C-O-C + C-OH + 2G-SH → C-C + C-OH + GSSG + H_2O	7.4
3	Epoxide	Thiol	C-O-C + G-SH → C-C + G-SOH (sulfenic acid)	15.3
4	/	Thiol	GSH + G-SOH → GSSG + H_2O	[d]
5	Epoxide	Thiol	C-O-C + G-SOH → G-SO(OH) (sulfinic acid)	[d]
6	Epoxide	Amine	C-O-C + G-NH_2 → C-C + G-NOH_2	21.5
7	Carbonyl	Thiol	C=O + 2GSH → C + GSSG + H_2O	[d]
8[c]	Carboxylic	Thiol	O=C-OH + 4GSH → C-CH_2OH + 2GSSG + H_2O	[d]
9	Carboxylic	Thiol	O=C-OH + GSH → O=C-GS (conjugate) + H_2O	[d]
10	Carboxylic	Amine	O=C-OH + GNH_2 → O=C-GNH (conjugate) + H_2O	[d]

[a] Reaction free energies are reported using electronic energies from ωB97x-D3/def2-TZVP calculations on molecular geometries optimized using BP86-D3BJ/def2-SVP.

[b] The reaction mechanisms 1 and 2 are explained in detail in the main text. The first reaction barrier for each multi-step reaction scheme is included in this table.

[c] The first step of this multi-step reaction mechanism was examined, and the reaction barrier calculated for the initial step was higher than 50 kcal/mol.

[d] Calculated barriers for these reactions are higher than 50 kcal/mol, indicating the systems are highly unstable and the reactions will not occur.

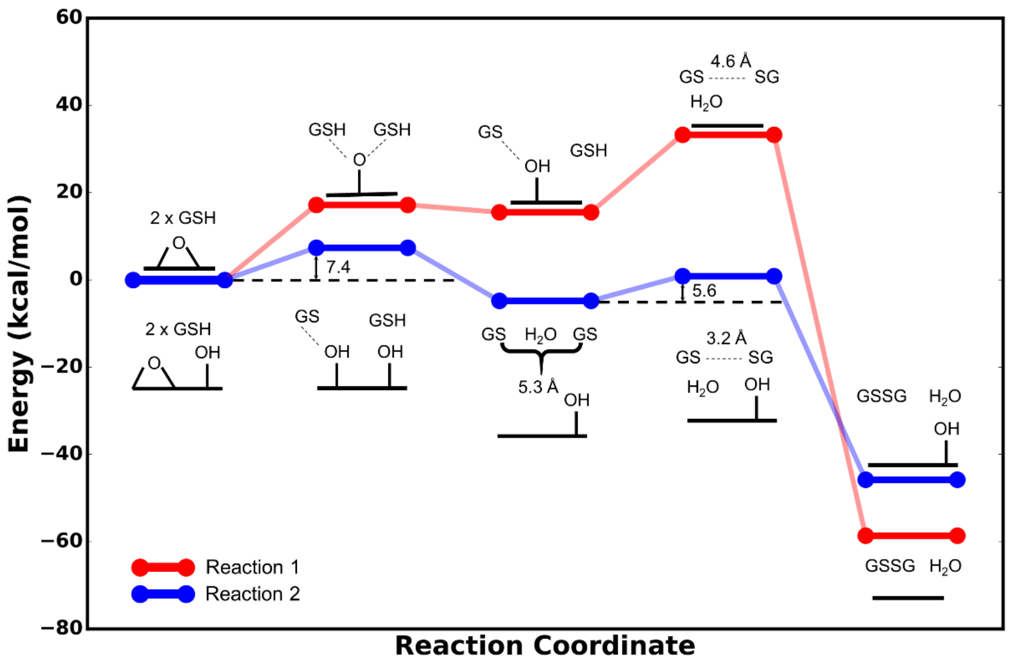

Figure 3.9 Calculated reaction free energies for two different reaction mechanism. Gas phase reaction free energies are reported in ωB97x-D3/def2-TZVP//BP86-D3BJ/def2-SVP level of theory. Reaction 1 is the reaction of GSH with one epoxide group on the graphene cluster. This is a two-step reaction mechanism where the first step involves the ring opening reaction of the epoxide group on the graphene and the dehydrogenation of a GSH molecule with a reaction energy of 15.5 kcal/mol and barrier height of 17.2 kcal/mol. The second step involves the dehydrogenation of the second GSH molecule to form a water molecule which has a reaction energy of -74.1 kcal/mol and has a barrier height of 17.7 kcal/mol. Reaction 2 is also a two-step reaction mechanism of GSH with one epoxide group and one hydroxyl group on the graphene cluster. The first step of Reaction 2 is the ring opening of the epoxide group and the dehydrogenation of both GSH molecules with a reaction energy of -4.8 kcal/mol and a barrier height of 7.4 kcal/mol. The second step is the formation of the S-S bond with a with a reaction energy of -41.0 kcal/mol and a barrier height of 5.6 kcal/mol.

We then considered alternative configurations of oxygen species, namely a situation where an epoxide would be adjacent to a hydroxyl group.[193, 195] In this scenario, the first step again is the epoxide ring opening reaction with the dehydrogenation of a GSH molecule to form a diol group on the surface which immediately reacts with the other GSH molecule to form a metastable complex of dehydrogenated GSH molecules and water which interact with the remaining hydroxyl group (reaction energy = -4.8 kcal/mol; barrier height = 7.4 kcal/mol). The primary reaction coordinate in this system is the distance between the two sulfur atoms on the two different GSH molecules, D_{S-S}, which is 4.6 Å in our reactant state but then increases to 5.3 Å in the product state of the first reaction. This increase in D_{S-S} is due to the formation of a stable intermediate with hydrogen bonding between the two sulfur atoms of GSH and the now formed water molecule. The second step on this pathway is the formation of the S-S bond between dehydrogenated GSH molecules (reaction energy = -41.0 kcal/mol; barrier height = 5.6 kcal/mol), which would also liberate the water molecule. For the second reaction step, D_{S-S} is initially 5.3 Å and then decreases to 2.1 Å upon forming a GSSG molecule.

Our critical finding is that the only energetically feasible GSH oxidation pathway that we could observe does not simply involve just an epoxide species. Instead, GSH oxidation likely occurs at a site that synergistically involves both an epoxide and an adjacent oxygen group needed for additional stabilization (e.g., a hydroxyl group). We observe that hydroxyl groups can form hydrogen bonding networks similar to those observed in previous computational studies of GO as mentioned before.[193, 195] Here, the hydroxyl group facilitates hydrogen bonding that stabilize the transition states structures and thus result in lower reaction barriers. We also report reaction free energies modeled using a continuum treatment for solvation in Figure 3.10. The overall picture is qualitatively the same as what is provided by gas phase calculations, but the barrier heights for the solvated reactions are substantially higher and do not corroborate with our experimental data. While solvation energy contributions may be assumed to be important, recent studies have shown that continuum solvation models are sometimes surprisingly poorly suited for giving insights into multistep reaction mechanisms,[223, 224] and thus we presently have higher confidence in the simpler model that uses gas phase energetics that also results in data consistent with experimental work.

We also evaluated other reaction mechanisms that might be important for GSH-GO system. We modeled reactions involving the oxygen edge groups, and they all resulted with barriers greater than 50 kcal/mol (Table 3.1), suggesting they do not play a significant role in this reaction mechanism. Our calculations found that G-SOH (sulfenic acid) formation has a reasonably low barrier (15.3 kcal/mol), but this reaction is highly exoergic, which makes the formation of GSSG from G-SOH highly unfavorable (+66.9 kcal/mol). Thus, our analysis suggests that G-SOH formation can occur as a side reaction, but it is not a desired intermediate en route to GSSG. We also considered a GSH molecule reacting from the nitrogen site and forming a G-NOH$_2$ molecule, however the barrier calculated for this reaction (21.5 kcal/mol) was higher compared to that for G-SOH formation (15.3 kcal/mol). This is not surprising since S-H bonds are substantially weaker than N-H bonds (*vide supra*), and so it is easier for oxygen to get inserted between an S-H bond rather than a N-H bond. The list of all the reactions we have studied is given in Table 3.1.

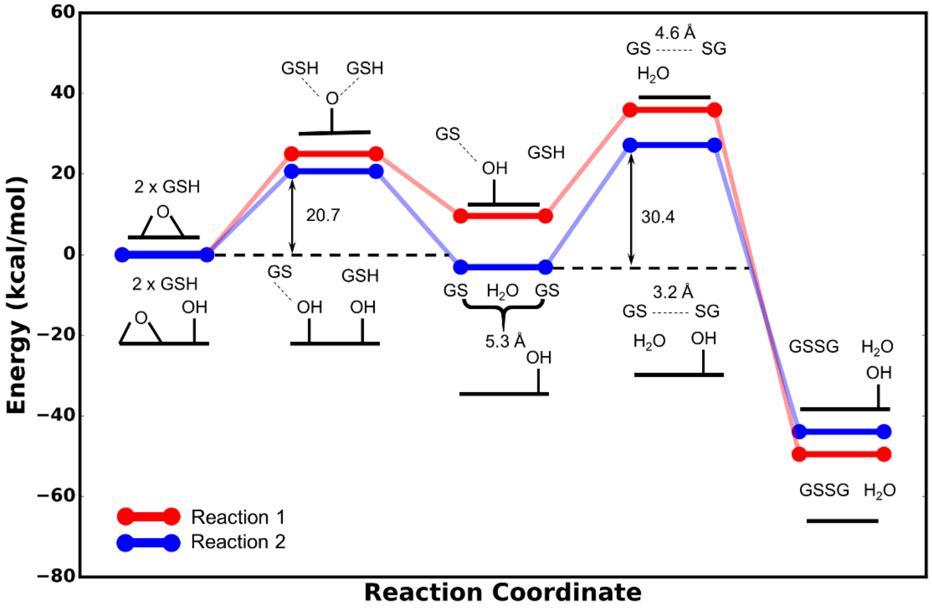

Figure 3.10 Reaction energies from Figure 3.9 calculated using continuum solvation energies using ωB97x-D3/def2-TZVP(CPCM)//BP86-D3BJ(CPCM)/def2-SVP. Reaction 1 involves the reaction of GSH with one epoxide group on the graphene cluster. This is a two-step reaction mechanism where the first step involves the ring opening reaction of the epoxide group on the graphene and the dehydrogenation of a GSH molecule with a reaction energy of 9.6 kcal/mol and barrier height of 25.0 kcal/mol. The second step involves the dehydrogenation of the second GSH molecule to form a water molecule which has a reaction energy of -59.1 kcal/mol and has a barrier height of 26.9 kcal/mol. Reaction 2 is also a two-step reaction mechanism of GSH with one epoxide group and one hydroxyl group on the graphene cluster. The first step of Reaction 2 is the ring opening of the epoxide group and the dehydrogenation of the both GSH molecules with a reaction energy of -3.1 kcal/mol and a barrier height of 20.7 kcal/mol. The second step is the formation of the S-S bond with a reaction energy of -40.8 kcal/mol and a barrier height of 30.4 kcal/mol

3.4 Conclusions

The integration of experimental and cost-effective computational approaches enables a complementary and comprehensive understanding of the interaction between GO and the important cellular antioxidant, GSH. Results from both approaches reveal a direct oxidation mechanism of GSH by GO in addition to the previously reported catalytic oxidation mechanism. Examination of the GO surface chemistry changes before and after exposure to GSH show a decrease in the C-O content for a GO sample with epoxide groups (ARGO) and no notable change in the GO surface for a reduced GO sample without epoxide groups (TGO600). This empirical data suggests the important role of epoxide groups in the direct oxidation of GSH, which we explore further using a computational quantum chemistry approach. DFT calculations of all possible reaction schemes between GSH and oxygen groups on GO demonstrate that epoxide groups are the preferred active sites for GSH oxidation. Furthermore, adjacent hydroxyl groups are modeled and demonstrate facilitation of GSH oxidation by reducing the reaction barrier through transition state stabilization involving intermolecular hydrogen bonding interactions between the hydroxyl groups on the GO and the reacting GSH species.

The combined empirical-computational approach identifies an important direct reaction between the GO surface and a thiol-containing biomolecule. The methodology enables interrogation of this direct mechanism and findings from this study are transferrable beyond GSH to the interactions between oxygen functionalized carbon nanomaterials and thiol-containing molecules. Further, this work provides insights into manipulating surface oxygen groups to rationally design CNMs to meet intended performance needs in an application that may or may not leverage bioactivity. For example, the reactive sites on CNMs (e.g., epoxides on GO) can be tailored to control the toxicity to human health and the environment. On the other hand, the surface chemistry can be manipulated to promote such reactions, such as in the development of sensing probes for monitoring thiol related biological processes. While a low DO environment has allowed us to identify the direct interaction mechanisms between GSH and the GO surface, these conditions are also relevant to anoxic natural and engineered systems. For example, anoxic conditions occur in subsurface natural water and soil systems in which our research findings not only illuminate the potential adverse impacts of unintended release of CNMs to the ecosystem but can also be used to advance the identification of thiol compounds in such environmental samples using CNM-based sensing platforms. In engineered systems (e.g., microbial fuel cells, sensors), there are opportunities to leverage nano-bio interactions to enhance the performance (e.g., electron transfer, selectivity and sensitivity of detection events). For example, in microbial fuel cells CNM-based anode electrodes can be manipulated through changing surface chemistry to ensure biocompatibility to anaerobic microbes while still facilitating the desired extracellular electron transfer.

4.0 Leveraging Electrochemistry to Uncover the Role of Nitrogen in the Biological Reactivity of Nitrogen-Doped Graphene

This Chapter has been published:

Wang, Y.; Aquino de Carvalho, N.; Tan, S.; Gilbertson, L. M. *Environmental Science: Nano* **2019**, 6, 3525

While nitrogen doping greatly broadens graphene applications, relatively little is known about the influence of this heteroatom on the biological activity of graphene. A set of systematically modified nitrogen-doped graphene (NG) materials was synthesized using the hydrothermal method in which the degree of N-doping and N-bonding type is manipulated using two nitrogen precursors (urea and uric acid) and different thermal annealing temperatures. The bioactivity of the NG samples was evaluated using the oxidation of the intracellular antioxidant glutathione (GSH) and bacterial viability (of *Escherichia coli* K12*)*, and oxidative stress was identified as the predominant antibacterial mechanism. Two key energy-relevant electrochemical reactions, oxygen reduction reaction (ORR) and oxygen evolution reaction (OER), were used to characterize the influence of different N-types on the electronic properties of the NG materials. Electron-donating graphitic-N and electron-withdrawing pyridinic-N were identified as effective promoters for ORR and OER, respectively. The similar mechanisms between the GSH oxidation (indicative of oxidative stress) and ORR mechanisms reveal the role of graphitic-N as the active site in oxidative stress related bioactivity, independent of other consequential properties (e.g., defect density, surface area). This work advances a growing rational design paradigm for graphene family materials using chemical composition and further provides valuable insight into the performance-hazard tradeoffs of NG applications in related fields.

4.1 Introduction

The one-atom-thick and high-aspect-ratio graphene gives rise to advantageous electronic, thermal, optical, and mechanical properties that enable diverse applications in energy storage and conversion, electronics, and biotechnology.[11, 12, 14, 15, 49, 225] Research on biological interactions of graphene-based nanomaterials and the ability to manipulate properties to influence interactions at bio-interfaces are critical for not only understanding potential risks that graphene poses to environmental and human health through increased use, but also for enabling their biomedical and bioanalytical development.[19, 21, 22, 187] In addition, resolving the material properties that govern impacts of graphene-based nanomaterials at bio-interfaces is critical to developing rational design guidelines to meet desired functional performance outcomes in these applications while minimizing the potential for unintended consequences.[5]

Chemical doping of graphene with heteroatoms, particularly nitrogen, is an effective approach to tailor electronic properties and chemical reactivity of graphene, which contributed to the emergence of (bio)electronic, (bio)sensor, electrocatalyst, and energy storage and conversion applications.[41-44, 226, 227] However, to date, very little is known about the influence of nitrogen doping on the biological activity of graphene. The similarity in the atomic size of nitrogen and carbon, and the five available valance electrons enable relatively facile replacement of carbon with nitrogen in the graphene lattice by forming strong covalent bonds.[43] Differences in electronegativity and electron density introduce charge redistribution between nitrogen dopants and adjacent carbon atoms. The resulting changes in spin density and charge distribution of these carbon atoms bring about more active sites on the graphene, accelerating electron transfer and improving the (electro)cataltyic activity of graphene.[42, 177, 226, 228, 229] While pure graphene is a zero-bandgap semimetal, nitrogen doping shifts the Fermi level and opens up the bandgap, enabling the transformation of graphene to a *n*- or *p*-type semiconductor depending on the particular nitrogen configurations.[227, 230-232] Nitrogen doping is a facile doping process that effectively modulates the structure and physicochemical properties of graphene while maintaining high electrical conductivity.[233]

Our previous study on reduced graphene oxide (rGO) demonstrates the positive correlation between electrochemical activity and the propensity to induce biological oxidative stress.[187] Decoupling these activities (e.g., by identifying another structural or property feature that correlates independently with biological oxidative stress) would elucidate opportunities to design graphene-family materials with enhanced electrochemical performance while reducing the potential for adverse biological impacts. Previous findings of nitrogen-doped carbon nanomaterials (carbon nanotubes, graphene, carbon dots) suggest the potential opportunity to decouple the governing properties due to suggested biocompatibility.[178, 234-240] On the other hand, in our efforts to probe underlying mechanisms of electrochemical and biological reactions of oxygen functionalized carbon nanomaterials,[21, 22, 187] we identified electron transfer properties common to both activities that are similarly tuned by different surface functional groups. In this work, we investigate the potential for nitrogen doping to (i) decouple function and biological reactivity of graphene, and (ii) establish the foundation for a new paradigm linking inherent electronic and biological activities of carbon nanomaterials.

N-doped graphene (NG) contains four primary nitrogen configurations in the graphene lattice: pyridinic-N, pyrrolic-N, graphitic-N, and N-oxide.[42, 74, 229, 241] The nitrogen bonding configurations, not the total nitrogen content, have been identified as the key factor for the performance of important electrochemical reactions (e.g., oxygen reduction reaction (ORR) and oxygen evolution reaction (OER)), with pyridinic-N or/and graphitic-N configurations commonly considered as active catalytic sites.[42, 66, 73, 75, 226, 242] To further resolve the role of N in the biological activity of NG and the potential to decouple from electrochemical activities, we systematically prepared a set of NG materials with varying degrees of N-doping and different N-types using a hydrothermal method. The degree of nitrogen doping and configurations of nitrogen in doped graphene is tailored by using two different nitrogen precursors (urea and uric acid) and thermal annealing under different temperatures. The bioactivity of the prepared materials is evaluated as the inactivation of a bacterial model organism, *Escherichia coli* (*E. coli*) K12, and the propensity to oxidize the intracellular antioxidant, glutathione (GSH). Two important and well-studied electrochemical reactions, ORR and OER, are used (i) as representative functional performance metrics (relevant to energy-related electrochemical reactions), and (ii) to characterize the inherent electronic behavior of different NG materials as the potential mechanism underlying different biological activities.

4.2 Materials and Methods

4.2.1 Chemicals and Materials

Single layer graphene oxide (GO) powder (~99% purity) prepared using Hummer's method was purchased from ACS Materials LLC (Medford, MA, USA, product no. GNOP20A5), and used as the starting material to synthesize N-doped graphene. Uric acid (≥ 99%), methylene blue, platinum (20% on carbon black), iridium (IV) oxide (IrO_2, 99.99% metals basis), and Nafion perfluorinated resin solution (5 wt% in mixture of lower aliphatic alcohols and water) were obtained from Sigma-Aldrich (St. Louis, MO, USA). Urea (≥ 99%), reduced glutathione (GSH), bicarbonate ($NaHCO_3$), tris(hydroxymethyl) aminomethane (TRIS, 99.85%), hydrochloric acid (HCl, 36.5 – 38%), Ellman's reagent (5,5'-dithio-bis-(2-nitrobenzoic acid), DTNB), dimethyl sulfoxide (DMSO, ≥ 99.9%), potassium hydroxide (KOH, 85.8%), isopropanol (molecular biology grade, ≥ 99.9%), sodium chloride (NaCl, 99.6%), Bacto agar, and Luria-Bertani (LB) Lennox broth (Lot 163854) were obtained from Fisher Scientific (Pittsburgh, PA, USA). Polypyrrole was purchased from Toronto Research Chemicals (Toronto, ON, Canada). Deionized (DI) water was produced by Millipore Synergy UV Water Purification System and used as solvent for all chemicals, unless otherwise specified.

4.2.2 Synthesis of a Systematic N-Doped Graphene Material Set

300 mg of GO was dispersed in 200 mL of deionized water by bath sonication (VWR Aquasonic 150T) for 1 h, and then mixed with urea in a 1: 30 mass ratio and with uric acid in a 1: 10 mass ratio, respectively. The mixture was stirred for 1 h and then sealed in a 300 mL Teflon-

lined autoclave and remained at 175℃ for 12 h. After the autoclave was cooled down to the room temperature, the solids were filtered and washed and finally dried by lyophilization. The samples after this one-pot hydrothermal process are named as NG-U and NG-UA (i.e., N-doped reduced GO (NG) with urea and uric acid as the nitrogen precursor), respectively. One rGO sample was also prepared using the same experimental procedure but without addition of the N precursor, which serves as the control for NG-U and NG-UA samples.

Further, two annealed samples were prepared for each N-precursor set. NG-U or NG-UA was transferred to a tube furnace (Thermo Scientific Lindberg/Blue M TF55035A-1) and heated to the target temperature at a heating rate of 5 ℃ min^{-1} and annealed for 30 min under a helium gas flow. The samples after annealing NG-U at 650 ℃ and 950 ℃ are denoted by NG-U-650 and NG-U-950, respectively. The samples after annealing NG-UA at 650 ℃ and 800 ℃ are denoted by NG-UA-650 and NG-UA-800, respectively.

4.2.3 Material Characterization

N-doped graphene samples were characterized using X-ray photoelectron spectroscopy (XPS, to determine the elemental composition and distribution of N-types through peak deconvolution of N1s spectra), Raman spectroscopy (to determine defect density and the shift between *n*- and *p*-doping), transmission electron microscopy (TEM, to evaluate the morphology and obtain the mapping of elemental distribution), Brunauer-Emmett-Teller (BET) analysis (to measure the surface area), and methylene blue (MB) adsorption (to evaluate the dispersed surface area in suspension). The methodological details of these characterization techniques are described below.

XPS. Surface elemental composition of all samples were analyzed by XPS operating in a Thermo Scientific ESCALAB 250Xi instrument with a monochromatic Al Kα X-ray source (1486.7 eV) and a 650 µm spot size. The survey spectra were obtained at 150 eV of pass energy and 1.0 eV of step size and were used to determine the elemental composition. The high resolution C1s and N1s spectra were collected at 50 eV of pass energy and 0.1 eV of step size. Triplicate measurements in different positions of each sample were conducted and the data were presented as averages with standard deviations. Peak deconvolution of N1s spectra was carried out using Thermo Scientific Avantage software. A Shirley-derived background was used for spectral substation and C-C at 284.8 eV was used for energy scale correction. Two N-containing polymers, poly(3,5 pyridine) and polypyrrole were used as the reference standards to obtain the peak fitting constraints for binding energies of pyridinic-N (398.7 eV) and pyrrolic-N (399.8 eV), respectively. The peak fitting constraint for binding energy of graphitic-N (401.7 eV) was adopted from a previous publication where a nearly pure graphitic-N doped graphene was fabricated.[243] The remaining tail region toward high binding energy was assigned to N-oxide (centered at ~404 eV). Peak positions were constrained to shift within ±0.3 eV from the assigned binding energies, and values of full width at half maximum (FWHM) for all four components were kept at the same level between components with ±0.2 eV deviation and at least as large as the values measured from two reference polymers.

Raman spectroscopy. Raman spectra were collected by a Horiba Scientific XplorA Raman-AFM/TERS system with an excitation wavelength of 638 nm. Three measurements at different locations of each sample were performed. The intensities and positions of D and G peaks were determined by fitting D peak with a Lorentzian character and G peak with a Breit-Wigner-Fano (BWF) function due to its asymmetry shape[122, 123] after a polynomial baseline subtraction.

TEM. Electron microscopy imaging was conducted on a JEOL JEM-2100F transmission electron microscope operated at 200 kV and equipped with an Oxford Aztec energy dispersive X-ray spectroscopy (EDS) with windowless solid-state silicon drift detector for elemental analysis. The morphology of all graphene samples was studied at TEM mode, while the mapping of elemental distribution within selective areas of the graphene sheets was carried out at scanning transmission electron microscopy (STEM) mode. TEM specimens were prepared by applying 10-20 μL suspensions of graphene (100 μg mL^{-1}) in ethanol onto holey carbon films supported on Cu TEM grids.

BET analysis for surface area measurement. Surface areas of samples in powder form were measured on a Micromeritics ASAP 2020 surface area analyzer using nitrogen adsorption at liquid nitrogen temperature (-196 °C). A relative pressure (P/P_0) range of 0.06 to 0.20 was used to determine the BET surface areas.

Surface area in suspension measured by MB adsorption. A sample suspension in water (0.1 mg mL^{-1}) after 1 h bath sonication was mixed with a MB solution (0.05 mg mL^{-1}) in a 1:1 volume ratio. The mixture vials in triplicate were shaken for 24 h in a rotator at room temperature to achieve the adsorption equilibrium. Then the free MB was isolated from the solution by centrifugation at 12,000 rpm for 15 min and its concentration was determined by measuring its light absorbance at 663 nm using a UV-vis spectrophotometer (Thermo Scientific Evolution 201).

The literature value of 2.54 m^2 of surface area covered by 1 mg of adsorbed MB[244, 245] was used to calculate the surface area of all samples in deionized water, as shown in the following equation. M_{MB} is the mass change of MB after the equilibrium incubation, and M_{Sample} is the mass of the sample.

$$\text{Surface area } (\mathrm{m}^2\ \mathrm{g}^{-1}) = 2.54(\mathrm{m}^2\ \mathrm{g}^{-1}) \times \mathrm{M}_{\mathrm{MB}}(\mathrm{mg})/\mathrm{M}_{\mathrm{Sample}}(\mathrm{mg}) \qquad (4\text{-}1)$$

4.2.4 Evaluation of Biological Activity

GSH oxidation by the NG samples. GSH oxidation by the NG samples was evaluated following the same procedure detailed in our previous publications.[21, 22, 166, 187] Briefly, reduced GSH (0.4 mM) was exposed to the NG samples (0.05 mg mL^{-1}, buffered at pH=8.6) and monitored for 6 h in the dark at room temperature under constant rotation. Measurements were performed at different time points (0.25, 0.5, 1, 2.5, 4, and 6 h). At each time point, the suspension was passed through a 0.22 µm syringe filter (MilliporeSigma) to remove the graphene sample. 0.9 mL of the filtrate was then combined with 1.57 mL Tris-HCl buffer (pH=8.3) and 30 µL of Ellman's reagent (0.1 M). The absorbance at 412 nm was measured using a UV-vis spectrophotometer and then used to determine the concentration of non-oxidized GSH. The percent loss of GSH was calculated compared to the control (no NG). Average and standard deviations were determined from three replicates.

Kinetic rates of GSH oxidation were calculated following our previous studies.[166, 187] Rapid adsorption of reactant (i.e., GSH) and desorption of product (e.g. glutathione disulfide) from the sample surface is assumed in the kinetic model. The interaction between GSH and the NG samples is expressed with the following first-order rate law:

$$-\frac{(\mathrm{d}[\mathrm{GSH}])}{\mathrm{d}t} = k[\mathrm{GSH}][\mathrm{NG}] \rightarrow \ln[\mathrm{GSH}] = -k[\mathrm{NG}]t + \mathrm{C} \tag{4-2}$$

where k is the rate constant (mL mg^{-1} h^{-1}), [GSH] is the concentration of free GSH in solution, [NG] is the concentration of the NG sample (0.05 mg mL^{-1}), C is a constant of this integration equation and denotes the natural logarithm of the initial GSH concentration.

Antibacterial activity of the NG samples in suspension. E. coli K12 (CGSC #7740, Yale Coli Genetic Stock Center, New Haven, CT, USA) was used as a model Gram-negative bacterium to evaluate antimicrobial activities of the NG samples. Cultures were grown overnight in LB Lennox broth at 37 °C and harvested at mid-exponential log phase. To remove residual growth-medium constituents prior to exposure to the prepared NG samples, cell cultures were (i) centrifuged at 10,000 rpm for 1 min to pellet cells, (ii) the supernatant was decanted and replaced with saline solution (0.9% NaCl), and (iii) the cells were re-suspended in saline solution. This washing step was repeated three times.

The NG samples (0.2 mg mL^{-1}) dispersed in saline solution were bath sonicated for 1 h before being exposed to the bacteria. For the exposure, 3 mL of the sonicated NG samples was mixed with 30 µL of bacteria solution (~10^7 colony forming units (CFU) mL^{-1}) for 4 h at room temperature under constant rotation. In addition to directly plating the suspension after 4 h exposure, the bacteria suspension was bath sonicated for 10 min after the 4 h reaction release viable bacteria that are wrapped by NG aggregates, as in previous studies.[58, 64, 83, 94, 246] After both the exposure period and the sonication step, bacteria inactivation was evaluated using a colony counting method. Briefly, 100 µL of bacteria suspension was immediately plated on LB agar plates and incubated for 17 h at 37 °C for CFU enumeration. The percent inactivation was calculated by comparing the exposure to the control (i.e., bacteria solution without the NG samples). All treatments were prepared in triplicate and repeated in three independent experiments. All materials and chemicals used for antimicrobial activity experiments were sterile.

GraphPad Prism version 8.1.0 (La Jolla, California, USA) was used to assess the difference in the GSH oxidation and the bacterial inactivation by rGO and NG samples. One-way ANOVA with Tukey's multiple comparison test was used to compare three or more treatments at each time point, and two-tailed *t*-test was used when there were only two treatments to compare. Moreover, linear regression model was applied for GSH oxidation results and the slopes of curves from different treatments were compared via the extra sum-of-squares F test. The significance level is 95%, i.e., *P* values smaller than 0.05 are considered statistically significant.

4.2.5 Electrochemical Measurements

For electrochemical characterization, the working electrodes were prepared as follows: (i) 2 mg of sample was mixed with 600 µL deionized water, 390 µL isopropanol, and 10 µL of Nafion (5 wt%) followed by 15 min probe sonication (Branson S-450 digital ultrasonic homogenizer) and 2 h bath sonication to form a well-dispersed suspension, (ii) 10 µL of the dispersed mixture was carefully deposited on the glassy carbon disk electrode surface (0.1963 cm^2) and dried at room temperature for 2 h. The working electrodes were then tested in a three-electrode cell with a platinum counter electrode and an Ag/AgCl reference electrode. The values of potential are referenced against Ag/AgCl unless otherwise specified. Also, commercial noble metal catalysts Pt/C and IrO_2 were used as reference materials for ORR and OER, respectively.

The ORR experiments by rotating ring-disk electrode (RRDE) voltammetry were carried out using the same procedures described in our previous research.[187] Briefly, 1 M KOH electrolyte solution was used for all ORR experiments. Prior to each measurement, the electrolyte was bubbled with N_2 for 30 min and the working electrode was cleaned by cyclic voltammetry for 25 cycles sweeping from 0.2 to -1 V. Next, the electrolyte was saturated with O_2 for 30 min before performing RRDE tests. RRDE voltammetry was conducted from 0.2 to -1 V at a scan rate of 5 mV s^{-1} with varying rotating speeds of 400, 625, 900, 1600, and 2500 rpm. The ring potential was held at 0.5 V. The electron transfer number (n) and the percentage of H_2O_2 released during ORR were determined using the following equations:

$$n = \frac{4I_D}{I_D + \frac{I_R}{N}} \tag{4-3}$$

$$\%\mathrm{H_2O_2} = 200 \times \frac{\frac{I_R}{N}}{I_D + \frac{I_R}{N}} \tag{4-4}$$

where I_D is the measured disk current (mA), I_R is the measured ring current (mA), and N is the H_2O_2 collection coefficient at the ring (25.6%, provided by PINE Research Instrument). The onset potentials of ORR polarization curves were determined from the intersection of the tangents between the baseline and the rising reduction current.

The OER experiments using rotating disk electrode (RDE) were performed in 1 M KOH electrolyte from 0 to 0.7 V with a scan rate of 5 mV s^{-1} and a rotating speed of 1600 rpm. The electrolyte was saturated with O_2 before the experiments and the O_2 flow was maintained over the electrolyte during the measurements to ensure the O_2/H_2O equilibrium.

4.3 Results and Discussion

4.3.1 Preparation and Characterization of Systematically Modified N-Doped Graphene

Changing nitrogen precursors and annealing temperatures effectively tunes the N-doping states. The hydrothermal method was used to synthesize NG samples because it is a facile and eco-friendly method compared to other complex, low-yield, and costly techniques such as chemical vapor deposition and nitrogen plasma process.[43, 73, 74, 245, 247] The hydrothermal method has also been shown to attain a higher level of nitrogen doping compared to other methods such as thermal annealing, electrothermal reaction, and arc-discharge.[42, 43, 247] In the hydrothermal process, supercritical water acts as an alternative green reducing agent to organic solvents. Nitrogen precursors are mixed with GO in a hydrothermal autoclave reactor, and nitrogen doping occurs concomitantly with the elimination of oxygen groups on the GO. Given that nitrogen precursors affect the nature of N-types in NG,[72] urea and uric acid were used as nitrogen sources to introduce distinct properties and further different performance of samples between two precursor NG sets. A comparison of two precursor NG sets is anticipated to identify the governing material properties leading to more conclusive results.

There are four primary nitrogen configurations observed in NG: pyridinic-N, pyrrolic-N, graphitic-N, and N-oxide (Figure 4.1).[42, 74, 229, 241] Pyridinic-N and pyrrolic-N are located on graphene edges, the pyridinic structure is sp^2 hybridized and bonded to two carbon atoms while the pyrrolic structure is sp^3 hybridized and incorporated into five-membered ring. Graphitic valley and center nitrogen configurations refer to the sp^3 N atoms within the six-membered carbons. N-oxide refers to the nitrogen bonded with two carbon atoms and one oxygen atom. These nitrogen bonding types play profoundly different roles in tuning the graphene electronic properties, providing a *p*-type doping (electron-deficient, higher tendency to withdraw electrons) by pyridinic- and pyrrolic-N and a *n*-type doping (electron-rich, higher tendency to donate electrons) by graphitic-N.[227, 231, 232] The type of nitrogen introduced into the carbon lattice of our samples was tailored using thermal annealing at different temperatures (650, 800, 950 °C) after the hydrothermal reaction, leveraging different thermal stabilities of the N-types: graphitic-N > pyridinic-N > pyrrolic-N.[43, 248]

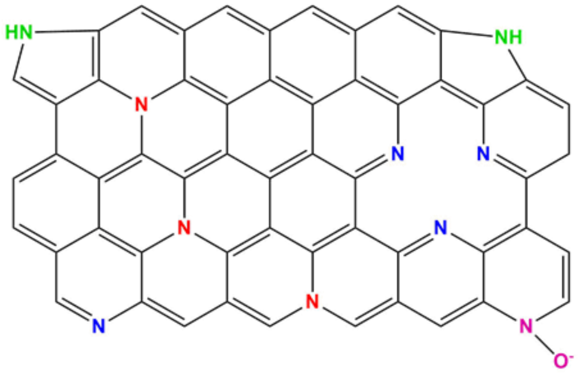

Figure 4.1 Schematic N-doping configurations in N-doped graphene, including pyridinic-N (blue), pyrrolic-N (green), graphitic-N (red), and N-oxide (purple).

XPS was used to quantify the amount and distribution of N-types on our different samples (data compiled in Table 4.1). The results confirm that nitrogen was successfully doped to the graphene lattice and that a systematic distribution of the four nitrogen configurations was achieved. A 9.17% and 6.86% total nitrogen is introduced into the graphene sheets for NG-U and NG-UA, respectively. Upon annealing, the total nitrogen content decreases to 5.70% for NG-U-950 and 3.84% for NG-UA-800, suggesting the removal of thermally unstable N species at these higher temperatures. The annealing treatment enables a self-arrangement and temperature-favored competition among different N-types (see details below on the conversion between N-types). In addition, lower percent oxygen (O%) is observed for NG-U and NG-UA than for the rGO sample, suggesting that the N-doping process reduces oxygen functional groups on GO as a result of competitive doping between oxygen and nitrogen precursors.[242]

To quantify the relative amount of each N-type, the N1s spectra of NG samples were deconvoluted into four components (Figure 4.2). The binding energies for three main peaks including pyridinic-N, pyrrolic-N, and graphitic-N were assigned by constraining the peak positions to 398.7 eV (determined using a standard poly(3,5 pyridine)), 399.8 eV (determined using a standard polypyrrole), and 401.7 eV[243] (based on a previous study on a nearly pure graphitic-N doped graphene), respectively. The remaining small region centered at 404 eV was assigned to N-oxide, which is in good agreement with the literature.[41, 74, 75, 241, 249] The N-bonding configurations in the NG samples fabricated by the one-step hydrothermal method with either urea or uric acid (NG-U and NG-UA) are composed mainly of pyrrolic-N. The subsequent thermal treatment shifts the predominant N to pyridinic-N, for all samples. A decrease in percent pyrrolic-N and pyridinic-N and increase in graphitic-N is observed after a further increase in the annealing temperature. These shifts occur due to different thermal stabilities of N-types, with graphitic-N being the most stable.[43, 248] This conversion from pyrrolic-N to pyridinic-N or graphitic-N shifts the material propensity toward both electrochemical and biological activities.

Table 4.1 Surface chemistry characterization data for N-doped graphene samples attained from XPS spectra, including the atomic percentage of C, O, and N. The atomic percentage of four predominant nitrogen configurations (pyridinic-N, pyrrolic-N, graphitic-N, and N-oxide) are identified from peak deconvolution of the N1s envelope. The values in the parentheses refer to the percentage distribution of four N-types.

Samples	Annealing Temp. (°C)	% C	% O	% N	Pyridinic-N (% total N)	Pyrrolic-N (% total N)	Graphitic- N (% total N)	N-oxide (% total N)
rGO	/	84.97 ±0.46	15.03 ±0.46	/	/	/	/	/
NG-U	/	82.26 ±0.45	8.57 ±0.08	9.17 ±0.38	2.83±0.06 (30.88%)	4.66±0.11 (50.79%)	0.93±0.01 (10.16%)	0.75±0.04 (8.17%)
NG-U-650	650	88.10 ±0.10	4.88 ±0.06	7.01 ±0.05	3.33±0.04 (47.49%)	2.06±0.04 (29.33%)	1.10±0.01 (15.67%)	0.53±0.01 (7.51%)
NG-U-950	900	90.58 ±0.41	3.72 ±0.35	5.70 ±0.26	2.69±0.08 (47.18%)	1.02±0.07 (17.90%)	1.45±0.02 (25.45%)	0.54±0.05 (9.46%)
NG-UA	/	81.12 ±0.83	12.02 ±0.35	6.86 ±0.48	1.01±0.05 (14.73%)	4.97±0.06 (72.50%)	0.65±0.01 (9.47%)	0.23±0.03 (3.29%)
NG-UA-650	650	91.13 ±0.42	4.63 ±0.44	4.24 ±0.05	2.18±0.03 (51.50%)	1.04±0.03 (24.59%)	0.68±0.04 (15.93%)	0.34±0.02 (7.97%)
NG-UA-800	800	92.98 ±0.23	3.18 ±0.15	3.84 ±0.15	1.96±0.06 (51.10%)	0.54±0.06 (14.11%)	0.97±0.07 (25.20%)	0.37±0.03 (9.58%)

(rGO= the reduced GO after one-step hydrothermal reduction without the addition of nitrogen precursors, serving as the control for NG-U and NG-UA samples; NG-U = N-doped rGO after one-step hydrothermal reduction with urea as the N precursor; NG-UA = N-doped rGO after one-step hydrothermal reduction with uric acid as the N precursor; NG-U-##0 or NG-UA-##0 = thermally annealed NG-U or NG-UA with the maximum temperature indicated by ##0)

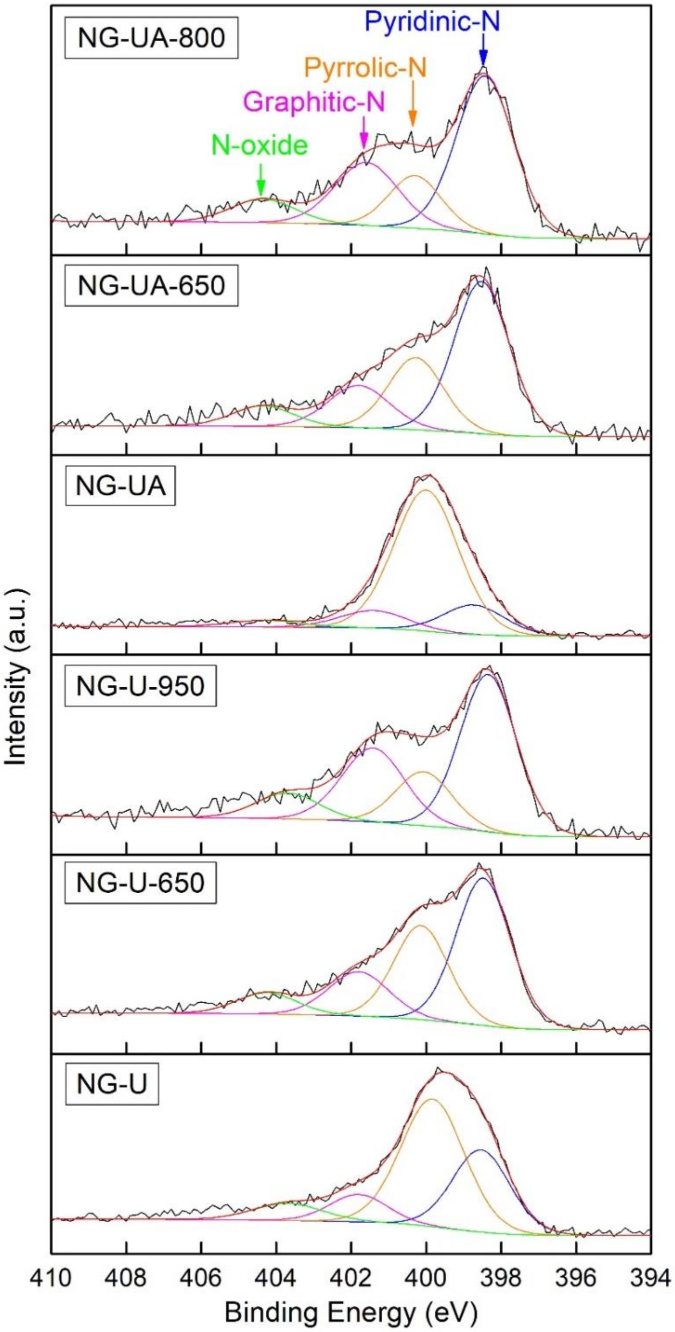

Figure 4.2 Deconvoluted XPS N1s spectra of NG samples. Peak positions for four N components were constrained to shift within ±0.3 eV from the assigned binding energies, and values of full width at half maximum (FWHM) were kept at the same level between components with ±0.2 eV deviation and at least as large as the values measured from two reference polymers (poly(3,5 pyridine) and polypyrrole)

Raman spectra reveal the changes in defect density and the shift between n- and p-type doping. Raman spectroscopy is used to characterize the changes in defect density by comparing the intensity ratio of the D and G peak (I_D/I_G). It can also be used to differentiate the doping types (*n*- or *p*-type) based on the shift of G peak position (Figure 4.3).[232, 250, 251] The broad bump-like 2D region (2400-3250 cm^{-1}) is observed for all samples (Figure 4.4), which is indicative of the high defect density regime.[154, 157, 187] In this regime, an increase of I_D/I_G indicates a decrease in defect density as opposed to the low defect density regime where the increase of I_D/I_G corresponds to an increase in defect density.[154, 157, 187] A higher I_D/I_G is noted for all NG samples compared to rGO, suggesting that N-doping reduces the defects by removing oxygen groups restoring the conjugated graphene structure. NG-U has the highest defect level (i.e., lowest I_D/I_G ratio) among all doped samples. The annealing process after one-step hydrothermal process decreases the defect level through the reduction of N and O functionalities. The annealing at higher temperature does not significantly change the content of defects between NG-U-650 and NG-U-950, while NG-UA-800 exhibits a lower defect level than NG-UA-650.

The effects of doping and the resultant compressive and tensile strain in graphene are possible origins for the shift of Raman peaks.[251] The shift of G peak position is a fingerprint of the concentration of charge carriers and dopants.[251] The downshift of G peak position could be attributed to the incorporation of N atoms leading to *n*-type doping (graphitic-N) while an upshift is observed for *p*-type doping (pyridinic-N, pyrrolic-N).[227, 252] An upshift in the G peak at 1600 cm^{-1} is observed for the rGO sample compared to the value (~1580 cm^{-1}) reported for pure graphene without significant defects (i.e., no D peak is observed).[250] This is due to the presence of residual oxygen functional groups causing a *p*-doping effect.[249] Upon being doped with N, the downshift of G peak position in NG-U and NG-UA suggests that the incorporation of N atoms reduce the effects of *p*-doping. A further downshift of G peak position is noted for the annealed samples, indicating an overall enhanced *n*-doping resulting from a higher content of graphitic-N, which agrees with XPS results.

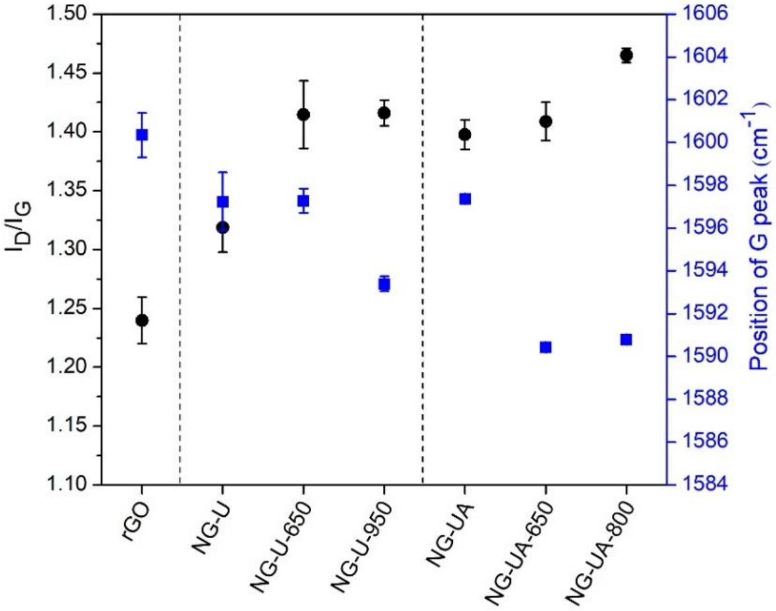

Figure 4.3 Comparison of the I_D/I_G ratios and the position of G peak for rGO and NG samples. The I_D/I_G ratios (left y-axis) and the position of G peak (right y-axis) are displayed by black circles and blue squares, respectively. The error bars stand for the standard deviation of triplicate measurements in different locations of each sample.

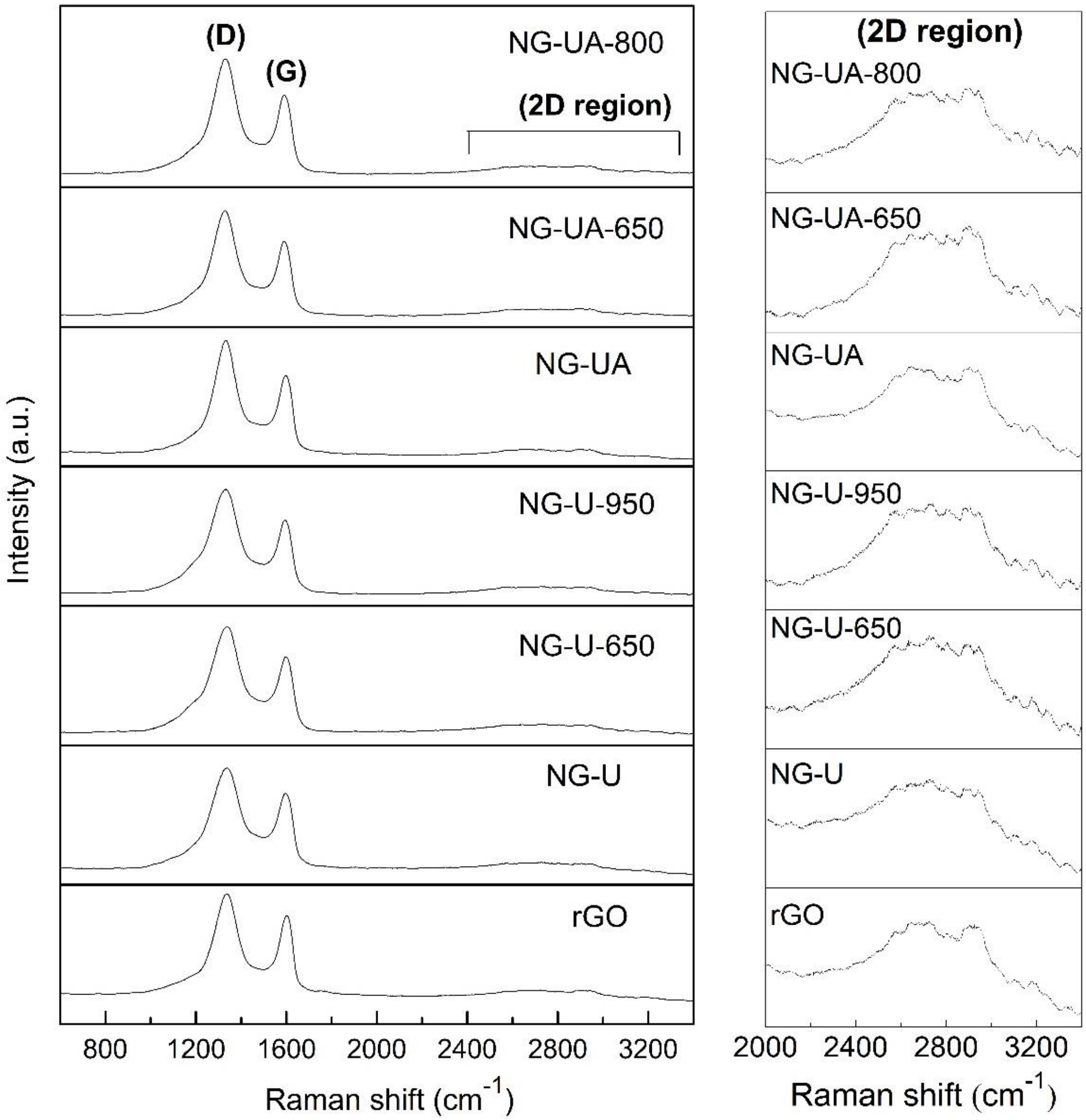

Figure 4.4 Raman spectra of rGO and NG samples with the 2D region magnified on the right.

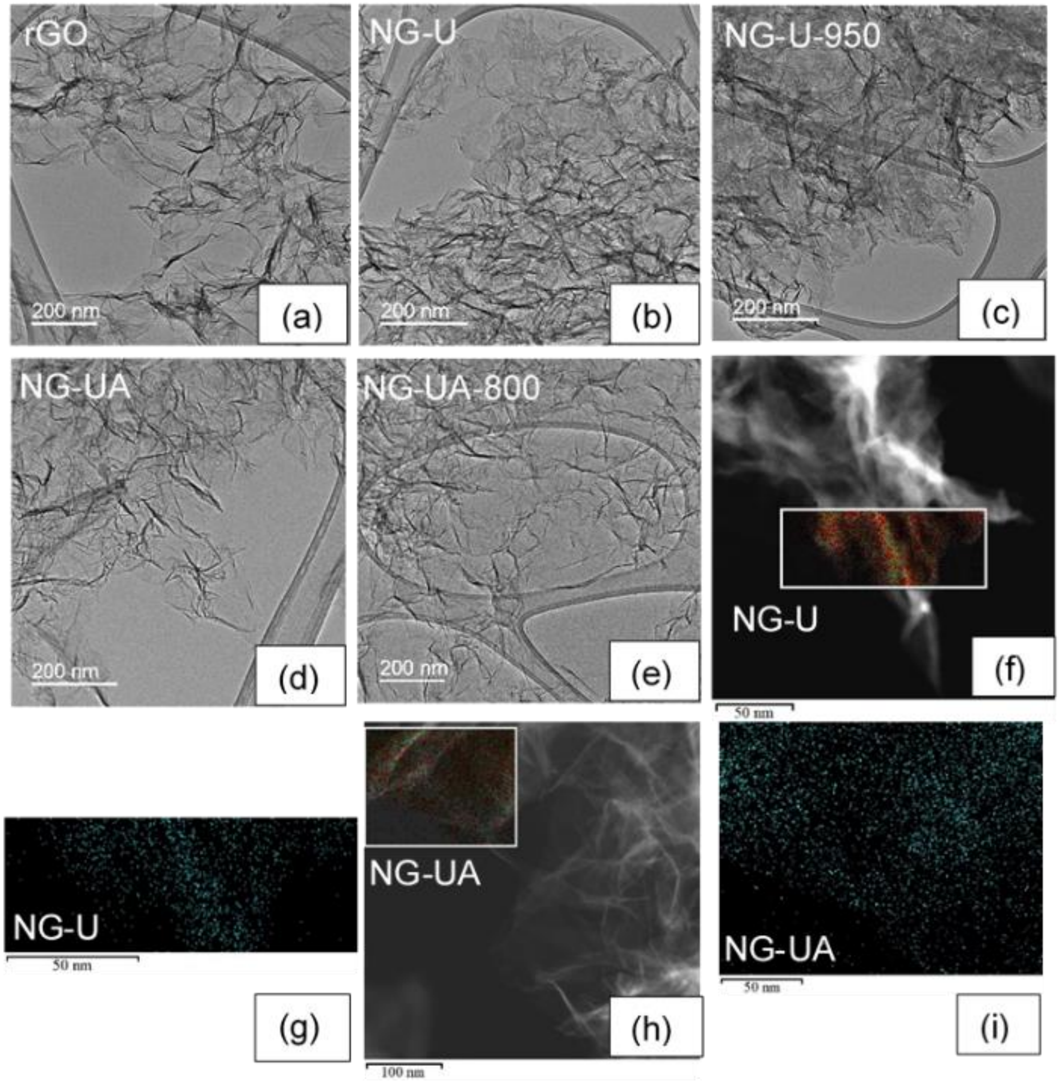

Figure 4.5 TEM images of rGO (a), NG (b), NG-U-950 (c), NG-UA (d), NG-UA-800 (e), and STEM-EDS elemental maps of selected areas (f and h; red dots for C, green dots for O, and cyan dots for N) indicating the distribution of N (g and i, cyan dots) in NG-U and NG-UA, respectively.

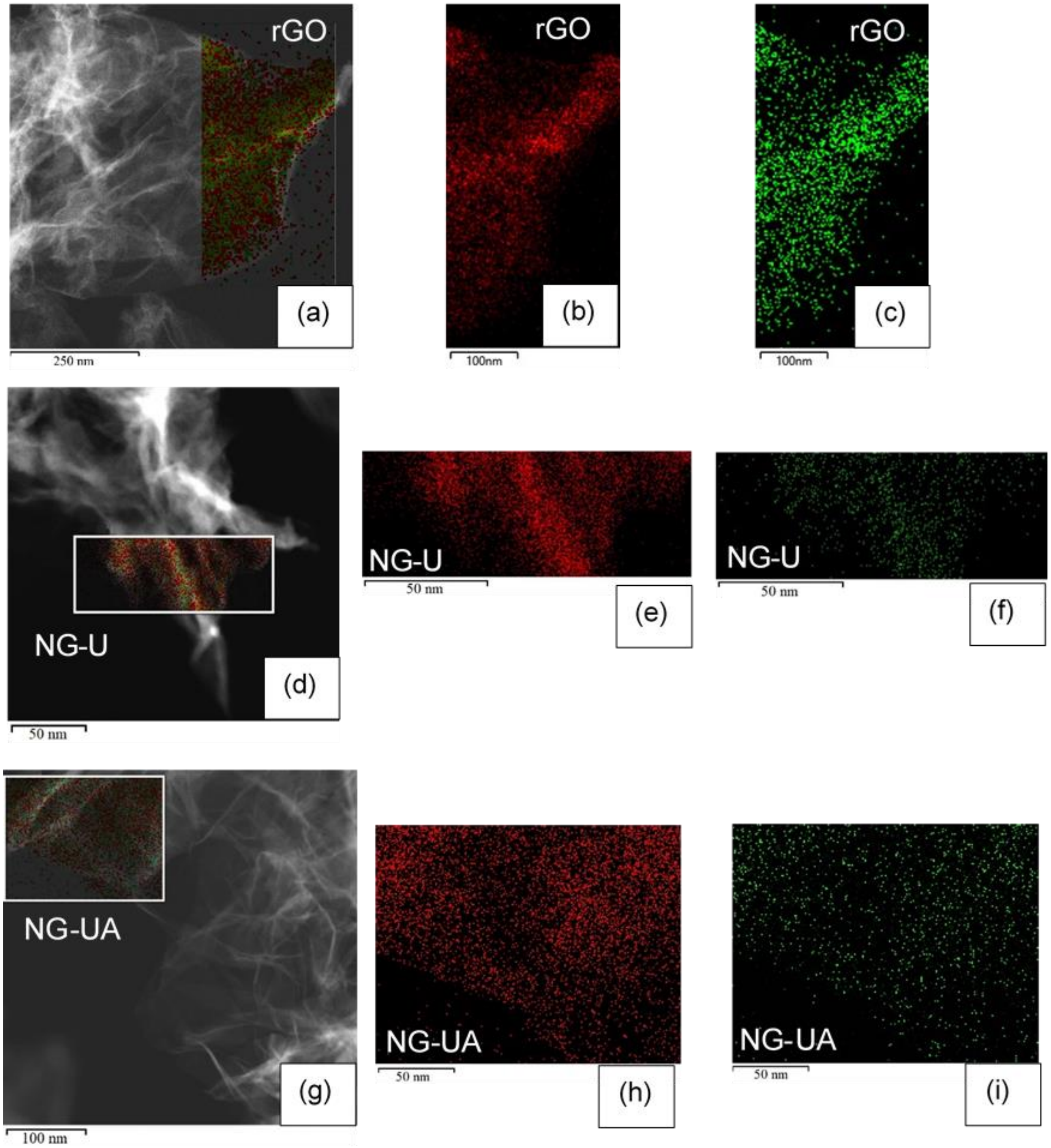

Figure 4.6 STEM-EDS elemental maps of selected areas (a, d, g) indicating the distribution of C (b, e, h; red dots) and O (c, f, i; green dots) in rGO, NG-U, and NG-UA, respectively.

No notable changes in graphene morphology are observed upon N-doping. TEM images of synthesized samples (Figure 4.5), including undoped graphene (rGO), N-doped graphene (NG-U and NG-UA), and N-doped graphene with a further thermal treatment (NG-U-950 and NG-UA-800), show randomly compact and wrinkled multilayer graphene nanosheets. The structure of graphene morphology is well maintained after N-doping, and there is no apparent morphological difference among the five samples, suggesting that N-doping with different nitrogen precursors by the hydrothermal method and the subsequent thermal treatment do not influence the graphene morphology. The distribution of elements in the NG samples is shown by chemical mapping using STEM-EDS. A uniform distribution of N is shown in Figure 3f-i, and that of C and O in Figure 4.6.

4.3.2 Identifying Oxidative Stress as the Dominant Mechanism of Biological Activity

The predominant mechanisms that are proposed to contribute to adverse biological impacts of graphene-based nanomaterials include chemical and physical pathways. Chemical mechanisms primarily refer to oxidative-stress induced by the graphene material, including direct redox reaction at bio-interfaces or indirect via the production of reaction oxygen species (ROS).[55, 58-60, 89] Physical mechanisms include membrane-disruption imposed by the physical interaction with the graphene edges[55, 59, 85, 86] and the wrapping or trapping of organisms given the unique thin 2D structure of graphene sheets.[55, 58, 64, 94, 246] The relative contribution of each mechanism and the ability to manipulate their magnitude of impact remains unresolved. Herein, different NG samples were found to exhibit different propensities for GSH oxidation and *E. coli* K12 inactivation, with the oxidative stress identified to be the dominant mechanism.

The oxidative potential of the NG sample set was assessed by the acellular oxidation of GSH. GSH is a cellular antioxidant and plays a major role in maintainance of a healthly redox balance[60, 253] by oxidizing to its disulfide form (glutathione disulfide, GSSG)[253] to protect against exogenous oxidative agents, such as ROS.[254, 255] The balance of GSH and GSSG serves as a predictor of the ability to defend oxidative stress.[57] Due to the close relevance of GSH to oxidative stress, GSH oxidation is commonly used to probe the level of oxidative stress imparted by graphene-based nanomaterials.[58-60, 187] Further, given that oxidative stress has been shown to be a major mechanism for bacterial cytotoxicity of graphene-based nanomaterials,[59, 246] the depletion of GSH can be correlated with antibacterial activity wherein the effects of bacterial inactivation result from the chemical pathway (i.e., by oxidative stress).

GSH was exposed to rGO and NG samples for 6 h and the measurement of non-oxidized portion of GSH was conducted using Ellman's assay at 1, 2.5, 4, and 6 h. Due to the high activity of NG-UA-650 and -800, additional data was collected at 0.25 and 0.5 h. The magnitude of GSH oxidation is different for the differentially treated samples (Figure 4.7a), while the relative trend between the samples is maintained at all measured timepoints. The kinetic rate constants (k, mL mg^{-1} h^{-1}) determined from the slope of the linear curve fits (ln [GSH] versus time, Figure 4.8) follow the order: NG-U-650 (2.30) < rGO (2.84) < NG-U-950 (7.33) < NG-U (7.97) < NG-UA (13.14) < NG-UA-650 (94.40) < NG-UA-800 (208.27), with a strong fit to the first-order kinetic model ($R^2 > 0.98$). The effect of nitrogen precursors (urea and uric acid) on the oxidative capacity of samples toward GSH is significant; the samples with uric acid as the N-precursor (NG-UA, NG-UA-650 and -800) oxidize GSH considerably faster than those prepared from urea (NG-U, NG-U-650 and -950). Annealing temperatures are also found to influence the oxidative potential of NG samples. As the annealing temperature increases from 650 °C to 800 °C (for uric acid samples) and from 650 °C to 950 °C (for urea samples), GSH oxidation increases from 83% to 100% at 0.5 h and from 46% to 88% at 6 h for samples synthesized from uric acid and urea, respectively. Interestingly, while the annealed samples within the uric acid sample set (NG-UA-650 and -800) induce a higher GSH loss than the non-annealed sample (NG-UA), this trend does not hold for urea samples. NG-U causes similar GSH oxidation compared to NG-U-950, both of which are significantly higher than NG-U-650. The combined GSH oxidation results demonstrate that the prepared samples, with different C:N compositions and distributions of N-types, have different oxidative potentials suggesting induction of differential magnitudes of oxidative stress to bacterial cells.

The antibacterial activity of the NG sample set to the model bacterium *E. coli* K12 was evaluated. A similar trend is observed among the samples for *E.coli* K12 inactivation (Figure 4.7b) and GSH oxidation (Figure 4.7a). For example, increasing the annealing temperature leads to a higher magnitude of cytotoxicity (NG-U-950 > NG-U-650 and NG-UA-800 > NG-UA-650) and the two annealed uric acid samples (NG-UA-650 and -800) demonstrate the highest GSH oxidation and high bacterial inactivation. The similar trends suggest that while physical proximity of the graphene material to the bacteria cell is necessary to induce a response, the dominant mechanism of cytotoxicity is chemical in nature rather than physical puncturing (see additional explanation below). The hydrothermal and thermal annealing treatments do not significantly affect the structure and morphology of the prepared NG samples (see Figure 4.5), suggesting that the physical disruption mechanism induced by sharp edges of graphene (if it exists) is not likely explanations for the observed differences in bacterial cytotoxicity. Rather, the difference in the observed cytotoxic potentials among our samples (e.g., a > 90% loss of cell viability for NG-UA-

650 and -800 versus a < 5% of that for rGO, NG-U-650, and NG-UA) indicates that cell damage is induced through oxidative stress mechanisms rather than physical disruption.

The potential influence of a physical wrapping mechanism has been proposed and can confound conventional culturing approaches to evaluating cytotoxicity by inhibiting bacteial proliferation on agar plates. The effect of wrapping is typically investigated by releasing trapped cells through a mild bath sonication prior to plating.[58, 64, 83, 94, 246] In agreement with previous studies[83, 94, 246], cell entrapment by the NG samples is not observed as there is no statistically significant decrease ($P > 0.05$) in cell viability loss before and after sonication (Figure 4.7b). The combined results from the GSH oxidation and the cell inactivation support the dominant role of oxidative stress in the biological reactivity of our NG samples and their diverse oxidative potential.

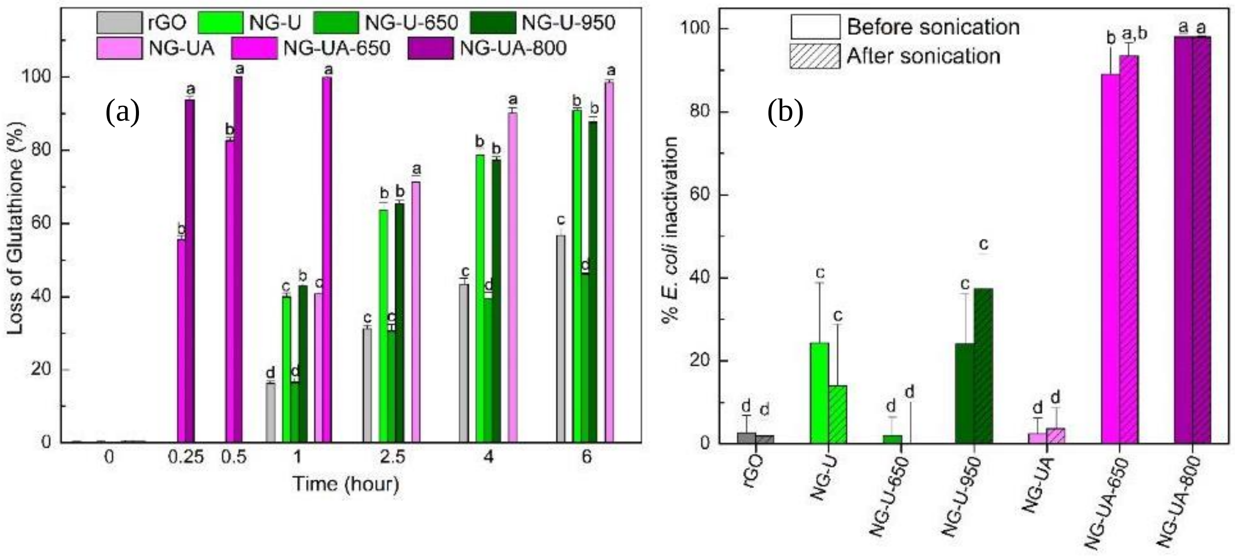

Figure 4.7 Glutathione (GSH) oxidation and cytotoxicity to *E. coli* K12 for rGO and NG samples. (a) GSH oxidation for a total 6 h of incubation compared to the control (no rGO/NG). The mass loading of samples is 0.05 mg mL^{-1} and the initial concentration of GSH is 0.4 mM. (b) Cytotoxicity to *E. coli* K12 after 4 h of reaction to 0.2 mg mL^{-1} sample before and after 10 min bath sonication to release viable bacteria wrapped in aggerated graphene sheets. The data were normalized to the control (saline solution without rGO/NG), the cell concentration of the control remained constant after the 4 h incubation and after the 10 min sonication. Means suffixed with different letters (a-d) for each time point are significantly different from each other at *P* < 0.05. Error bars denote the standard deviations of sample replicates.

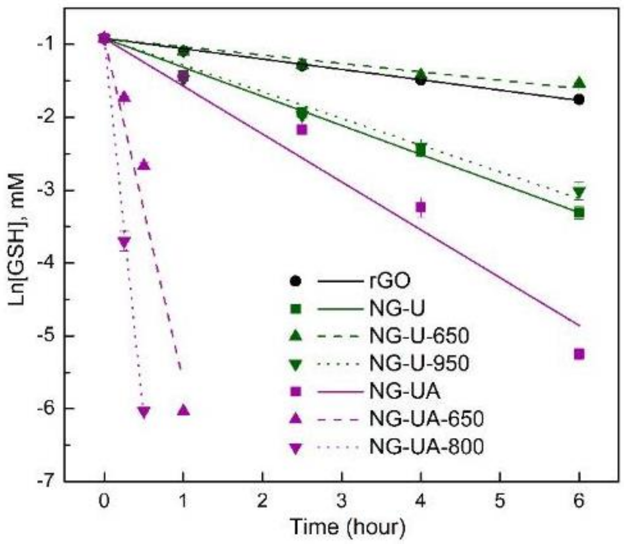

rGO: $y = -0.1421x - 0.9163, R^2 = 0.9997$

NG-U: $y = -0.3984x - 0.9163, R^2 = 0.9992$

NG-U-650: $y = -0.1150x - 0.9163, R^2 = 0.9973$

NG-U-950: $y = -0.3665x - 0.9163, R^2 = 0.9960$

NG-UA: $y = -0.6568x - 0.9163, R^2 = 0.9886$

NG-UA-650: $y = -4.7198x - 0.9163, R^2 = 0.9813$

NG-UA-800: $y = -10.4134x - 0.9163, R^2 = 0.9988$

Figure 4.8 Plots of natural logarithm of the GSH concentration (ln [GSH], mM) versus time by applying the first-order kinetic model to the GSH oxidation mediated by rGO and NG samples. The kinetic rate constants (*k*, mL mg^{-1} h^{-1}) follow the order: NG-U-650 (2.30) < rGO (2.84) < NG-U-950 (7.33) < NG-U (7.97) < NG-UA (13.14) < NG-UA-650 (94.40) < NG-UA-800 (208.27). *k* is significantly different between all samples (*P* < 0.05), except for NRG-U versus NRG-U-950 (*P* = 0.12). Three replicates were measured at each time point. Geometric symbols represent the mean values of ln [GSH] at each sampling time over the mean concentration of the control (no rGO/NG). Error bars indicate the standard deviation (*n* = 3).

4.3.3 Evaluation of Oxygen Reduction Reaction (ORR) and Oxygen Evolution Reaction (OER) Validates Different Electron Transfer Properties as a Function of N-Type

ORR and OER are electrochemical processes that underlie clean energy technologies, including water splitting, fuel cells, and metal-air batteries.[15, 42, 44] Graphene-based nanomaterials have been pursued as metal-free catalysts to replace the noble-metal commercial catalysts (e.g., Pt, Ir, Ru) that are scarce and high-cost.[15, 42, 44, 226] Further, nitrogen-doped graphene has been extensively studied in the field of ORR and OER.[42, 66, 73, 75, 226] As such, ORR and OER are used in this work to represent the desired functional performance of NG materials. Also, given the importance of oxygen and electron transfer in the mechanisms of biological activities,[21, 22, 187] the evaluation of ORR and OER activities of NG will be useful for a better understanding of the underlying mechanism of interaction at the bio-interface. Herein, the evaluation of functional electrochemical activities, ORR and OER, of NG samples validate different electron transfer properties as a function of nitrogen type.

The enhanced ORR and OER activities are driven by properties of graphene-based materials, including the (i) electrical conductivity for electron transport within the graphene plane,[78-80] (ii) defects (topological and edge defects) that offer active sites,[81, 82] (iii) electroactive surface area available for accessing active sites,[80] and (iv) presence of functionalities (e.g., pyridinic-N, graphitic-N) that induce active sites for accelerating the adsorption of targets (and the intermediates) and favor electron transport for the reaction.[66, 75, 256] While the ORR reduces O_2 to H_2O, OER can be considered the opposite reaction in which H_2O oxidizes to O_2. Considering this inherently different mechanisms between ORR and OER, the active N moieties in NG to influence each activity will depend on their ability to donate or withdraw electrons.

ORR and OER are commonly carried out in a hydrodynamic condition. This enhances mass transfer by inducing convection so that steady-state diffusion is achieved, enabling elucidation of the kinetics and the mechanism of electrode reactions with high precision measurements. [53] RRDE and RDE measurements were performed for ORR and OER, respectively. Both experiments were conducted in alkaline media due to the advantages in terms of a decreased overpotential and a less corrosive environment compared to the process in acidic media.[51] Enhancement in ORR and OER activities is typically represented by a more positive onset potential and a higher absolute value of the current density on the potential-current polarization curves.

Trends in ORR polarization curves for rGO and NG samples are displayed in Figure 4.9a with the Pt/C curve shown for comparison. While rGO and NG samples demonstrate a poor ORR activity compared to Pt/C (as the reference), different ORR activity is observed between samples, with the trend in onset potential: NG-U-650 (-0.189 V) < rGO (-0.179 V) < NG-UA (-0.169 V) ~ NG-UA-650(-0.169 V) < NG-U-950 (-0.164 V) < NG-U (-0.159 V) < NG-UA-800 (-0.149 V). After the one-step hydrothermal synthesis, NG-U demonstrates a better electrochemical activity than NG-UA, indicating there are different interactions between urea and uric acid with GO during the hydrothermal synthesis. The subsequent annealing process results in a more pronounced increase in the electrochemical reactivity of samples within the uric acid precursor set than that within the urea precursor set.

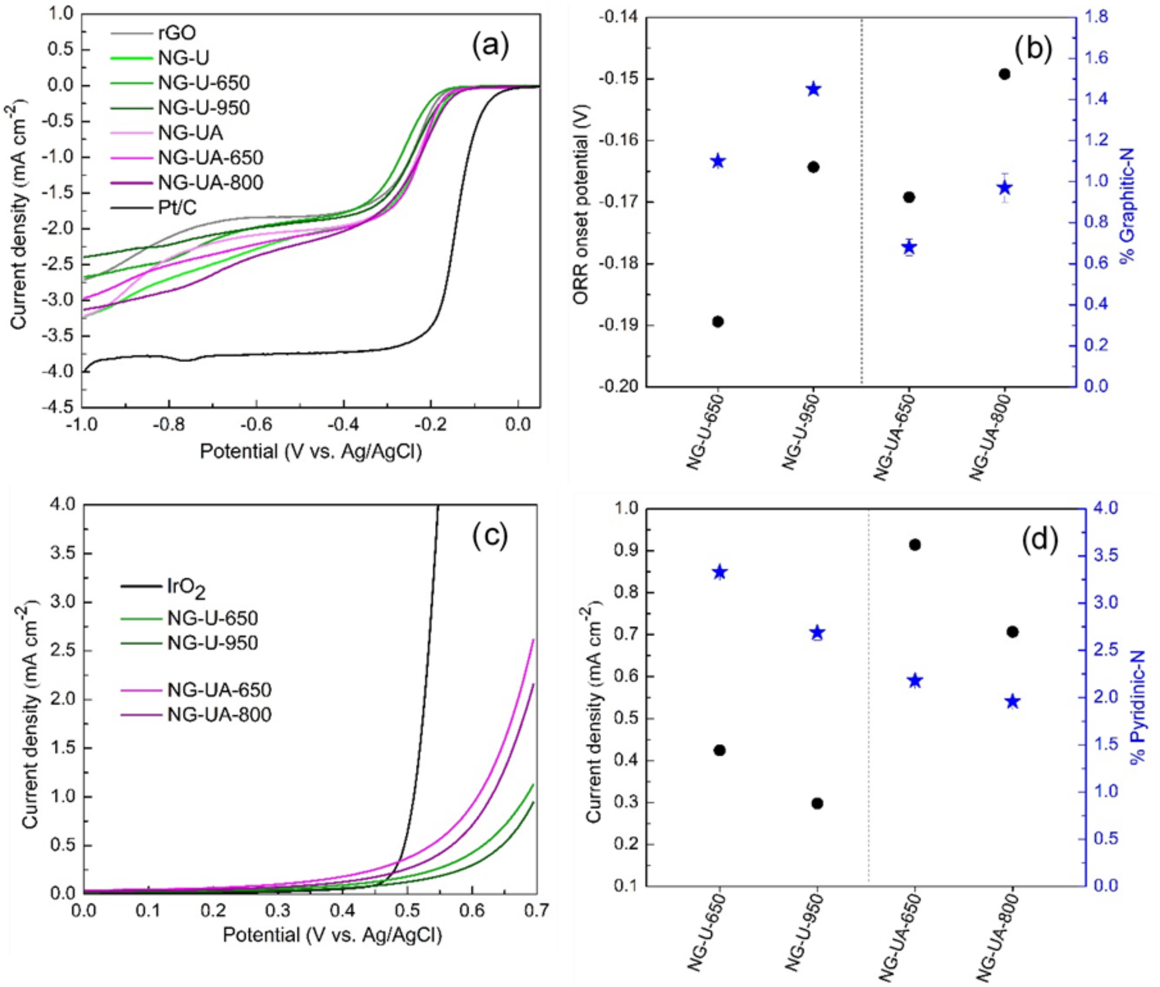

Figure 4.9 ORR and OER polarization curves and the correlation between the ORR/OER performance and the percent of graphitic-N/pyridinic-N. (a) ORR polarization curves of rGO, NG samples, and Pt/C on RRDE in O_2 saturated 1 M KOH with a rotation rate of 1600 rpm and a scan rate of 5 mV s^{-1}. (b) The correlation between the ORR performance of NG (represented by the onset potential) and the percent of graphitic-N (determined by XPS). (c) OER polarization curves of annealed NG samples and IrO_2 on RDE in O_2 saturated 1 M KOH with a rotation rate of 1600 rpm and a scan rate of 5 mV s^{-1}. (d) The correlation between the OER performance of annealed NG samples (represented by the current density at a potential of 0.6 V) and the percent of pyridinic-N (determined by XPS).

The electron transfer number (n) and the H_2O_2 yield (H_2O_2 %) were calculated by employing RRDE (Figure 4.10). ORR in alkaline media can occur by either a two-electron ($O_2 + H_2O + 2e^- \rightarrow HO_2^- + OH^-, HO_2^- + H_2O + 2e^- \rightarrow 3OH^-$) or a four-electron ($O_2 + 2H_2O + 4e^- \rightarrow 4OH^-$) pathway thus, a higher *n* represents a lower H_2O_2 yield. The four-electron pathway is advantageous for energy applications because the H_2O_2 intermediates produced in the two-electron pathway will deteriorate the catalysts and lead to a decline in the O_2 utilization rate.[127] At the potential ranging from -0.4 to -1.0 V, the *n* calculated for all samples falls within a range of 3.5 (25% H_2O_2) to 3.9 (5% H_2O_2), suggesting a predominant 4-electron oxygen reduction pathway. In general, NG-UA and NG-UA-650 show a lower *n* than rGO over this potential range while other samples enhance *n*, which suggests that the C:N compositions and distribution of N-types influences the reduction pathway.

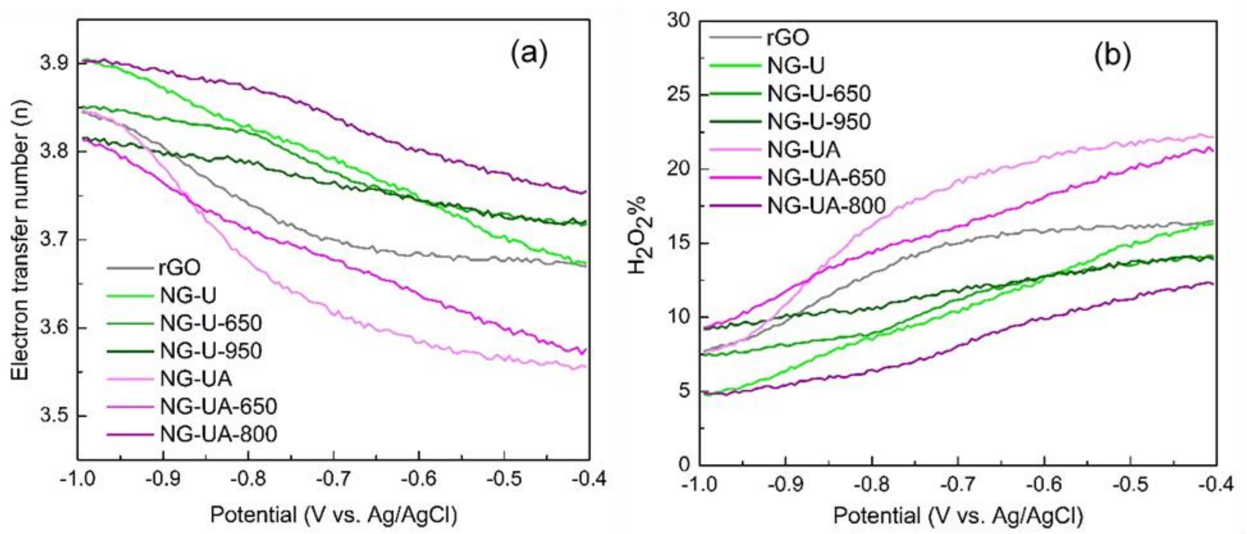

Figure 4.10 Electrochemical indicators for the ORR performance of rGO and NG samples, including (a) the electron transfer numbers *n* and (b) the yield of H_2O_2, H_2O_2%. *n* and H_2O_2% were determined by RRDE.

The capacity of graphene materials to catalyze ORR depends on the defect density because defect sites can enhance the O_2 adsorption.[60] The higher defect density in NG-U explains the favorable reactivity toward ORR. While annealing decreases the defect density and subsequently suppresses the ORR activity, we observe an increasing ORR trend between NG-U-650 and NG-U-950 (having similar defect density), and between NG-UA-650 and NG-UA-800 (the latter having a lower defect density). This indicates that another property of these materials is involved in the observed difference in ORR activity. The proportion of different N-types, rather than the nitrogen content on the graphene, has been proposed to play an important role in the facilitation of electrocatalytic activity.[66, 256-258] Graphitic-N possesses the electron-donating characteristic[227, 231, 232] and greater charge carrier transport over other N-types.[230, 231] Graphitic-N atoms can lower the O_2 adsorption barrier by decreasing the repulsive interaction between graphene π electrons and lone pair electrons of O_2,[256, 258] and can facilitate the donation of electrons to the adsorbed O_2 to form OOH species,[66, 259] both of which are key steps to enhance the reduction of O_2 in alkaline solution. As a result, the samples annealed at higher temperatures demonstrate enhanced reactivity toward ORR due to the increase in the content of graphitic-N (Figure 4.9b).

The electrocatalytic activity of the annealed samples within urea and uric acid precursor sets was investigated toward OER to determine whether the predicted opposing trend is observed as predicted; samples with more pyridinic-N would have a greater propensity towards OER. Indeed, the opposite trend (Figure 4.9c and 4.9d) is observed for OER compared to that for ORR. The samples annealed at higher temperatures (having 2.69% and 1.96 % pyridinic-N for NG-U-950 and NG-UA-800, respectively) demonstrate lower OER activity in terms of the current density than that at lower temperatures (having 3.33% and 2.18% pyridinic-N for NG-U-650 and NG-UA-650). The carbon adjacent to electron-donating graphitic-N atoms possess a partial negative charge

(δ^-) and therefore can serve as nucleophiles. This behavior is unfavorable for the adsorption of intermediates necessary for water oxidation in the alkaline media (e.g., OH^-, OOH^-).[66, 257] Carbon atoms adjacent to electron-withdrawing pyridinic-N atoms carry a partial positive charge (δ^+), thus serving as electrophiles facilitating the adsorption of intermediates necessary for water oxidation (e.g., OH^-, OOH^-).[66, 260] In addition, the polarized pyridinic-N (δ^-) is not favorable for the reduction of O_2 due to its high density of N lone pair electrons that cause strong repulsive interaction with the O_2 approaching its adjacent carbon atoms.[256] Consequently, the samples annealed at higher temperatures demonstrate lower reactivity toward OER owing to the decrease in the pyridinic-N content.

While samples annealed with uric acid (NG-UA-650 and -800) contain lower percentage of graphitic-N and pyridinic-N than those within urea sample set (NG-U-650 and -950), the uric acid sample set presents an overall higher ORR and OER (Figure 4.9b and 4.9d). This observation suggests another property in contributing to the sample activity and is attributed to the higher surface area of the uric acid materials (Figure 4.11). The Brunauer-Emmett-Teller (BET) surface area for NG-UA-800 is 549.3 $m^2 g^{-1}$ and 428.2 $m^2 g^{-1}$ for NG-U-950, enhancing access to the active sites that facilitate the electrocatalytic activities. The observed differences in BET surface area is maintained when the respective materials are dispersed (see additional details below).

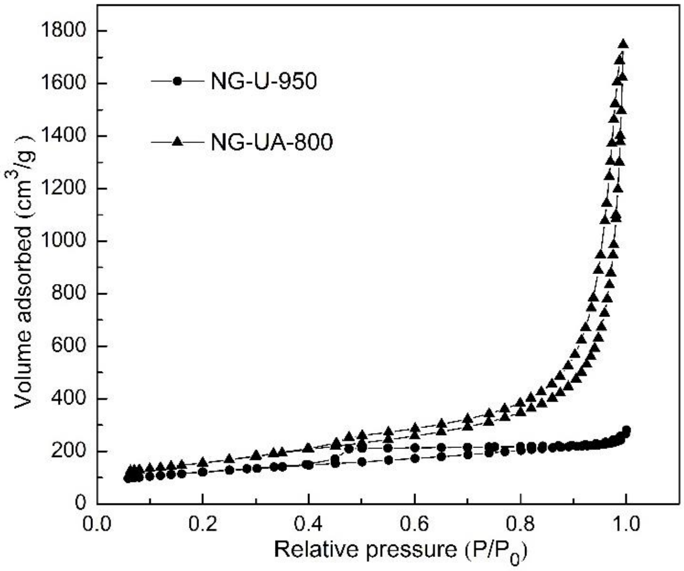

Figure 4.11 Nitrogen adsorption-desorption isotherms for NG-U-950 and NG-UA-800 measured at liquid-nitrogen temperature (-196℃).

Taken together, the characterization data indicate that multiple physicochemical properties of NG influence the electrochemical performance (here, ORR and OER activities). While the consequential material properties that result from N-doping (e.g., defect density, surface area) influence ORR and OER synchronously, opposite trends observed for ORR and OER highlight the significant role of N-types in mediating these two electrochemical activities. While electron-donating graphitic-N and electron-withdrawing pyridinic-N are effective promoters for ORR and OER, respectively, the defect density and surface area that result from different preparation methods (precursors and annealing temperatures) further contribute to the material activity.

4.3.4 The Similarity Between Glutathione (GSH) Oxidation and Oxygen Reduction Reaction (ORR) Reveals the Role of Graphitic-N as the Active Site in Oxidative Stress Related Bioactivity

The evaluation of biological activity of our NG sample set highlights the essential role of oxidative stress at bio-interfaces and affirms that the oxidation of GSH is a good predictor of oxidative stress delivered by our NG samples. Previous studies propose that graphene family nanomaterials catalyze GSH oxidation through electron transfer with dissolved oxygen at the defect sites.[60, 94] The dissolved oxygen (O_2) reacts with active defect sites on graphene forming surface-bound oxygen intermediates (e.g., superoxide anion O_2^-, hydroperoxide OOH) that can oxidize GSH or be released to the bulk solution to form reactive oxygen species (ROS) that react with GSH.[60] The rate-limiting step for the oxidation of GSH is the formation of the surface oxide intermediates (O_2^-, OOH), similar to mechanism for ORR on the electrode surface in alkaline solution. Since O_2 has a high bond dissociation energy, it is not uniformly favorable and requires the formation of intermediates (O_2^-, OOH) that have lower bond dissociation energy.[51, 257] As such, the oxidation of GSH and ORR share a similar mechanism, both of which are dominated by O_2-mediated catalytic process to reduce O_2 that starts with O_2 adsorption on the active sites of graphene materials.[51, 60] It is thus expected that graphitic-N can influence the capacity of NG to oxidize GSH, as it does for ORR.

Similar trends are observed for the oxidation of GSH and the ORR activity within each N-precursor set (urea versus uric acid in Figure 4.12a). As with the ORR trends described above, the important contribution of defects to the oxidization of GSH is underlined by the higher defect density in NG-U than the two annealed samples (NG-U-650 and -950, see Figure 4.3). The samples annealed at higher temperatures within each N-precursor show an increased oxidative potential toward GSH, which is attributed to the increase in the percent of graphitic-N. Yet similar to the ORR trend described above, the samples prepared with the uric acid precursor have lower amounts of graphitic-N than those prepared with urea while exhibiting higher oxidative potential, which is believed to result from the increase in available surface area. Since the GSH assay is performed in the aqueous media, the dispersed surface area of the samples was evaluated by the adsorption of methylene blue (Figure 4.12b). This approach is regarded as a standard method for measuring the surface area of graphitic materials in the aqueous phase.[244, 245] Overall, a higher surface area corresponds with a better dispersion, which is observed for the uric acid samples. A visual comparison of their dispersion in water is shown in Figure 4.13. The increase in the thermal annealing temperatures induces a reduction in the dispersed surface area in both sample sets. This is caused by the removal of surface functionalities, which promotes aggregation of the samples in suspension, thus decreasing the available dispersed surface area.

Collectively, the data supports multiple factors synergistically influencing the NG-mediated oxidation of GSH. In addition to the defect density and dispersed surface area, uncovering the role of graphitic-N in both ORR and GSH oxidation elucidates the underlying mechanisms of oxidative-stress induced biological activity. The similarities in ORR and GSH trends suggests the potential to employ electrochemical tools to evaluate the relative bioactivity of graphene materials via chemical pathways.

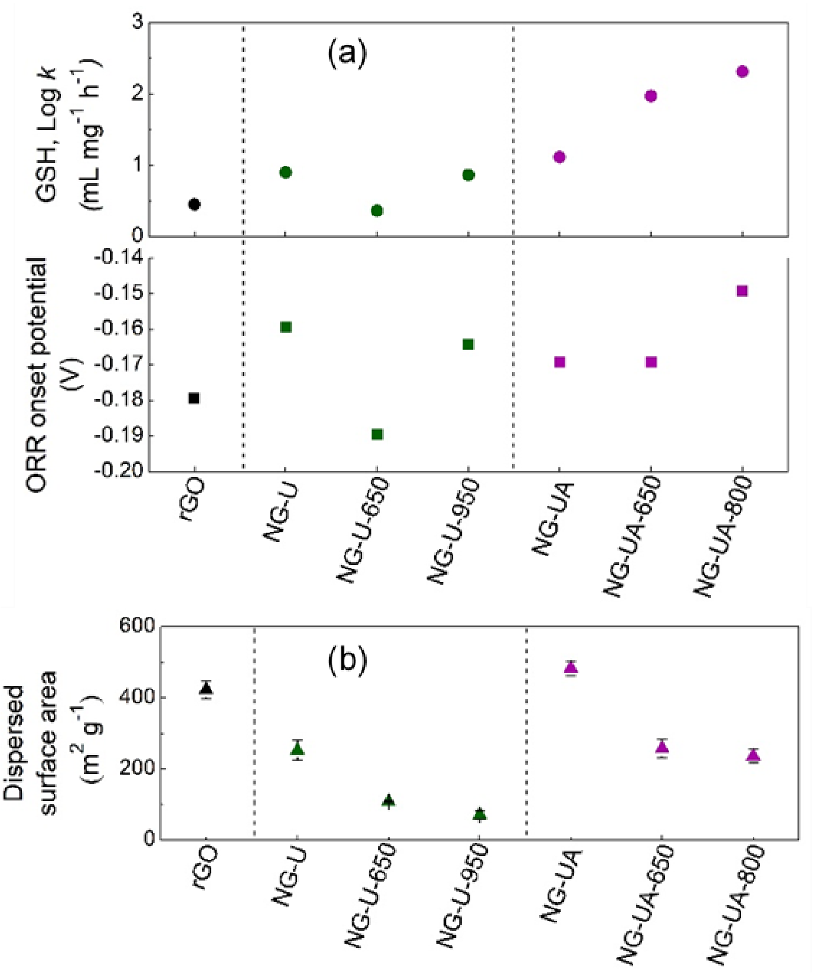

Figure 4.12 (a) The correlated trends between the rate constants for GSH oxidation and the onset potentials for the ORR activity and (b) the dispersed surface areas in suspension determined by the adsorption of methylene blue (MB).

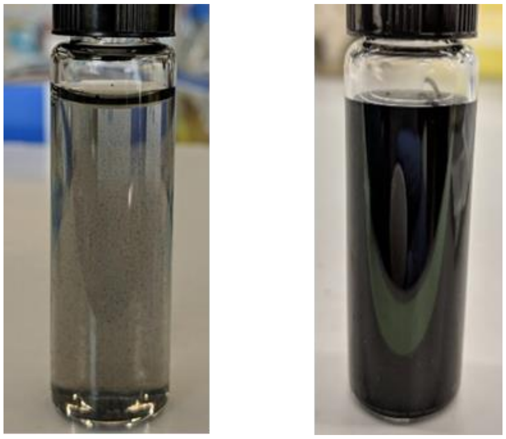

Figure 4.13 Two representative photographs on urea and uric acid samples dispersed in deionized water (0.05 mg mL^{-1}). Left: the urea sample; Right: the uric acid sample.

4.3.5 The Opportunity to Tailor Functional Performance and Inherent Hazard Outcomes

Sustainable design of nanomaterials defines a proactive approach to advance new applications while reducing the potential to introduce hazards to human health and the environment.[3, 5] Results from this study demonstrate that governing N-types are distinct for electrochemical applications given their unique electronic properties. Specifically, graphitic-N is responsible for the reduction of oxygen (ORR) while pyridinic-N is responsible for water oxidation (OER). This suggests the ability to tune performance based on chemical composition, which we demonstrate is possible using different N-precursors and annealing temperatures. While the goal of a sustainable design approach is to enhance functional performance while reducing inherent bioactivity (GSH oxidation, cytotoxicity), a possible outcome is that the same material property modulates both outcomes. This was the result in our previous research on GO/rGO[187,21, 22] as well as in this study for NG and ORR performance. Yet, in studying N-doped graphene herein, we discovered that the ability to decouple functional performance and bioactivity will depend on the desired performance outcome (i.e., ORR versus OER). For example, the functional performance of OER is facilitated by pyridinic-N and the samples with high pyridinic-N have lower oxidative potential, thus suggesting a path towards enhanced performance without high bioactivity. While we used two approaches to modulate N-types of NG, there are many more options that enable further control of N doping to obtain closer to pure graphitic or pyridinic C-N bonding configuration[243, 256] and advance the intended rational sustainable design for their applications.

4.4 Conclusions

The type of N that is incorporated in the graphene structure depends on how the sample is prepared, including the nature of N precursors and annealing temperatures. The different amount of doped N and the relative abundance of N-types differentially influence biological and electrochemical activities. Defect density and surface area are consequential properties that result from changes in N-content and work in concert with chemical composition to modulate both activities. While this work identifies these three properties to govern the measured outcomes (i.e., GSH oxidation, bacterial inactivation, ORR, and OER), the contribution of each property to each outcome differs. For example, the trends in GSH oxidation and bacterial inactivation for the uric acid and urea sample sets are similar, yet the magnitude of the difference between individual samples differs for these two measured biological activities (Figure 4.7a versus 4.7b). These findings elucidate the opportunity to tune (un)desired properties and material activities by modifying graphene chemistry.

While both electrochemical and biological activities are controlled by a balance between multiple properties, the type of N has an overarching effect. Electron-donating graphitic-N is responsible for ORR and O_2-mediated oxidative stress in bioactivity while electron-withdrawing pyridinic-N is responsible enhancement in OER. Identification of N active sites for biological activities is useful to guide the development of N-doped graphene materials for their biomedical and bioanalytical applications. From the perspective of rational design, N-types can be leveraged as a design handle to tailor properties of graphene for specific applications while reducing or maintaining minimal adverse biological effects.

Finally, there is growing evidence of the correlation between electrochemical activity and biological reactivity of carbon nanomaterials including multi-walled carbon nanotubes,[21, 22] graphene oxide,[187] and N-doped graphene (in the present work). Uncovering the underlying electronic nature of graphene, including the ability to engage in electron exchange and transport, is critical to informing the ability to rationally design graphene materials for electrochemical applications while also advancing predictive toxicity capabilities.

5.0 Summary and Research Recommendations

5.1 Summary

A proactive approach to reducing the potential for human and environmental risks alongside the development of novel materials is critically important and has motivated the work in this dissertation to develop rational design guidelines for graphene. The work is unique in studying the functional performance (electrochemical activity) and the hazard (biological activity) in combination for material sets of graphene systematically modified using chemical composition (i.e., O and N chemistries).

Chemical composition manipulation offers the opportunity to control the properties of graphene-based materials (GMs) and tailor the outcomes. Material sets of graphene oxide (GO) and nitrogen-doped graphene (NG) are investigated to determine the material properties - oxygen and nitrogen sites and consequential properties - that govern the electrochemical activities (oxygen reduction reaction (ORR) and/or oxygen evolution reaction (OER)) and the biological activities (glutathione (GSH) oxidation and/or bacterial (*E. coli*) inactivation). In Chapter 2, the carbonyl (C=O) group on the surface of GO is found to influence ORR and GSH oxidation. Interestingly, both activities are not controlled by a single factor; instead, these measured endpoints are influenced by a combination of other properties, including aggregation state, defect density, and electrical conductivity that arise as a consequence of the changing chemical composition.[187] In Chapter 3, a direct reaction between GO and GSH is studied. The combined experimental and computational approach confirms the preferred reaction between GSH and epoxide groups (C-O-C). The computational data further elucidates the reaction mechanism highlighting the supporting role of the hydroxyl group (-OH) in mediating the GO-epoxide and GSH-thiol reaction.[261] In Chapter 4, the graphitic-N and pyridinic-N doped in the carbon lattice of graphene are identified to be the contributors to ORR and OER of NG, respectively. The similar trends observed between GSH and *E. coli* inactivation demonstrate the predominant oxidative stress mechanism in killing the bacterial cells. The similar trends observed and the shared mechanism between ORR and GSH oxidation indicate the active role of graphitic-N in these two activities. In addition to the contributions from the governing N-types, both electrochemical and biological activities are influenced by a balance of consequential properties, including (aqueous) surface area and defect density.[262]

Collectively, the data (Table 5.1) indicate how synthesis methods differentially manipulate the chemical composition (active O and N sites) and influence the governing consequential properties that contribute to enhanced material performance for electrochemical and biological activities being studied. For example, in the GO material set, chemical reduction can produce a comparable chemical composition of rGO sample compared to thermal reduction, but with a relatively lower level of structural defects and a higher electrical conductivity leading to an enhanced electrochemical or biological activity. For the NG material set, where the hydrothermal synthesis technique is employed, lower mass density and higher surface area of NG is obtained using uric acid as the N precursor in comparison to urea. However, the synthetic mechanisms of hydrothermal treatment of GO with these two N precursors is not well understood. In the future work, computational tools (e.g., density functional theory) can be leveraged to better understand the different interaction mechanisms of GO between uric acid and urea and the introduction of N-doping, ideally simulating the hydrothermal synthesis condition. Further, high-resolution TEM and density gradient ultracentrifugation[263] can be employed to explore the influence of N-precursors in the microstructure and thickness of produced NG, respectively. In doing so, the synthetic mechanisms with different N-precursors that cause the differences in material properties (e.g., mass density, surface area, aqueous dispersion, defects, distribution of N-types) will be revealed.

The similar trends in GSH oxidation and bacterial inactivation indicate the dominant mechanism bacteria inactivation is oxidative stress and support the use of the GSH oxidation as a facile assay to predict GM antibacterial action. Further, there is an intimate link between GSH oxidation and ORR activity, both of which involve catalytic reduction of oxygen to adsorbed oxygen intermediates (e.g., O_2^-, OOH). This suggests a potential causal mechanism of inherent toxicity that is driven by the ability for GM to transfer and transport electrons, governed by the surface chemistry and consequential properties identified in this work, including C=O, graphitic-N, structural defects, electrical conductivity, and active surface area. As such, unveiling the electronic properties of GMs will enable a better understanding of interactions of materials with important biological redox reactions, such as those involved in the cellular electron transport chain (e.g., NADH/NAD^+, $FADH_2$/FAD, H_2O/O_2),[102] advancing predictive capability of bioactivities.

Table 5.1 Summary of ranges for the levels of chemical composition (active O and N sites), the governing consequential properties, electrochemical and biological activities for GO and NG material sets.

GO material properties		GO parent material	rGO thermal reduction (200 to 900 ℃)	rGO chemical reduction ($NaBH_4$)
Chemical composition[a]	% C-C	36.98	68.74 – 86.72	74.49
	% C-O	47.48	9.08 – 14.68	15.67
	% C=O	8.74	3.21 – 8.48	5.50
Defect density[b]	I_D/I_G	1.28	1.32 – 1.92	1.40
Conductivity[c]	$(\mathrm{S\ m^{-1}})$	/	0.47 – 13.77	8.54
ORR[d]	onset potential (V)	-0.2143	-0.2744 – -0.2445	-0.1695
GSH oxidation[e]	rate constant, log *K* $(\mathrm{mL\ mg^{-1}\ h^{-1}})$	0.53	-0.45 – 0.40	0.67

NG material properties		rGO hydrothermal treatment	NG hydrothermal treatment + thermal annealing w/ urea precursor	NG hydrothermal treatment + thermal annealing w/ uric acid precursor
Chemical composition[f]	% N	/	5.70 – 9.17	3.84 – 6.86
	% pyridinic-N	/	2.69 – 3.33	1.01 – 2.18
	% graphitic-N	/	0.93 – 1.45	0.65 – 0.97
Defect density[g]	I_D/I_G	1.24	1.32 – 1.42	1.40 – 1.46
Dispersed surface area[h]	$(\mathrm{m^2\ g^{-1}})$	422	70 – 252	236 – 483
ORR[i]	onset potential (V)	-0.1794	-0.1894 – -0.1594	-0.1693 – -0.1492
OER[i]	current density $(\mathrm{mA\ cm^{-2}})$ at 0.6 V	/	0.30 – 0.42	0.70 – 0.91
GSH oxidation[h]	rate constant, log *K* $(\mathrm{mL\ mg^{-1}\ h^{-1}})$	0.45	0.36 – 0.90	1.12 – 2.32
E. coli inactivation[j]	% loss of cell viability	2.7	2.1 – 24	2.5 – 98

Note: The data are summarized from Table 2.1(atomic percent)[a], Figure 2.7[b], Figure 2.18[c], Table 2.2[d], Figure 2.10[e], Table 4.1(atomic percent)[f], Figure 4.3[g], Figure 4.12[h], Figure 4.9[i], and Figure 4.7[j].

A better understanding of how tuning a property influences material function and hazard will facilitate the practical utility of rational design. While rational design aims to enhance the functional performance of materials and eliminate or reduce the potential hazard, the ability to decouple function and hazard will depend on the desired outcomes. The GMs can be engineered for a desired application that may or may not leverage bioactivity. For example, electrochemical and biological activities of GMs can be inextricably linked, i.e., both are governed by the same property(ies) such as the electronic properties. This correlation can be leveraged for applications where both activities are desired, such as GM-based electrochemical biosensors for biomarker detection[264, 265] and electrochemical disinfection of pathogens.[266] However, for these reactive materials of which function is linked to hazard (toxicity), appropriate disposal strategies should be employed to prevent the toxicity to human health and the environment. The particular material property(ies) associated with toxicity should be elaborately controlled (e.g., surface deactivation of active O or N sites, saturation of the structural defects). In addition, for the applications where the biocompatibility is desired, such as microbial fuel cells,[267] GM-based electrodes can be configurated through surface chemistry manipulation and controlled alignment of graphene nanosheets to ensure biocompatibility to anaerobic microbes while still maintaining excellent extracellular electron transfer. Further, there is an opportunity to tailor function and hazard outcomes when a specific property associated with function does not contribute to hazard. For example, N-types doped in the graphene distinctly influence the electrochemical applications (ORR and OER) studied in this work. While the intimate link exists between ORR and oxidative-stress related bioactivities that are driven by graphitic-N, pyridinic-N acts as a contributing factor for OER but the sample with high pyridinic-N does not induce more oxidative stress, offering a path toward advancing performance in applications relying on OER without elevating bioactivity.

Taken together, the established property-function and property-hazard relationships constitute an important dataset necessary for the establishment of the rational design guideline of GMs, advancing their application potential through the development of benign and functional GM-derived products. The impact of this contribution is significant because it can reduce environmental health and safety uncertainties, which is expected to be beneficial by breaking through barriers to investment and expediting the pace for product diversification and large-scale commercialization.[19] Finally, the work contributes to enhanced understanding of underlying causative mechanisms of GM physicochemical properties relating to their electrochemical and biological activities, which will promote the development in energy conversion and storage, biosensor, and biomedical fields.

5.2 Research Recommendations

The work within this dissertation presents a holistic approach to establishing property-function and property-hazard relationships for GMs that will inform their rational design to maximize the functional efficacy and minimize the negative impact. It also serves as a foundation for future research opportunities that will provide additional resolution and contributions accelerating the realization of the promise of GMs.

5.2.1 Develop Approaches to Synthesize Graphene with Desired Chemical Compositions

While active oxygen groups of GO (carbonyl, epoxide, hydroxyl groups) and nitrogen types (graphitic-N, pyridinic-N) of NG are identified in this work to influence a specific electrochemical or biological activity, the next and important step that should be pursued is how to synthesize graphene with a desired chemical composition. There are very few studies[243, 256, 268] on the synthesis of graphene that accomplish introducing the desired oxygen groups or nitrogen types in a controllable manner. Reduced graphene oxide with a high concentration of carbonyl groups was prepared using H_3PO_4 and NaH_2PO_4 medium in a hydrothermal process concomitant with the reduction of graphene oxide, and demonstrated enhanced capacitance due to the carbonyl groups involvement in reversible pseudocapacitance.[268] Additionally, nitrogen-doped graphene with a primary graphitic-N or pyridinic-N content was fabricated by a CVD technique through pyrolysis of hydrogen and methane[243] or hydrogen and ethylene[256] in the presence of ammonia on copper foils. However, the synthetic mechanism for this CVD process to produce a specific N-C bonding configuration in graphene is not understood. The ability to control chemical composition would realize rational design of graphene to maximize the desired performance and reduce the EHS risks. As such, more controllable and facile approaches to synthesize graphene are encouraged supporting through synthetic mechanisms.

5.2.2 Tune ORR Pathways and Product Selectivity

Oxygen (O_2) related reactions are of great importance in both electrochemical and biological activities. While many efforts have been made to develop electrocatalysts (e.g., heteroatom-doped graphene) that drive the four-electron ORR pathway that is desirable for fuel cells and metal-air batteries for maximizing energy conversion efficiency,[41-43] it is also important to focus on selective reduction of O_2 to hydrogen peroxide (H_2O_2) via a two-electron reaction given the wide use of H_2O_2 in various applications such as water treatment,[269] surface disinfection,[270] and environmental remediation.[271] The most widely used process to produce H_2O_2 is the anthraquinone oxidation, however, this approach suffers from high energy demand, capital cost, and transport and handling of highly concentrated H_2O_2.[272, 273] Conversely, electrochemical synthesis of H_2O_2 through a two-electron reduction of O_2 is a greener and safer route, and has recently attracted researchers' interests.[271, 273-275] Carbon nanomaterials serve as alternatives to platinum group-metals and have shown great promise for electrochemical synthesis of H_2O_2.[271] While pure carbon electrodes have low intrinsic activity for H_2O_2 production, additional treatments by functionalizing carbon with heteroatoms enhances the activity of carbon catalysts.[271, 273] While the electronic effects of catalysts on the binding strength between the catalytic site and O species are the origin of catalytic activity and selectivity for H_2O_2 production, there remain opportunities to develop carbon-based catalysts with tunability in electronic structures through chemical composition manipulation, which are necessary for systematic control of ORR pathways as well as the catalytic activity. In addition to informing paths towards enhanced control of electrochemical pathways, the correlation between ORR and oxidative-stress related bioactivity identified in this dissertation reveals a further opportunity to leverage these established reaction mechanisms to advance the predictive capability of mechanisms that underly GM oxidative-stress related bioactivity.

5.2.3 Explore the Influence of Graphene Electronic Properties on Biological Electron Transport Chains

In this dissertation, electron transfer characteristics of graphene (e.g., electrical conductivity, electron-donating graphitic-N) are identified to perturb biological redox pathways (i.e., glutathione oxidation) that induce oxidative stress and an adverse biological response. The energy that fuels various cellular processes in living cells (e.g., adenosine triphosphate, ATP) is derived from redox reactions in which electrons are shuttled from a series of electron transporters in the mitochondrion, referred to as the electron transport chain.[102] If nanomaterials with excellent electron transfer capacity (e.g., graphene and other 2D nanomaterials) are taken up by cells, they are likely to interfere with these critical reactions (e.g., mitochondrial electron transport chain), leading to changes in ATP production, damage of cell mitochondria, and apoptosis. Thus, a better understanding of how the electronic properties of nanomaterials interact with biological electron transport chains will uncover the underlying cytotoxicity mechanism, the knowledge of which informs advancement of applications where an intended cytotoxicity is induced to target specific cells (e.g., cancer cells) such as anti-cancer nanotheranostics or drug resistant bacteria, as well as evaluates safety of nanomaterials for biomedical applications.

5.2.4 Coupled Experimental-Computational Approach to Unveil Nano-Bio Interface Mechanisms

The experimental-computational approach employed in Chapter 3 is transferable to observe the interactions and unveil the underlying mechanisms between nanomaterials and other important cellular components (e.g., lipids, proteins, generic biomolecules) with atomic-level detail. For example, the bacterial cell is composed of proteins, polysaccharides, phospholipids, and nucleic acids, each of which is formed by subunits such as amino acids, sugars, fatty acids, and nucleotides in a specific sequence. The cell wall or cell membrane (depending on the type of bacteria) is most likely the first place of interaction with nanomaterials, thus, any event that interferes with their main components (e.g., phospholipid and peptidoglycan protein) will cause bacterial death. An investigation of the interactions between active sites of nanomaterials (e.g., functional groups, dopants) and functional groups of representative amino acids (e.g., the nitrogen group) for peptidoglycan proteins and fatty acids (e.g., the methylene group) for phospholipids, will provide deeper insight into the mechanisms of interaction. Such information can be used to inform rational design of nanomaterials for targeted antibacterial action and enhanced detection of target bacterial analytes.

In addition to the approach outlined in Chapter 3, additional experimental approaches will enhance the resolution and range of information attained through these investigations. Changes in surface chemistry before and after interacting with cellular components can be characterized using X-ray photoelectron spectroscopy (XPS)[261] and X-ray absorption near edge structure (XANES)[66] and the nano-bio binding affinity can be measured using surface plasmon resonance system.[276] For the computational approach, density functional theory[261] and molecular dynamics[86, 276, 277] enable simulation of interactions at the scale of interest. The resolution of the underlying interaction mechanisms at the nano-bio interface will enable a better understanding of the toxic effects of nanomaterials and further development of safe nanomaterials for biomedical applications.

Bibliography

1. Anastas, P.; Eghbali, N., Green chemistry: principles and practice. *Chem. Soc. Rev.* **2010,** *39* (1), 301-312.

2. Kostal, J.; Voutchkova-Kostal, A.; Anastas, P. T.; Zimmerman, J. B., Identifying and designing chemicals with minimal acute aquatic toxicity. *Proc. Natl. Acad. Sci. U. S. A.* **2015,** *112* (20), 6289-6294.

3. Hutchison, J. E., Greener nanoscience: a proactive approach to advancing applications and reducing implications of nanotechnology. *ACS Nano* **2008,** *2* (3), 395-402.

4. Dahl, J. A.; Maddux, B. L.; Hutchison, J. E., Toward greener nanosynthesis. *Chem. Rev.* **2007,** *107* (6), 2228-2269.

5. Gilbertson, L. M.; Zimmerman, J. B.; Plata, D. L.; Hutchison, J. E.; Anastas, P. T., Designing nanomaterials to maximize performance and minimize undesirable implications guided by the principles of green chemistry. *Chem. Soc. Rev.* **2015,** *44* (16), 5758-5777.

6. Falinski, M. M.; Plata, D. L.; Chopra, S. S.; Theis, T. L.; Gilbertson, L. M.; Zimmerman, J. B., A framework for sustainable nanomaterial selection and design based on performance, hazard, and economic considerations. *Nat. Nanotechnol.* **2018,** *13* (8), 708.

7. Li, R.; Zhang, L.; Wang, P., Rational design of nanomaterials for water treatment. *Nanoscale* **2015,** *7* (41), 17167-17194.

8. Kreyling, W. G.; Semmler-Behnke, M.; Chaudhry, Q., A complementary definition of nanomaterial. *Nano Today* **2010,** *5* (3), 165-168.

9. Roco, M. C.; Bainbridge, W. S., *Nanotechnology: societal implications: maximizing benefits for humanity*. Springer Dordrecht, The Netherlands: 2007.

10. Lai, R. W.; Yeung, K. W.; Yung, M. M.; Djurišić, A. B.; Giesy, J. P.; Leung, K. M., Regulation of engineered nanomaterials: current challenges, insights and future directions. *Environ. Sci. Pollut. Res.* **2018,** *25* (4), 3060-3077.

11. Jariwala, D.; Sangwan, V. K.; Lauhon, L. J.; Marks, T. J.; Hersam, M. C., Carbon nanomaterials for electronics, optoelectronics, photovoltaics, and sensing. *Chem. Soc. Rev.* **2013,** *42* (7), 2824-2860.

12. Hou, J.; Shao, Y.; Ellis, M. W.; Moore, R. B.; Yi, B., Graphene-based electrochemical energy conversion and storage: fuel cells, supercapacitors and lithium ion batteries. *Physical chemistry chemical physics : PCCP* **2011,** *13* (34), 15384-402.

13. Zheng, H.; Ma, R.; Gao, M.; Tian, X.; Li, Y.-Q.; Zeng, L.; Li, R., Antibacterial applications of graphene oxides: structure-activity relationships, molecular initiating events and biosafety. *Sci. Bull.* **2017**.

14. Reina, G.; González-Domínguez, J. M.; Criado, A.; Vázquez, E.; Bianco, A.; Prato, M., Promises, facts and challenges for graphene in biomedical applications. *Chem. Soc. Rev.* **2017,** *46* (15), 4400-4416.

15. Hu, C.; Dai, L., Carbon‐based metal‐free catalysts for electrocatalysis beyond the ORR. *Angew. Chem., Int. Ed.* **2016,** *55* (39), 11736-11758.

16. Kong, W.; Kum, H.; Bae, S.-H.; Shim, J.; Kim, H.; Kong, L.; Meng, Y.; Wang, K.; Kim, C.; Kim, J., Path towards graphene commercialization from lab to market. *Nat. Nanotechnol.* **2019,** *14* (10), 927-938.

17. Hu, X.; Zhou, Q., Health and ecosystem risks of graphene. *Chem. Rev.* **2013,** *113* (5), 3815-3835.

18. Seabra, A. B.; Paula, A. J.; de Lima, R.; Alves, O. L.; Durán, N., Nanotoxicity of graphene and graphene oxide. *Chem. Res. Toxicol.* **2014,** *27* (2), 159-168.

19. Wang, Z.; Zhu, W.; Qiu, Y.; Yi, X.; von dem Bussche, A.; Kane, A.; Gao, H.; Koski, K.; Hurt, R., Biological and environmental interactions of emerging two-dimensional nanomaterials. *Chem. Soc. Rev.* **2016,** *45* (6), 1750-1780.

20. Jastrzębska, A. M.; Kurtycz, P.; Olszyna, A. R., Recent advances in graphene family materials toxicity investigations. *J. Nanopart. Res.* **2012,** *14* (12), 1-21.

21. Gilbertson, L. M.; Goodwin Jr, D. G.; Taylor, A. D.; Pfefferle, L.; Zimmerman, J. B., Toward tailored functional design of multi-walled carbon nanotubes (MWNTs): electrochemical and antimicrobial activity enhancement via oxidation and selective reduction. *Environ. Sci. Technol.* **2014,** *48* (10), 5938-5945.

22. Pasquini, L. M.; Sekol, R. C.; Taylor, A. D.; Pfefferle, L. D.; Zimmerman, J. B., Realizing comparable oxidative and cytotoxic potential of single-and multiwalled carbon nanotubes through annealing. *Environ. Sci. Technol.* **2013,** *47* (15), 8775-8783.

23. Novoselov, K. S.; Geim, A. K.; Morozov, S. V.; Jiang, D.; Zhang, Y.; Dubonos, S. V.; Grigorieva, I. V.; Firsov, A. A., Electric field effect in atomically thin carbon films. *Science* **2004,** *306* (5696), 666-669.

24. Lee, C.; Wei, X.; Kysar, J. W.; Hone, J., Measurement of the elastic properties and intrinsic strength of monolayer graphene. *Science* **2008,** *321* (5887), 385-388.

25. Geim, A. K.; Novoselov, K. S., The rise of graphene. In *Nanoscience and Technology: A Collection of Reviews from Nature Journals*, World Scientific: 2010; pp 11-19.

26. Jing-Han, Y.; Wei-Wei, J.; Er-Qiang, L.; Tian-Song, P.; Yuan-Yuan, Z.; Hui, W., Fifth-nearest-neighbor tight-binding description of electronic structure of graphene. *Commun. Theor. Phys.* **2010,** *53* (6), 1172.

27. Petruk, O.; Szewczyk, R.; Ciuk, T.; Strupiński, W.; Salach, J.; Nowicki, M.; Pasternak, I.; Winiarski, W.; Trzcinka, K., Sensitivity and offset voltage testing in the hall-effect sensors made of graphene. In *Recent Advances in Automation, Robotics and Measuring Techniques,* Springer: 2014; pp 631-640.

28. Balandin, A. A.; Ghosh, S.; Bao, W.; Calizo, I.; Teweldebrhan, D.; Miao, F.; Lau, C. N., Superior thermal conductivity of single-layer graphene. *Nano Lett.* **2008,** *8* (3), 902-907.

29. Miranda, R.; de Parga, A. L. V., Graphene: Surfing ripples towards new devices. *Nat. Nanotechnol.* **2009,** *4* (9), 549.

30. Zhu, Y.; Murali, S.; Cai, W.; Li, X.; Suk, J. W.; Potts, J. R.; Ruoff, R. S., Graphene and graphene oxide: synthesis, properties, and applications. *Adv. Mater.* **2010,** *22* (35), 3906-3924.

31. Papageorgiou, D. G.; Kinloch, I. A.; Young, R. J., Mechanical properties of graphene and graphene-based nanocomposites. *Prog. Mater. Sci.* **2017,** *90*, 75-127.

32. Reiss, T.; Hjelt, K.; Ferrari, A., Graphene is on track to deliver on its promises. *Nat. Nanotechnol.* **2019,** *14* (10), 907-910.

33. Whitener, K. E.; Sheehan, P. E., Graphene synthesis. *Diamond Relat. Mater.* **2014,** *46*, 25-34.

34. De Jesus, L. R.; Dennis, R. V.; Depner, S. W.; Jaye, C.; Fischer, D. A.; Banerjee, S., Inside and outside: X-ray absorption spectroscopy mapping of chemical domains in graphene oxide. *J. Phys. Chem. Lett.* **2013,** *4* (18), 3144-3151.

35. Ganguly, A.; Sharma, S.; Papakonstantinou, P.; Hamilton, J., Probing the thermal deoxygenation of graphene oxide using high-resolution in situ X-ray-based spectroscopies. *J. Phys. Chem. C* **2011,** *115* (34), 17009-17019.

36. Pei, S.; Cheng, H.-M., The reduction of graphene oxide. *Carbon* **2012,** *50* (9), 3210-3228.

37. Chng, E. L. K.; Pumera, M., The toxicity of graphene oxides: dependence on the oxidative methods used. *Chem. Eur. J.* **2013,** *19* (25), 8227-8235.

38. Yuan, B.; Zeng, X.; Xu, C.; Liu, L.; Ma, Y.; Zhang, D.; Fan, Y., Electrochemical modification of graphene oxide bearing different types of oxygen functional species for the electro-catalytic oxidation of reduced glutathione. *Sens. Actuators, B* **2013,** *184*, 15-20.

39. Holloway, A. F.; Wildgoose, G. G.; Compton, R. G.; Shao, L.; Green, M. L., The influence of edge-plane defects and oxygen-containing surface groups on the voltammetry of acid-

treated, annealed and “super-annealed” multiwalled carbon nanotubes. *J. Solid State Electrochem.* **2008,** *12* (10), 1337-1348.

40. Tammeveski, K.; Kontturi, K.; Nichols, R. J.; Potter, R. J.; Schiffrin, D. J., Surface redox catalysis for O2 reduction on quinone-modified glassy carbon electrodes. *J. Electroanal. Chem.* **2001,** *515* (1), 101-112.

41. Wang, H.; Maiyalagan, T.; Wang, X., Review on recent progress in nitrogen-doped graphene: synthesis, characterization, and its potential applications. *ACS Catal.* **2012,** *2* (5), 781-794.

42. Duan, J.; Chen, S.; Jaroniec, M.; Qiao, S. Z., Heteroatom-doped graphene-based materials for energy-relevant electrocatalytic processes. *ACS Catal.* **2015,** *5* (9), 5207-5234.

43. Wang, X.; Sun, G.; Routh, P.; Kim, D.-H.; Huang, W.; Chen, P., Heteroatom-doped graphene materials: syntheses, properties and applications. *Chem. Soc. Rev.* **2014,** *43* (20), 7067-7098.

44. Liu, X.; Dai, L., Carbon-based metal-free catalysts. *Nat. Rev. Mater.* **2016,** *1* (11), 16064.

45. Brownson, D. A. C.; Banks, C. E., Graphene electrochemistry: an overview of potential applications. *The Analyst* **2010,** *135* (11), 2768-2778.

46. Brownson, D. A. C.; Kampouris, D. K.; Banks, C. E., Graphene electrochemistry: fundamental concepts through to prominent applications. *Chem. Soc. Rev.* **2012,** *41* (21), 6944-6976.

47. Pumera, M., Graphene-based nanomaterials and their electrochemistry. *Chem. Soc. Rev.* **2010,** *39* (11), 4146-4157.

48. Chen, D.; Feng, H.; Li, J., Graphene oxide: preparation, functionalization, and electrochemical applications. *Chem. Rev.* **2012,** *112* (11), 6027-6053.

49. McWilliams, A., The maturing nanotechnology market: products and applications. *BCC Research, NAN031G* **2016**.

50. Jiao, Y.; Zheng, Y.; Jaroniec, M.; Qiao, S. Z., Design of electrocatalysts for oxygen- and hydrogen-involving energy conversion reactions. *Chem. Soc. Rev.* **2015,** *44* (8), 2060-2086.

51. Ge, X.; Sumboja, A.; Wuu, D.; An, T.; Li, B.; Goh, F. T.; Hor, T. A.; Zong, Y.; Liu, Z., Oxygen reduction in alkaline media: from mechanisms to recent advances of catalysts. *ACS Catal.* **2015,** *5* (8), 4643-4667.

52. Hu, C.; Zhang, L.; Gong, J., Recent progress made in the mechanism comprehension and design of electrocatalysts for alkaline water splitting. *Energy Environ. Sci.* **2019,** *12* (9), 2620-2645.

53. Bard, A. J.; Faulkner, L. R., Methods involving forced convection-hydrodynamic methods. In *Electrochemical Methods: Fundamentals and Applications*, 2nd ed.; Wiley: New York, 2001; pp 331-364.

54. Yang, K.; Li, Y.; Tan, X.; Peng, R.; Liu, Z., Behavior and toxicity of graphene and its functionalized derivatives in biological systems. *Small* **2013,** *9* (9-10), 1492-1503.

55. Zou, X.; Zhang, L.; Wang, Z.; Luo, Y., Mechanisms of the antimicrobial activities of graphene materials. *J. Am. Chem. Soc.* **2016,** *138* (7), 2064-2077.

56. Huang, G. G.; Han, X. X.; Hossain, M. K.; Ozaki, Y., Development of a heat-induced surface-enhanced Raman scattering sensing method for rapid detection of glutathione in aqueous solutions. *Anal. Chem.* **2009,** *81* (14), 5881-5888.

57. Schafer, F. Q.; Buettner, G. R., Redox environment of the cell as viewed through the redox state of the glutathione disulfide/glutathione couple. *Free Radicals Biol. Med.* **2001,** *30* (11), 1191-1212.

58. Perreault, F.; de Faria, A. F.; Nejati, S.; Elimelech, M., Antimicrobial properties of graphene oxide nanosheets: why size matters. *ACS Nano* **2015,** *9* (7), 7226-7236.

59. Liu, S.; Zeng, T. H.; Hofmann, M.; Burcombe, E.; Wei, J.; Jiang, R.; Kong, J.; Chen, Y., Antibacterial activity of graphite, graphite oxide, graphene oxide, and reduced graphene oxide: membrane and oxidative stress. *ACS Nano* **2011,** *5* (9), 6971-6980.

60. Liu, X.; Sen, S.; Liu, J.; Kulaots, I.; Geohegan, D.; Kane, A.; Puretzky, A. A.; Rouleau, C. M.; More, K. L.; Palmore, G. T. R., Antioxidant deactivation on graphenic nanocarbon surfaces. *Small* **2011,** *7* (19), 2775-2785.

61. Holden, P. A.; Schimel, J. P.; Godwin, H. A., Five reasons to use bacteria when assessing manufactured nanomaterial environmental hazards and fates. *Curr. Opin. Biotechnol.* **2013,** *27*, 73-78.

62. Efremova, L. V.; Vasilchenko, A. S.; Rakov, E. G.; Deryabin, D. G., Toxicity of graphene shells, graphene oxide, and graphene oxide paper evaluated with Escherichia coli biotests. *BioMed Res. Int.* **2015,** *2015*, 10.

63. Akhavan, O.; Ghaderi, E., Toxicity of graphene and graphene oxide nanowalls against bacteria. *ACS Nano* **2010,** *4* (10), 5731-5736.

64. Akhavan, O.; Ghaderi, E.; Esfandiar, A., Wrapping bacteria by graphene nanosheets for isolation from environment, reactivation by sonication, and inactivation by near-infrared irradiation. *J. Phys. Chem. B* **2011,** *115* (19), 6279-6288.

65. Zhou, X.; Bai, Z.; Wu, M.; Qiao, J.; Chen, Z., 3-Dimensional porous N-doped graphene foam as a non-precious catalyst for the oxygen reduction reaction. *J. Mater. Chem. A* **2015,** *3* (7), 3343-3350.

66. Yang, H. B.; Miao, J.; Hung, S.-F.; Chen, J.; Tao, H. B.; Wang, X.; Zhang, L.; Chen, R.; Gao, J.; Chen, H. M., Identification of catalytic sites for oxygen reduction and oxygen evolution in n-doped graphene materials: development of highly efficient metal-free bifunctional electrocatalyst. *Sci. Adv.* **2016,** *2* (4), e1501122.

67. Li, Y.; Yang, J.; Zhao, N.; Huang, J.; Zhou, Y.; Xu, K.; Zhao, N., Facile fabrication of N-doped three-dimensional reduced graphene oxide as a superior electrocatalyst for oxygen reduction reaction. *Appl. Catal., A* **2017,** *534*, 30-39.

68. Lin, Z.; Waller, G. H.; Liu, Y.; Liu, M.; Wong, C.-p., 3D Nitrogen-doped graphene prepared by pyrolysis of graphene oxide with polypyrrole for electrocatalysis of oxygen reduction reaction. *Nano Energy* **2013,** *2* (2), 241-248.

69. Lin, Z.; Song, M.-k.; Ding, Y.; Liu, Y.; Liu, M.; Wong, C.-p., Facile preparation of nitrogen-doped graphene as a metal-free catalyst for oxygen reduction reaction. *Physical chemistry chemical physics : PCCP* **2012,** *14* (10), 3381-3387.

70. Gao, X.; Wang, L.; Ma, J.; Wang, Y.; Zhang, J., Facile preparation of nitrogen-doped graphene as an efficient oxygen reduction electrocatalyst. *Inorg. Chem. Front.* **2017,** *4* (9), 1582-1590.

71. Faisal, S. N.; Haque, E.; Noorbehesht, N.; Zhang, W.; Harris, A. T.; Church, Tamara L.; Minett, A. I., Pyridinic and graphitic nitrogen-rich graphene for high-performance supercapacitors and metal-free bifunctional electrocatalysts for ORR and OER. *RSC Adv.* **2017,** *7* (29), 17950-17958.

72. Soo, L. T.; Loh, K. S.; Mohamad, A. B.; Daud, W. R. W.; Wong, W. Y., Effect of nitrogen precursors on the electrochemical performance of nitrogen-doped reduced graphene oxide towards oxygen reduction reaction. *J. Alloys Compd.* **2016,** *677*, 112-120.

73. Miao, H.; Li, S.; Wang, Z.; Sun, S.; Kuang, M.; Liu, Z.; Yuan, J., Enhancing the pyridinic N content of nitrogen-doped graphene and improving its catalytic activity for oxygen reduction reaction. *Int. J. Hydrogen Energy* **2017,** *42* (47), 28298-28308.

74. Liu, Y.; Li, J.; Li, W.; Li, Y.; Zhan, F.; Tang, H.; Chen, Q., Exploring the nitrogen species of nitrogen doped graphene as electrocatalysts for oxygen reduction reaction in al–air batteries. *Int. J. Hydrogen Energy* **2016,** *41* (24), 10354-10365.

75. Xing, T.; Zheng, Y.; Li, L. H.; Cowie, B. C.; Gunzelmann, D.; Qiao, S. Z.; Huang, S.; Chen, Y., Observation of active sites for oxygen reduction reaction on nitrogen-doped multilayer graphene. *ACS Nano* **2014,** *8* (7), 6856-6862.

76. Sun, J.; Wang, L.; Song, R.; Yanga, S., Enhancing pyridinic nitrogen level in graphene to promote electrocatalytic activity for oxygen reduction reaction. *Nanotechnology* **2016,** *27* (5), 055404.

77. Zhu, C.; Li, H.; Fu, S.; Du, D.; Lin, Y., Highly efficient nonprecious metal catalysts towards oxygen reduction reaction based on three-dimensional porous carbon nanostructures. *Chem. Soc. Rev.* **2016,** *45* (3), 517-531.

78. Zhou, R.; Zheng, Y.; Hulicova-Jurcakova, D.; Qiao, S. Z., Enhanced electrochemical catalytic activity by copper oxide grown on nitrogen-doped reduced graphene oxide. *J. Mater. Chem. A* **2013,** *1* (42), 13179-13185.

79. Liang, Y.; Li, Y.; Wang, H.; Zhou, J.; Wang, J.; Regier, T.; Dai, H., Co3O4 nanocrystals on graphene as a synergistic catalyst for oxygen reduction reaction. *Nat. Mater.* **2011,** *10* (10), 780-786.

80. Jiang, Z.-J.; Jiang, Z., Interaction induced high catalytic activities of CoO nanoparticles grown on nitrogen-doped hollow graphene microspheres for oxygen reduction and evolution reactions. *Sci. Rep.* **2016,** *6*, 27081.

81. Bagri, A.; Mattevi, C.; Acik, M.; Chabal, Y. J.; Chhowalla, M.; Shenoy, V. B., Structural evolution during the reduction of chemically derived graphene oxide. *Nat. Chem.* **2010,** *2* (7), 581-587.

82. Gómez-Navarro, C.; Meyer, J. C.; Sundaram, R. S.; Chuvilin, A.; Kurasch, S.; Burghard, M.; Kern, K.; Kaiser, U., Atomic structure of reduced graphene oxide. *Nano Lett.* **2010,** *10* (4), 1144-1148.

83. Liu, S.; Hu, M.; Zeng, T. H.; Wu, R.; Jiang, R.; Wei, J.; Wang, L.; Kong, J.; Chen, Y., Lateral dimension-dependent antibacterial activity of graphene oxide sheets. *Langmuir* **2012,** *28* (33), 12364-12372.

84. Li, R.; Mansukhani, N. D.; Guiney, L. M.; Ji, Z.; Zhao, Y.; Chang, C. H.; French, C. T.; Miller, J. F.; Hersam, M. C.; Nel, A. E., Identification and optimization of carbon radicals on hydrated graphene oxide for ubiquitous antibacterial coatings. *ACS Nano* **2016,** *10* (12), 10966-10980.

85. Wu, C.; Wang, C.; Zheng, J.; Luo, C.; Li, Y.; Guo, S.; Zhang, J., Vacuolization in cytoplasm and cell membrane permeability enhancement triggered by micrometer-sized graphene oxide. *ACS Nano* **2015,** *9* (8), 7913-7924.

86. Tu, Y.; Lv, M.; Xiu, P.; Huynh, T.; Zhang, M.; Castelli, M.; Liu, Z.; Huang, Q.; Fan, C.; Fang, H.; Zhou, R., Destructive extraction of phospholipids from Escherichia coli membranes by graphene nanosheets. *Nat. Nanotechnol.* **2013,** *8* (8), 594-601.

87. Chen, L.; Hu, P.; Zhang, L.; Huang, S.; Luo, L.; Huang, C., Toxicity of graphene oxide and multi-walled carbon nanotubes against human cells and zebrafish. *Sci. China Chem.* **2012,** *55* (10), 2209-2216.

88. Chang, Y.; Yang, S.-T.; Liu, J.-H.; Dong, E.; Wang, Y.; Cao, A.; Liu, Y.; Wang, H., In vitro toxicity evaluation of graphene oxide on A549 cells. *Toxicol. Lett.* **2011,** *200* (3), 201-210.

89. Perreault, F.; Fonseca de Faria, A.; Elimelech, M., Environmental applications of graphene-based nanomaterials. *Chem. Soc. Rev.* **2015,** *44* (16), 5861-5896.

90. Akhavan, O.; Ghaderi, E., Escherichia coli bacteria reduce graphene oxide to bactericidal graphene in a self-limiting manner. *Carbon* **2012,** *50* (5), 1853-1860.

91. Krishnamoorthy, K.; Veerapandian, M.; Zhang, L.-H.; Yun, K.; Kim, S. J., Antibacterial efficiency of graphene nanosheets against pathogenic bacteria via lipid peroxidation. *J. Phys. Chem. C* **2012,** *116* (32), 17280-17287.

92. Hui, L.; Piao, J.-G.; Auletta, J.; Hu, K.; Zhu, Y.; Meyer, T.; Liu, H.; Yang, L., Availability of the basal planes of graphene oxide determines whether it is antibacterial. *ACS Appl. Mater. Interfaces* **2014,** *6* (15), 13183-13190.

93. Mangadlao, J. D.; Santos, C. M.; áde Leon, A. C. C., On the antibacterial mechanism of graphene oxide (GO) Langmuir–Blodgett films. *Chem. Commun.* **2015,** *51* (14), 2886-2889.

94. Lu, X.; Feng, X.; Werber, J. R.; Chu, C.; Zucker, I.; Kim, J.-H.; Osuji, C. O.; Elimelech, M., Enhanced antibacterial activity through the controlled alignment of graphene oxide nanosheets. *Proc. Natl. Acad. Sci. U. S. A.* **2017,** *114* (46), E9793-E9801.

95. Yadav, N.; Dubey, A.; Shukla, S.; Saini, C. P.; Gupta, G.; Priyadarshini, R.; Lochab, B., Graphene oxide-coated surface: inhibition of bacterial biofilm formation due to specific surface–interface interactions. *ACS omega* **2017,** *2* (7), 3070-3082.

96. Pulingam, T.; Thong, K. L.; Ali, M. E.; Appaturi, J. N.; Dinshaw, I. J.; Ong, Z. Y.; Leo, B. F., Graphene oxide exhibits differential mechanistic action towards Gram-positive and Gram-negative bacteria. *Colloids Surf. B* **2019,** *181*, 6-15.

97. Pham, V. T.; Truong, V. K.; Quinn, M. D.; Notley, S. M.; Guo, Y.; Baulin, V. A.; Al Kobaisi, M.; Crawford, R. J.; Ivanova, E. P., Graphene induces formation of pores that kill spherical and rod-shaped bacteria. *ACS Nano* **2015,** *9* (8), 8458-8467.

98. Gao, Y.; Wu, J.; Ren, X.; Tan, X.; Hayat, T.; Alsaedi, A.; Cheng, C.; Chen, C., Impact of graphene oxide on the antibacterial activity of antibiotics against bacteria. *Environ. Sci.: Nano* **2017,** *4* (5), 1016-1024.

99. Sengupta, I.; Bhattacharya, P.; Talukdar, M.; Neogi, S.; Pal, S. K.; Chakraborty, S., Bactericidal effect of graphene oxide and reduced graphene oxide: Influence of shape of bacteria. *Colloids Interface Sci. Commun.* **2019,** *28*, 60-68.

100. Gurunathan, S.; Han, J. W.; Dayem, A. A.; Eppakayala, V.; Kim, J.-H., Oxidative stress-mediated antibacterial activity of graphene oxide and reduced graphene oxide in Pseudomonas aeruginosa. *Int. J. Nanomed.* **2012,** *7*, 5901–5914.

101. Chen, J.; Peng, H.; Wang, X.; Shao, F.; Yuan, Z.; Han, H., Graphene oxide exhibits broad-spectrum antimicrobial activity against bacterial phytopathogens and fungal conidia by intertwining and membrane perturbation. *Nanoscale* **2014,** *6* (3), 1879-1889.

102. Madigan, M. T., *Brock biology of microorganisms*. 13th ed.; Benjamin Cummings: San Francisco, 2012.

103. Anastas, P. T.; Kirchhoff, M. M., Origins, current status, and future challenges of green chemistry. *Acc. Chem. Res.* **2002,** *35* (9), 686-694.

104. Connors, K. A.; Voutchkova-Kostal, A. M.; Kostal, J.; Anastas, P.; Zimmerman, J. B.; Brooks, B. W., Reducing aquatic hazards of industrial chemicals: probabilistic assessment of sustainable molecular design guidelines. *Environ. Toxicol. Chem.* **2014,** *33* (8), 1894-1902.

105. Yang, W.; Ratinac, K. R.; Ringer, S. P.; Thordarson, P.; Gooding, J. J.; Braet, F., Carbon nanomaterials in biosensors: should you use nanotubes or graphene? *Angew. Chem., Int. Ed.* **2010,** *49* (12), 2114-2138.

106. Allen, M. J.; Tung, V. C.; Kaner, R. B., Honeycomb carbon: a review of graphene. *Chem. Rev.* **2010,** *110* (1), 132-145.

107. Shao, Y.; Wang, J.; Engelhard, M.; Wang, C.; Lin, Y., Facile and controllable electrochemical reduction of graphene oxide and its applications. *J. Mater. Chem.* **2010,** *20* (4), 743-748.

108. De Volder, M. F.; Tawfick, S. H.; Baughman, R. H.; Hart, A. J., Carbon nanotubes: present and future commercial applications. *Science* **2013,** *339* (6119), 535-539.

109. Zhao, X.; Liu, R., Recent progress and perspectives on the toxicity of carbon nanotubes at organism, organ, cell, and biomacromolecule levels. *Environ. Int.* **2012,** *40*, 244-255.

110. Liu, X. T.; Mu, X. Y.; Wu, X. L.; Meng, L. X.; Guan, W. B.; Ma, Y. Q.; Sun, H.; Wang, C. J.; Li, X. F., Toxicity of multi-walled carbon nanotubes, graphene oxide, and reduced graphene oxide to zebrafish embryos. *Biomed. Environ. Sci.* **2014,** *27* (9), 676-683.

111. Petersen, E. J.; Zhang, L.; Mattison, N. T.; O'Carroll, D. M.; Whelton, A. J.; Uddin, N.; Nguyen, T.; Huang, Q.; Henry, T. B.; Holbrook, R. D.; Chen, K. L., Potential release pathways, environmental fate, and ecological risks of carbon nanotubes. *Environ. Sci. Technol.* **2011,** *45* (23), 9837-9856.

112. Wang, J.; Yang, S.; Guo, D.; Yu, P.; Li, D.; Ye, J.; Mao, L., Comparative studies on electrochemical activity of graphene nanosheets and carbon nanotubes. *Electrochem. Commun.* **2009,** *11* (10), 1892-1895.

113. Kurantowicz, N.; Sawosz, E.; Jaworski, S.; Kutwin, M.; Strojny, B.; Wierzbicki, M.; Szeliga, J.; Hotowy, A.; Lipińska, L.; Koziński, R., Interaction of graphene family

materials with Listeria monocytogenes and Salmonella enterica. *Nanoscale Res. Lett.* **2015,** *10* (1), 1-12.

114. Neto, A. C.; Guinea, F.; Peres, N. M.; Novoselov, K. S.; Geim, A. K., The electronic properties of graphene. *Rev. Mod. Phys.* **2009,** *81* (1), 109.

115. Loh, K. P.; Bao, Q.; Eda, G.; Chhowalla, M., Graphene oxide as a chemically tunable platform for optical applications. *Nat. Chem.* **2010,** *2* (12), 1015-1024.

116. Kavinkumar, T.; Sastikumar, D.; Manivannan, S., Effect of functional groups on dielectric, optical gas sensing properties of graphene oxide and reduced graphene oxide at room temperature. *RSC Adv.* **2015,** *5* (14), 10816-10825.

117. Li, X.; Wang, H.; Robinson, J. T.; Sanchez, H.; Diankov, G.; Dai, H., Simultaneous nitrogen doping and reduction of graphene oxide. *J. Am. Chem. Soc.* **2009,** *131* (43), 15939-15944.

118. Gao, W.; Alemany, L. B.; Ci, L.; Ajayan, P. M., New insights into the structure and reduction of graphite oxide. *Nat. Chem.* **2009,** *1* (5), 403-408.

119. Shin, H. J.; Kim, K. K.; Benayad, A.; Yoon, S. M.; Park, H. K.; Jung, I. S.; Jin, M. H.; Jeong, H. K.; Kim, J. M.; Choi, J. Y., Efficient reduction of graphite oxide by sodium borohydride and its effect on electrical conductance. *Adv. Funct. Mater.* **2009,** *19* (12), 1987-1992.

120. Yang, L.; Jiang, S.; Zhao, Y.; Zhu, L.; Chen, S.; Wang, X.; Wu, Q.; Ma, J.; Ma, Y.; Hu, Z., Boron‐doped carbon nanotubes as metal‐free electrocatalysts for the oxygen reduction reaction. *Angew. Chem.* **2011,** *123* (31), 7270-7273.

121. Sheng, Z.-H.; Gao, H.-L.; Bao, W.-J.; Wang, F.-B.; Xia, X.-H., Synthesis of boron doped graphene for oxygen reduction reaction in fuel cells. *J. Mater. Chem.* **2012,** *22* (2), 390-395.

122. Tai, F.-C.; Lee, S.-C.; Chen, J.; Wei, C.; Chang, S.-H., Multipeak fitting analysis of Raman spectra on DLCH film. *J. Raman Spectrosc.* **2009,** *40* (8), 1055-1059.

123. Glover, A. J.; Cai, M.; Overdeep, K. R.; Kranbuehl, D. E.; Schniepp, H. C., In situ reduction of graphene oxide in polymers. *Macromolecules* **2011,** *44* (24), 9821-9829.

124. Vecitis, C. D.; Zodrow, K. R.; Kang, S.; Elimelech, M., Electronic-structure-dependent bacterial cytotoxicity of single-walled carbon nanotubes. *ACS Nano* **2010,** *4* (9), 5471-5479.

125. Lotya, M.; Hernandez, Y.; King, P. J.; Smith, R. J.; Nicolosi, V.; Karlsson, L. S.; Blighe, F. M.; De, S.; Wang, Z.; McGovern, I., Liquid phase production of graphene by exfoliation of graphite in surfactant/water solutions. *J. Am. Chem. Soc.* **2009,** *131* (10), 3611-3620.

126. Krishnamoorthy, K.; Veerapandian, M.; Yun, K.; Kim, S. J., The chemical and structural analysis of graphene oxide with different degrees of oxidation. *Carbon* **2013,** *53*, 38-49.

127. Ferrero, G. A.; Preuss, K.; Marinovic, A.; Jorge, A. B.; Mansor, N.; Brett, D. J. L.; Fuertes, A. B.; Sevilla, M.; Titirici, M.-M., Fe–N-doped carbon capsules with outstanding electrochemical performance and stability for the oxygen reduction reaction in both acid and alkaline conditions. *ACS Nano* **2016,** *10* (6), 5922-5932.

128. Zhou, R.; Zheng, Y.; Jaroniec, M.; Qiao, S.-Z., Determination of the electron transfer number for the oxygen reduction reaction: from theory to experiment. *ACS Catal.* **2016,** *6* (7), 4720-4728.

129. Chen, Z.; Higgins, D.; Chen, Z., Nitrogen doped carbon nanotubes and their impact on the oxygen reduction reaction in fuel cells. *Carbon* **2010,** *48* (11), 3057-3065.

130. Kruusenberg, I.; Alexeyeva, N.; Tammeveski, K., The pH-dependence of oxygen reduction on multi-walled carbon nanotube modified glassy carbon electrodes. *Carbon* **2009,** *47* (3), 651-658.

131. Benson, J.; Xu, Q.; Wang, P.; Shen, Y.; Sun, L.; Wang, T.; Li, M.; Papakonstantinou, P., Tuning the catalytic activity of graphene nanosheets for oxygen reduction reaction via size and thickness reduction. *ACS Appl. Mater. Interfaces* **2014,** *6* (22), 19726-19736.

132. Guo, C. X.; Lei, Y.; Li, C. M., Porphyrin functionalized graphene for sensitive electrochemical detection of ultratrace explosives. *Electroanalysis* **2011,** *23* (4), 885-893.

133. Guo, C.; Hu, F.; Li, C. M.; Shen, P. K., Direct electrochemistry of hemoglobin on carbonized titania nanotubes and its application in a sensitive reagentless hydrogen peroxide biosensor. *Biosens. Bioelectron.* **2008,** *24* (4), 819-824.

134. Eda, G.; Fanchini, G.; Chhowalla, M., Large-area ultrathin films of reduced graphene oxide as a transparent and flexible electronic material. *Nat. Nanotechnol.* **2008,** *3* (5), 270-274.

135. Becerril, H. A.; Mao, J.; Liu, Z.; Stoltenberg, R. M.; Bao, Z.; Chen, Y., Evaluation of solution-processed reduced graphene oxide films as transparent conductors. *ACS Nano* **2008,** *2* (3), 463-470.

136. Stankovich, S.; Dikin, D. A.; Piner, R. D.; Kohlhaas, K. A.; Kleinhammes, A.; Jia, Y.; Wu, Y.; Nguyen, S. T.; Ruoff, R. S., Synthesis of graphene-based nanosheets via chemical reduction of exfoliated graphite oxide. *Carbon* **2007,** *45* (7), 1558-1565.

137. Antolini, E., Graphene as a new carbon support for low-temperature fuel cell catalysts. *Appl. Catal., B* **2012,** *123*, 52-68.

138. Some, S.; Kim, Y.; Yoon, Y.; Yoo, H.; Lee, S.; Park, Y.; Lee, H., High-quality reduced graphene oxide by a dual-function chemical reduction and healing process. *Sci. Rep.* **2013,** *3*, 1929.

139. Paredes, J. I.; Villar-Rodil, S.; Martínez-Alonso, A.; Tascón, J. M. D., Graphene oxide dispersions in organic solvents. *Langmuir* **2008,** *24* (19), 10560-10564.

140. Lee, D.; Seo, J., Sp2/sp3 carbon ratio in graphite oxide with different preparation times. *J. Phys. Chem. C* **2011,** *115* (6), 2705-2708.

141. Mattevi, C.; Eda, G.; Agnoli, S.; Miller, S.; Mkhoyan, K. A.; Celik, O.; Mastrogiovanni, D.; Granozzi, G.; Garfunkel, E.; Chhowalla, M., Evolution of electrical, chemical, and structural properties of transparent and conducting chemically derived graphene thin films. *Adv. Funct. Mater.* **2009,** *19* (16), 2577-2583.

142. Yang, D.; Velamakanni, A.; Bozoklu, G.; Park, S.; Stoller, M.; Piner, R. D.; Stankovich, S.; Jung, I.; Field, D. A.; Ventrice Jr, C. A.; Ruoff, R. S., Chemical analysis of graphene oxide films after heat and chemical treatments by X-ray photoelectron and micro-Raman spectroscopy. *Carbon* **2009,** *47* (1), 145-152.

143. Hou, W.-C.; Chowdhury, I.; Goodwin Jr, D. G.; Henderson, W. M.; Fairbrother, D. H.; Bouchard, D.; Zepp, R. G., Photochemical transformation of graphene oxide in sunlight. *Environ. Sci. Technol.* **2015,** *49* (6), 3435-3443.

144. Robertson, J.; O'Reilly, E. P., Electronic and atomic structure of amorphous carbon. *Phys. Rev. B* **1987,** *35* (6), 2946-2957.

145. Jiang, Y.; Raliya, R.; Fortner, J. D.; Biswas, P., Graphene oxides in water: correlating morphology and surface chemistry with aggregation behavior. *Environ. Sci. Technol.* **2016,** *50* (13), 6964-6973.

146. Rozada, R.; Paredes, J. I.; Villar-Rodil, S.; Martínez-Alonso, A.; Tascón, J. M., Towards full repair of defects in reduced graphene oxide films by two-step graphitization. *Nano Res.* **2013,** *6* (3), 216-233.

147. Acik, M.; Lee, G.; Mattevi, C.; Pirkle, A.; Wallace, R. M.; Chhowalla, M.; Cho, K.; Chabal, Y., The role of oxygen during thermal reduction of graphene oxide studied by infrared absorption spectroscopy. *J. Phys. Chem. C* **2011,** *115* (40), 19761-19781.

148. Fernandez-Merino, M.; Guardia, L.; Paredes, J.; Villar-Rodil, S.; Solis-Fernandez, P.; Martinez-Alonso, A.; Tascon, J., Vitamin C is an ideal substitute for hydrazine in the reduction of graphene oxide suspensions. *J. Phys. Chem. C* **2010,** *114* (14), 6426-6432.

149. Mathkar, A.; Tozier, D.; Cox, P.; Ong, P.; Galande, C.; Balakrishnan, K.; Leela Mohana Reddy, A.; Ajayan, P. M., Controlled, stepwise reduction and band gap manipulation of graphene oxide. *J. Phys. Chem. Lett.* **2012,** *3* (8), 986-991.

150. Li, J.; Xiao, G.; Chen, C.; Li, R.; Yan, D., Superior dispersions of reduced graphene oxide synthesized by using gallic acid as a reductant and stabilizer. *J. Mater. Chem. A* **2013,** *1* (4), 1481-1487.

151. Beams, R.; Cançado, L. G.; Novotny, L., Raman characterization of defects and dopants in graphene. *J. Phys.: Condens. Matter* **2015,** *27* (8), 083002.

152. Singh, M.; Yadav, A.; Kumar, S.; Agarwal, P., Annealing induced electrical conduction and band gap variation in thermally reduced graphene oxide films with different sp 2/sp 3 fraction. *Appl. Surf. Sci.* **2015,** *326*, 236-242.

153. Kaniyoor, A.; Ramaprabhu, S., A Raman spectroscopic investigation of graphite oxide derived graphene. *AIP Adv.* **2012,** *2* (3), 032183.

154. Ferrari, A. C.; Robertson, J., Interpretation of Raman spectra of disordered and amorphous carbon. *Phys. Rev. B* **2000,** *61* (20), 14095.

155. Claramunt, S.; Varea, A.; López-Díaz, D.; Velázquez, M. M.; Cornet, A.; Cirera, A., The importance of interbands on the interpretation of the Raman spectrum of graphene oxide. *J. Phys. Chem. C* **2015,** *119* (18), 10123-10129.

156. Eigler, S.; Dotzer, C.; Hirsch, A., Visualization of defect densities in reduced graphene oxide. *Carbon* **2012,** *50* (10), 3666-3673.

157. Cançado, L. G.; Jorio, A.; Ferreira, E. M.; Stavale, F.; Achete, C.; Capaz, R.; Moutinho, M.; Lombardo, A.; Kulmala, T.; Ferrari, A., Quantifying defects in graphene via Raman spectroscopy at different excitation energies. *Nano Lett.* **2011,** *11* (8), 3190-3196.

158. Phan, D.-T.; Chung, G.-S., Effects of oxygen-functional groups on humidity sensor based graphene oxide thin films. In *Sensors, 2012 IEEE*, IEEE: 2012; pp 1-4.

159. Bo, Z.; Shuai, X.; Mao, S.; Yang, H.; Qian, J.; Chen, J.; Yan, J.; Cen, K., Green preparation of reduced graphene oxide for sensing and energy storage applications. *Sci. Rep.* **2014,** *4*, 4684.

160. Lucchese, M. M.; Stavale, F.; Ferreira, E. M.; Vilani, C.; Moutinho, M.; Capaz, R. B.; Achete, C.; Jorio, A., Quantifying ion-induced defects and Raman relaxation length in graphene. *Carbon* **2010,** *48* (5), 1592-1597.

161. Jung, I.; Dikin, D. A.; Piner, R. D.; Ruoff, R. S., Tunable electrical conductivity of individual graphene oxide sheets reduced at “low” temperatures. *Nano Lett.* **2008,** *8* (12), 4283-4287.

162. Dreyer, D. R.; Park, S.; Bielawski, C. W.; Ruoff, R. S., The chemistry of graphene oxide. *Chem. Soc. Rev.* **2010,** *39* (1), 228-240.

163. Wu, W.; Yu, Q.; Peng, P.; Liu, Z.; Bao, J.; Pei, S.-S., Control of thickness uniformity and grain size in graphene films for transparent conductive electrodes. *Nanotechnology* **2011,** *23* (3), 035603.

164. Červenka, J.; Flipse, C., Structural and electronic properties of grain boundaries in graphite: planes of periodically distributed point defects. *Phys. Rev. B* **2009,** *79* (19), 195429.

165. Hu, C.; Wang, Q.; Zhao, H.; Wang, L.; Guo, S.; Li, X., Ecotoxicological effects of graphene oxide on the protozoan Euglena gracilis. *Chemosphere* **2015,** *128,* 184-190.

166. Gilbertson, L. M.; Albalghiti, E. M.; Fishman, Z. S.; Perreault, F.; Corredor, C.; Posner, J. D.; Elimelech, M.; Pfefferle, L. D.; Zimmerman, J. B., Shape-dependent surface reactivity and antimicrobial activity of nano-cupric oxide. *Environ. Sci. Technol.* **2016,** *50* (7), 3975-3984.

167. Thomas, H. R.; Marsden, A. J.; Walker, M.; Wilson, N. R.; Rourke, J. P., Sulfur‐functionalized graphene oxide by epoxide ring‐opening. *Angew. Chem., Int. Ed.* **2014,** *53* (29), 7613-7618.

168. Shao, Y.; Liu, J.; Wang, Y.; Lin, Y., Novel catalyst support materials for PEM fuel cells: current status and future prospects. *J. Mater. Chem.* **2008,** *19* (1), 46-59.

169. Song, C.; Zhang, J., Electrocatalytic oxygen reduction reaction. In *PEM fuel cell electrocatalysts and catalyst layers*, Springer: 2008; pp 89-134.

170. Tang, C.; Wang, H. F.; Chen, X.; Li, B. Q.; Hou, T. Z.; Zhang, B.; Zhang, Q.; Titirici, M. M.; Wei, F., Topological defects in metal‐free nanocarbon for oxygen electrocatalysis. *Adv. Mater.* **2016,** *28* (32), 6845-6851.

171. Tao, L.; Wang, Q.; Dou, S.; Ma, Z.; Huo, J.; Wang, S.; Dai, L., Edge-rich and dopant-free graphene as a highly efficient metal-free electrocatalyst for the oxygen reduction reaction. *Chem. Commun.* **2016,** *52* (13), 2764-2767.

172. Jiang, Y.; Yang, L.; Sun, T.; Zhao, J.; Lyu, Z.; Zhuo, O.; Wang, X.; Wu, Q.; Ma, J.; Hu, Z., Significant contribution of intrinsic carbon defects to oxygen reduction activity. *ACS Catal.* **2015,** *5* (11), 6707-6712.

173. Yuan, W.; Zhou, Y.; Li, Y.; Li, C.; Peng, H.; Zhang, J.; Liu, Z.; Dai, L.; Shi, G., The edge- and basal-plane-specific electrochemistry of a single-layer graphene sheet. *Sci. Rep.* **2013,** *3*, 2248.

174. Acik, M.; Chabal, Y. J., Nature of graphene edges: a review. *Jpn. J. Appl. Phys.* **2011,** *50* (7R), 070101.

175. Yang, Z.; Yao, Z.; Li, G.; Fang, G.; Nie, H.; Liu, Z.; Zhou, X.; Chen, X. a.; Huang, S., Sulfur-doped graphene as an efficient metal-free cathode catalyst for oxygen reduction. *ACS Nano* **2011,** *6* (1), 205-211.

176. Qu, L.; Liu, Y.; Baek, J.-B.; Dai, L., Nitrogen-doped graphene as efficient metal-free electrocatalyst for oxygen reduction in fuel cells. *ACS Nano* **2010,** *4* (3), 1321-1326.

177. Gong, K.; Du, F.; Xia, Z.; Durstock, M.; Dai, L., Nitrogen-doped carbon nanotube arrays with high electrocatalytic activity for oxygen reduction. *Science* **2009,** *323* (5915), 760-764.

178. Carrero-Sanchez, J.; Elias, A.; Mancilla, R.; Arrellin, G.; Terrones, H.; Laclette, J.; Terrones, M., Biocompatibility and toxicological studies of carbon nanotubes doped with nitrogen. *Nano Lett.* **2006,** *6* (8), 1609-1616.

179. Reina, G.; Ruiz, A.; Murera, D.; Nishina, Y.; Bianco, A., "Ultramixing": a simple and effective method to obtain controlled and stable dispersions of graphene oxide in cell culture media. *ACS Appl. Mater. Interfaces* **2019,** *11* (8), 7695-7702.

180. Rauti, R.; Medelin, M.; Newman, L.; Vranic, S.; Reina, G.; Bianco, A.; Prato, M.; Kostarelos, K.; Ballerini, L., Graphene oxide flakes tune excitatory neurotransmission in vivo by targeting hippocampal synapses. *Nano Lett.* **2019**.

181. Lee, J.; Kim, J.; Kim, S.; Min, D.-H., Biosensors based on graphene oxide and its biomedical application. *Adv. Drug Delivery Rev.* **2016,** *105*, 275-287.

182. Gilbertson, L. M.; Pourzahedic, L.; Laughtonc, S.; Gao, X.; Zimmermand, J. B.; Theise, T. L.; Westerhofff, P. K.; Lowry, G. V., Defining the design space for nanotechnology's role in advancing sustainable crop production (in revision). *Nat. Nanotechnol.* **2019**.

183. Giraldo, J. P.; Wu, H.; Newkirk, G. M.; Kruss, S., Nanobiotechnology approaches for engineering smart plant sensors. *Nat. Nanotechnol.* **2019,** *14* (6), 541-553.

184. Lowry, G. V.; Avellan, A.; Gilbertson, L. M., Opportunities and challenges for nanotechnology in the agri-tech revolution. *Nat. Nanotechnol.* **2019,** *14* (6), 517-522.

185. Sanchez, V. C.; Jachak, A.; Hurt, R. H.; Kane, A. B., Biological interactions of graphene-family nanomaterials: an interdisciplinary review. *Chem. Res. Toxicol.* **2012,** *25* (1), 15-34.

186. Geim, A. K., Graphene: Status and Prospects. *Science* **2009,** *324* (5934), 1530-1534.

187. Wang, Y.; Gilbertson, L. M., Informing rational design of graphene oxide through surface chemistry manipulations: properties governing electrochemical and biological activities. *Green Chem.* **2017,** *19* (12), 2826-2838.

188. Wang, K.; Ruan, J.; Song, H.; Zhang, J.; Wo, Y.; Guo, S.; Cui, D., Biocompatibility of graphene oxide. *Nanoscale Res. Lett.* **2010,** *6* (1), 8.

189. Liao, K.-H.; Lin, Y.-S.; Macosko, C. W.; Haynes, C. L., Cytotoxicity of graphene oxide and graphene in human erythrocytes and skin fibroblasts. *ACS Appl. Mater. Interfaces* **2011,** *3* (7), 2607-2615.

190. Lu, C. H.; Yang, H. H.; Zhu, C. L.; Chen, X.; Chen, G. N., A graphene platform for sensing biomolecules. *Angew. Chem. Int. Ed. Engl.* **2009,** *48* (26), 4785-4787.

191. Chou, S. S.; De, M.; Luo, J.; Rotello, V. M.; Huang, J.; Dravid, V. P., Nanoscale graphene oxide (nGO) as artificial receptors: implications for biomolecular interactions and sensing. *J. Am. Chem. Soc.* **2012,** *134* (40), 16725-16733.

192. Safdari, F.; Raissi, H.; Shahabi, M.; Zaboli, M., DFT calculations and molecular dynamics simulation study on the adsorption of 5-fluorouracil anticancer drug on graphene oxide nanosheet as a drug delivery vehicle. *J. Inorg. Organomet. Polym. Mater.* **2017,** *27* (3), 805-817.

193. Cen, W.; Hou, M.; Liu, J.; Yuan, S.; Liu, Y.; Chu, Y., Oxidation of SO2 and NO by epoxy groups on graphene oxides: the role of the hydroxyl group. *RSC Adv.* **2015,** *5* (29), 22802-22810.

194. Keith, J. A.; Muñoz-García, A. B.; Lessio, M.; Carter, E. A., Cluster models for studying CO2 reduction on semiconductor photoelectrodes. *Top. Catal.* **2015,** *58* (1), 46-56.

195. Boukhvalov, D. W.; Dreyer, D. R.; Bielawski, C. W.; Son, Y. W., A computational investigation of the catalytic properties of graphene oxide: Exploring mechanisms by using DFT methods. *ChemCatChem* **2012,** *4* (11), 1844-1849.

196. Chen, C.; Kong, W.; Duan, H.-M.; Zhang, J., Theoretical simulation of reduction mechanism of graphene oxide in sodium hydroxide solution. *Physical chemistry chemical physics : PCCP* **2014,** *16* (25), 12858-12864.

197. Guo, Y.-n.; Lu, X.; Weng, J.; Leng, Y., Density functional theory study of the interaction of arginine-glycine-aspartic acid with graphene, defective graphene, and graphene oxide. *J. Phys. Chem. C* **2013,** *117* (11), 5708-5717.

198. Noctor, G.; Mhamdi, A.; Chaouch, S.; Han, Y.; Neukermans, J.; Marquez‐Garcia, B.; Queval, G.; Foyer, C. H., Glutathione in plants: an integrated overview. *Plant, Cell Environ.* **2012,** *35* (2), 454-484.

199. Bannai, S.; Tateishi, N., Role of membrane transport in metabolism and function of glutathione in mammals. *J. Membr. Biol.* **1986,** *89* (1), 1-8.

200. García‐Castañeda, O.; Gaxiola‐Robles, R.; Kanatous, S.; Zenteno‐Savín, T., Circulating glutathione concentrations in marine, semiaquatic, and terrestrial mammals. *Mar. Mammal Sci.* **2017,** *33* (3), 738-747.

201. Hasanuzzaman, M.; Nahar, K.; Anee, T. I.; Fujita, M., Glutathione in plants: biosynthesis and physiological role in environmental stress tolerance. *Physiol. Mol. Biol. Plants* **2017,** *23* (2), 249-268.

202. Mirzahosseini, A.; Noszál, B., Species-specific standard redox potential of thiol-disulfide systems: a key parameter to develop agents against oxidative stress. *Sci. Rep.* **2016,** *6*, 37596.

203. Pham, T. A.; Kim, J. S.; Kim, J. S.; Jeong, Y. T., One-step reduction of graphene oxide with l-glutathione. *Colloids Surf. A* **2011,** *384* (1), 543-548.

204. Zheng, S.; Pfaendtner, J., Enhanced sampling of chemical and biochemical reactions with metadynamics. *Mol. Simul.* **2015,** *41* (1-3), 55-72.

205. Neese, F., The ORCA program system. *Wiley Interdiscip. Rev.: Comput. Mol. Sci.* **2012,** *2* (1), 73-78.

206. Perdew, J. P., Density-functional approximation for the correlation energy of the inhomogeneous electron gas. *Phys. Rev. B* **1986,** *33* (12), 8822.

207. Becke, A. D., Density-functional exchange-energy approximation with correct asymptotic behavior. *Phys. Rev. A* **1988,** *38* (6), 3098.

208. Grimme, S.; Ehrlich, S.; Goerigk, L., Effect of the damping function in dispersion corrected density functional theory. *J. Comput. Chem.* **2011,** *32* (7), 1456-1465.

209. Weigend, F.; Ahlrichs, R., Balanced basis sets of split valence, triple zeta valence and quadruple zeta valence quality for H to Rn: Design and assessment of accuracy. *Physical chemistry chemical physics : PCCP* **2005,** *7* (18), 3297-3305.

210. Chai, J.-D.; Head-Gordon, M., Long-range corrected hybrid density functionals with damped atom–atom dispersion corrections. *Physical chemistry chemical physics : PCCP* **2008,** *10* (44), 6615-6620.

211. Takano, Y.; Houk, K., Benchmarking the conductor-like polarizable continuum model (CPCM) for aqueous solvation free energies of neutral and ionic organic molecules. *J. Chem. Theory Comput.* **2005,** *1* (1), 70-77.

212. Zimmerman, P., Reliable transition state searches integrated with the growing string method. *J. Chem. Theory Comput.* **2013,** *9* (7), 3043-3050.

213. Zimmerman, P. M., Growing string method with interpolation and optimization in internal coordinates: Method and examples. *J. Chem. Phys.* **2013,** *138* (18), 184102.

214. Zimmerman, P. M., Single-ended transition state finding with the growing string method. *J. Comput. Chem.* **2015,** *36* (9), 601-611.

215. Heppner, D. E.; Janssen-Heininger, Y. M.; van der Vliet, A., The role of sulfenic acids in cellular redox signaling: reconciling chemical kinetics and molecular detection strategies. *Arch. Biochem. Biophys.* **2017,** *616*, 40-46.

216. Lim, J. C.; Choi, H.-I.; Park, Y. S.; Nam, H. W.; Woo, H. A.; Kwon, K.-S.; Kim, Y. S.; Rhee, S. G.; Kim, K.; Chae, H. Z., Irreversible oxidation of the active-site cysteine of peroxiredoxin to cysteine sulfonic acid for enhanced molecular chaperone activity. *J. Biol. Chem.* **2008,** *283* (43), 28873-28880.

217. Chou, H.-C.; Chan, H.-L., Effect of glutathione reductase knockdown in response to UVB-induced oxidative stress in human lung adenocarcinoma. *Proteome Sci.* **2014,** *12* (1), 2.

218. Al-Gaashani, R.; Najjar, A.; Zakaria, Y.; Mansour, S.; Atieh, M. A., XPS and structural studies of high quality graphene oxide and reduced graphene oxide prepared by different chemical oxidation methods. *Ceram. Int.* **2019,** *45* (11), 14439-14448.

219. Figueiredo, J. L.; Pereira, M.; Freitas, M.; Orfao, J., Modification of the surface chemistry of activated carbons. *Carbon* **1999,** *37* (9), 1379-1389.

220. Szymański, G. S.; Karpiński, Z.; Biniak, S.; Świątkowski, A., The effect of the gradual thermal decomposition of surface oxygen species on the chemical and catalytic properties of oxidized activated carbon. *Carbon* **2002,** *40* (14), 2627-2639.

221. Cottrell, T. L., *The strengths of chemical bonds*. Academic Press: 1958.

222. Darwent, B. d., National standard reference data series. In *Natl. Bur. Stand.*, 1970; Vol. 31, pp 15-22.

223. Basdogan, Y.; Keith, J. A., A paramedic treatment for modeling explicitly solvated chemical reaction mechanisms. *Chem. Sci.* **2018,** *9* (24), 5341-5346.

224. Plata, R. E.; Singleton, D. A., A case study of the mechanism of alcohol-mediated morita baylis–hillman reactions. The importance of experimental observations. *J. Am. Chem. Soc.* **2015,** *137* (11), 3811-3826.

225. Tian, X.; Zheng, H.; Mirsaidov, U., Aggregation dynamics of nanoparticles at solid–liquid interfaces. *Nanoscale* **2017,** *9* (28), 10044-10050.

226. Zhang, J.; Dai, L., Heteroatom-doped graphitic carbon catalysts for efficient electrocatalysis of oxygen reduction reaction. *ACS Catal.* **2015,** *5* (12), 7244-7253.

227. Liu, H.; Liu, Y.; Zhu, D., Chemical doping of graphene. *J. Mater. Chem.* **2011,** *21* (10), 3335-3345.

228. Zhang, L.; Xia, Z., Mechanisms of oxygen reduction reaction on nitrogen-doped graphene for fuel cells. *J. Phys. Chem. C* **2011,** *115* (22), 11170-11176.

229. Lai, L.; Potts, J. R.; Zhan, D.; Wang, L.; Poh, C. K.; Tang, C.; Gong, H.; Shen, Z.; Lin, J.; Ruoff, R. S., Exploration of the active center structure of nitrogen-doped graphene-based catalysts for oxygen reduction reaction. *Energy Environ. Sci.* **2012,** *5* (7), 7936-7942.

230. Kim, H. S.; Kim, H. S.; Kim, S. S.; Kim, Y.-H., Atomistic mechanisms of codoping-induced p-to n-type conversion in nitrogen-doped graphene. *Nanoscale* **2014,** *6* (24), 14911-14918.

231. Usachov, D.; Vilkov, O.; Gruneis, A.; Haberer, D.; Fedorov, A.; Adamchuk, V.; Preobrajenski, A.; Dudin, P.; Barinov, A.; Oehzelt, M., Nitrogen-doped graphene: efficient growth, structure, and electronic properties. *Nano Lett.* **2011,** *11* (12), 5401-5407.

232. Schiros, T.; Nordlund, D.; Pálová, L.; Prezzi, D.; Zhao, L.; Kim, K. S.; Wurstbauer, U.; Gutiérrez, C.; Delongchamp, D.; Jaye, C., Connecting dopant bond type with electronic structure in n-doped graphene. *Nano Lett.* **2012,** *12* (8), 4025-4031.

233. Lee, W. J.; Maiti, U. N.; Lee, J. M.; Lim, J.; Han, T. H.; Kim, S. O., Nitrogen-doped carbon nanotubes and graphene composite structures for energy and catalytic applications. *Chem. Commun.* **2014,** *50* (52), 6818-6830.

234. Fan, M.; Zhu, C.; Liu, L.; Wu, Q.; Hao, Q.; Yang, J.; Sun, D., Modified PEDOT by benign preparing N-doped reduced graphene oxide as potential bio-electrode coating material. *Green Chem.* **2016,** *18* (6), 1731-1737.

235. Guo, M.; Li, D.; Zhao, M.; Zhang, Y.; Geng, D.; Lushington, A.; Sun, X., Nitrogen ion implanted graphene as thrombo-protective safer and cytoprotective alternative for biomedical applications. *Carbon* **2013,** *61*, 321-328.

236. Boncel, S.; Müller, K. H.; Skepper, J. N.; Walczak, K. Z.; Koziol, K. K., Tunable chemistry and morphology of multi-wall carbon nanotubes as a route to non-toxic, theranostic systems. *Biomaterials* **2011,** *32* (30), 7677-7686.

237. Yang, Y.; Zhang, J.; Zhuang, J.; Wang, X., Synthesis of nitrogen-doped carbon nanostructures from polyurethane sponge for bioimaging and catalysis. *Nanoscale* **2015,** *7* (29), 12284-12290.

238. Zhao, M.; Cao, Y.; Liu, X.; Deng, J.; Li, D.; Gu, H., Effect of nitrogen atomic percentage on N+-bombarded MWCNTs in cytocompatibility and hemocompatibility. *Nanoscale Res. Lett.* **2014,** *9* (1), 142.

239. Zhao, M.; Li, D.; Yuan, L.; Yue, Y.; Liu, H.; Sun, X., Differences in cytocompatibility and hemocompatibility between carbon nanotubes and nitrogen-doped carbon nanotubes. *Carbon* **2011,** *49* (9), 3125-3133.

240. Elías, A. L.; Carrero‐Sánchez, J. C.; Terrones, H.; Endo, M.; Laclette, J. P.; Terrones, M., Viability studies of pure carbon‐ and nitrogen‐doped nanotubes with entamoeba histolytica: from amoebicidal to biocompatible structures. *Small* **2007,** *3* (10), 1723-1729.

241. Okada, T.; Inoue, K. Y.; Kalita, G.; Tanemura, M.; Matsue, T.; Meyyappan, M.; Samukawa, S., Bonding state and defects of nitrogen-doped graphene in oxygen reduction reaction. *Chem. Phys. Lett.* **2016,** *665*, 117-120.

242. Sheng, Z.-H.; Shao, L.; Chen, J.-J.; Bao, W.-J.; Wang, F.-B.; Xia, X.-H., Catalyst-free synthesis of nitrogen-doped graphene via thermal annealing graphite oxide with melamine and its excellent electrocatalysis. *ACS Nano* **2011,** *5* (6), 4350-4358.

243. Wei, D.; Liu, Y.; Wang, Y.; Zhang, H.; Huang, L.; Yu, G., Synthesis of N-doped graphene by chemical vapor deposition and its electrical properties. *Nano Lett.* **2009,** *9* (5), 1752-1758.

244. McAllister, M. J.; Li, J.-L.; Adamson, D. H.; Schniepp, H. C.; Abdala, A. A.; Liu, J.; Herrera-Alonso, M.; Milius, D. L.; Car, R.; Prud'homme, R. K., Single sheet functionalized graphene by oxidation and thermal expansion of graphite. *Chem. Mater.* **2007,** *19* (18), 4396-4404.

245. Guo, H.-L.; Su, P.; Kang, X.; Ning, S.-K., Synthesis and characterization of nitrogen-doped graphene hydrogels by hydrothermal route with urea as reducing-doping agents. *J. Mater. Chem. A* **2013,** *1* (6), 2248-2255.

246. Faria, A. F.; Perreault, F.; Elimelech, M., Elucidating the role of oxidative debris in the antimicrobial properties of graphene oxide. *ACS Appl. Nano Mater.* **2018,** *1* (3), 1164-1174.

247. Sun, L.; Wang, L.; Tian, C.; Tan, T.; Xie, Y.; Shi, K.; Li, M.; Fu, H., Nitrogen-doped graphene with high nitrogen level via a one-step hydrothermal reaction of graphene oxide with urea for superior capacitive energy storage. *RSC Adv.* **2012,** *2* (10), 4498-4506.

248. Kundu, S.; Nagaiah, T. C.; Xia, W.; Wang, Y.; Dommele, S. V.; Bitter, J. H.; Santa, M.; Grundmeier, G.; Bron, M.; Schuhmann, W.; Muhler, M., Electrocatalytic activity and stability of nitrogen-containing carbon nanotubes in the oxygen reduction reaction. *J. Phys. Chem. C* **2009,** *113* (32), 14302-14310.

249. Lin, Z.; Waller, G.; Liu, Y.; Liu, M.; Wong, C. P., Facile synthesis of nitrogen‐doped graphene via pyrolysis of graphene oxide and urea, and its electrocatalytic activity toward the oxygen‐reduction reaction. *Adv. Energy Mater.* **2012,** *2* (7), 884-888.

250. Ferrari, A. C.; Meyer, J. C.; Scardaci, V.; Casiraghi, C.; Lazzeri, M.; Mauri, F.; Piscanec, S.; Jiang, D.; Novoselov, K. S.; Roth, S.; Geim, A. K., Raman spectrum of graphene and graphene layers. *Phys. Rev. Lett.* **2006,** *97* (18), 187401.

251. Zafar, Z.; Ni, Z. H.; Wu, X.; Shi, Z. X.; Nan, H. Y.; Bai, J.; Sun, L. T., Evolution of Raman spectra in nitrogen doped graphene. *Carbon* **2013,** *61*, 57-62.

252. Panchakarla, L.; Subrahmanyam, K.; Saha, S.; Govindaraj, A.; Krishnamurthy, H.; Waghmare, U.; Rao, C., Synthesis, structure, and properties of boron‐and nitrogen‐doped graphene. *Adv. Mater.* **2009,** *21* (46), 4726-4730.

253. Jones, D. P., Redox potential of GSH/GSSG couple: assay and biological significance. In *Methods Enzymol.*, Elsevier: 2002; Vol. 348, pp 93-112.

254. Smirnova, G.; Muzyka, N.; Oktyabrsky, O., Transmembrane glutathione cycling in growing Escherichia coli cells. *Microbiol. Res.* **2012,** *167* (3), 166-172.

255. Owensm, R. A.; Hartman, P. E., Glutathione: a protective agent in salmonella typhimurium and Escherichia coli as measured by mutagenicity and by growth delay assays. *Environ. Mutagen.* **1986,** *8* (5), 659-673.

256. Luo, Z.; Lim, S.; Tian, Z.; Shang, J.; Lai, L.; MacDonald, B.; Fu, C.; Shen, Z.; Yu, T.; Lin, J., Pyridinic N doped graphene: synthesis, electronic structure, and electrocatalytic property. *J. Mater. Chem.* **2011,** *21* (22), 8038-8044.

257. Okamoto, Y., First-principles molecular dynamics simulation of O2 reduction on nitrogen-doped carbon. *Appl. Surf. Sci.* **2009,** *256* (1), 335-341.

258. Niwa, H.; Horiba, K.; Harada, Y.; Oshima, M.; Ikeda, T.; Terakura, K.; Ozaki, J.-i.; Miyata, S., X-ray absorption analysis of nitrogen contribution to oxygen reduction reaction in carbon alloy cathode catalysts for polymer electrolyte fuel cells. *J. Power Sources* **2009,** *187* (1), 93-97.

259. Kim, H.; Lee, K.; Woo, S. I.; Jung, Y., On the mechanism of enhanced oxygen reduction reaction in nitrogen-doped graphene nanoribbons. *Physical chemistry chemical physics : PCCP* **2011,** *13* (39), 17505-17510.

260. Man, I. C.; Su, H. Y.; Calle-Vallejo, F.; Hansen, H. A.; Martínez, J. I.; Inoglu, N. G.; Kitchin, J.; Jaramillo, T. F.; Nørskov, J. K.; Rossmeisl, J., Universality in oxygen evolution electrocatalysis on oxide surfaces. *ChemCatChem* **2011,** *3* (7), 1159-1165.

261. Wang, Y.; Yasemin, B.; Zhang, T.; Lankone, R.; Wallace, A.; Fairbrother, H.; Keith, J.; Gilbertson, L., Unveiling the synergistic role of oxygen functional groups in the graphene-mediated oxidation of glutathione. *under review* **2020**.

262. Wang, Y.; Aquino de Carvalho, N.; Tan, S.; Gilbertson, L. M., Leveraging electrochemistry to uncover the role of nitrogen in the biological reactivity of nitrogen-doped graphene. *Environ. Sci.: Nano* **2019,** *6* (12), 3525-3538.

263. Green, A. A.; Hersam, M. C., Solution Phase Production of Graphene with Controlled Thickness via Density Differentiation. *Nano Lett.* **2009,** *9* (12), 4031-4036.

264. Bollella, P.; Fusco, G.; Tortolini, C.; Sanzò, G.; Favero, G.; Gorton, L.; Antiochia, R., Beyond graphene: electrochemical sensors and biosensors for biomarkers detection. *Biosens. Bioelectron.* **2017,** *89*, 152-166.

265. Taniselass, S.; Arshad, M. M.; Gopinath, S. C., Graphene-based electrochemical biosensors for monitoring noncommunicable disease biomarkers. *Biosens. Bioelectron.* **2019**.

266. Vecitis, C. D.; Schnoor, M. H.; Rahaman, M. S.; Schiffman, J. D.; Elimelech, M., Electrochemical multiwalled carbon nanotube filter for viral and bacterial removal and inactivation. *Environ. Sci. Technol.* **2011,** *45* (8), 3672-3679.

267. ElMekawy, A.; Hegab, H. M.; Losic, D.; Saint, C. P.; Pant, D., Applications of graphene in microbial fuel cells: the gap between promise and reality. *Renew. Sust. Energ. Rev.* **2017,** *72,* 1389-1403.

268. Yu, M.; Zhang, S.; Chen, Y.; Jin, H.; Zhang, Y.; Lu, L.; Shu, Z.; Hou, S.; Xie, B.; Cui, H., A green method to reduce graphene oxide with carbonyl groups residual for enhanced electrochemical performance. *Carbon* **2018,** *133,* 101-108.

269. Miklos, D. B.; Remy, C.; Jekel, M.; Linden, K. G.; Drewes, J. E.; Hübner, U., Evaluation of advanced oxidation processes for water and wastewater treatment – A critical review. *Water Research* **2018,** *139,* 118-131.

270. Doll, M.; Morgan, D. J.; Anderson, D.; Bearman, G., Touchless technologies for decontamination in the hospital: a review of hydrogen peroxide and UV devices. *Curr. Infect. Dis. Rep.* **2015,** *17* (9), 44.

271. Zhou, W.; Meng, X.; Gao, J.; Alshawabkeh, A. N., Hydrogen peroxide generation from O2 electroreduction for environmental remediation: A state-of-the-art review. *Chemosphere* **2019**.

272. Campos‐Martin, J. M.; Blanco‐Brieva, G.; Fierro, J. L., Hydrogen peroxide synthesis: an outlook beyond the anthraquinone process. *Angew. Chem., Int. Ed.* **2006,** *45* (42), 6962-6984.

273. Yang, S.; Verdaguer-Casadevall, A.; Arnarson, L.; Silvioli, L.; Čolić, V.; Frydendal, R.; Rossmeisl, J.; Chorkendorff, I.; Stephens, I. E. L., Toward the decentralized electrochemical production of H2O2: a focus on the catalysis. *ACS Catal.* **2018,** *8* (5), 4064-4081.

274. Jiang, K.; Back, S.; Akey, A. J.; Xia, C.; Hu, Y.; Liang, W.; Schaak, D.; Stavitski, E.; Nørskov, J. K.; Siahrostami, S., Highly selective oxygen reduction to hydrogen peroxide on transition metal single atom coordination. *Nat. Commun.* **2019,** *10* (1), 1-11.

275. Han, L.; Sun, Y.; Li, S.; Cheng, C.; Halbig, C. E.; Feicht, P.; Hübner, J. L.; Strasser, P.; Eigler, S., In-plane carbon lattice-defect regulating electrochemical oxygen reduction to hydrogen peroxide production over nitrogen-doped graphene. *ACS Catal.* **2019,** *9* (2), 1283-1288.

276. Chong, Y.; Ge, C.; Yang, Z.; Garate, J. A.; Gu, Z.; Weber, J. K.; Liu, J.; Zhou, R., Reduced cytotoxicity of graphene nanosheets mediated by blood-protein coating. *ACS Nano* **2015,** *9* (6), 5713-5724.

277. Dallavalle, M.; Calvaresi, M.; Bottoni, A.; Melle-Franco, M.; Zerbetto, F., Graphene can wreak havoc with cell membranes. *ACS Appl. Mater. Interfaces* **2015,** *7* (7), 4406-4414.